

Doctoral Thesis

STUDIES ON LARGE-SCALE EVOLUTION
OF MAGNETIC RECONNECTION USING
FULL PARTICLE SIMULATIONS WITH
ADAPTIVE MESH REFINEMENT
TECHNIQUE

Keizo Fujimoto

Department of Geophysics, Graduate School of
Science, Kyoto University

December 20, 2005

Abstract

Magnetic reconnection is widely believed to play an important role in magnetospheric substorms and solar flares as a fast conversion process of the magnetic energy to plasma kinetic energy. However, it has been difficult to describe its large-scale dynamics by using kinetic simulations due to limited computer resources. The main unresolved issues in the reconnection processes include the onset mechanism, the reconnection rate in the steady state, and the energy transport mechanism. The difficulty in approaching such issues lies in the fact that macro-scale structures can be strongly affected by localized micro-scale processes, in which the kinetic treatment of plasma is required.

In order to overcome this difficulty, we first develop a new 2-1/2 dimensional electromagnetic particle code that employs adaptive mesh refinement (AMR) technique and a particle splitting algorithm. The AMR technique subdivides and removes cells dynamically in accordance with a refinement criterion and enhances the spacial resolution locally. On the other hand, the particle splitting algorithm divides finite-size superparticles locating in fine cells, controlling the number of particles per cell in order to suppress numerical noise arising when the number of particles per cell gets too small. We perform some test simulations and compare three runs without the AMR, with the AMR, and with both the AMR and the particle splitting. These results indicate not only that the AMR and particle splitting algorithms are successfully applied to the conventional particle codes, but also that they are quite effective to achieve high-resolution simulations on the evolution of the current sheet associated with magnetic reconnection. Thus the new code allows us to implement a large-scale kinetic simulation of magnetic reconnection.

One of our goals by conducting large-scale simulations is to investigate a long time evolution of the diffusion region and to see what supports fast reconnection in a fully kinetic system. Our results show that fast reconnection is quickly achieved through the Hall effects but the system does not reach steady state and the reconnection rate decreases significantly. The key process responsible for slowing the reconnection processes is the extension of the electron diffusion region in association with the enhancement of the polarization electric field directing toward the neutral sheet in the electron inflow region. The polarization electric field is caused by the inertia difference between ions and electrons, and enhanced by the meandering motions of the background ions. The inflow electrons are forced by the polarization field to move toward the out-of-plane direction by the $\mathbf{E} \times \mathbf{B}$ drift and enhances the out-of-plane current density in the electron inflow region. Since the current density is imposed uniformly along the upstream edge of the

electron diffusion region, the magnetic field lines become mostly parallel to the x direction near the X-line. As a result, the electron meandering region so the electron diffusion region extends along the x direction. In order to confirm the role of the polarization electric field, we compare the simulation results with $m_i/m_e = 1$ and 100. It is found that (1) a steady-state reconnection is achieved in the system where the polarization electric field does not arise, (2) a large reconnection rate is obtained even in the system without the Hall effects. It is suggested that the anomalous resistivity due to the Buneman-type instability might be required to support a steady-state fast reconnection.

Another goal is to reveal energy transport processes associated with magnetic reconnection, that is, where and how plasma is accelerated and heated. In the present study, we pay attention to an electron heating mechanism in the plasma sheet-lobe boundary region, where the truncated (i.e., flat-topped) distribution function of electrons is often observed in the Earth magnetotail during magnetic reconnection. It is found that the electron two-stream instability between the background cold electrons and the strong beam electrons with high perpendicular temperature should be responsible for the formation of the flat-topped electrons. Electrons are trapped by the electrostatic potential wells resulting from the electron two-stream instability and scattered along the ambient magnetic field, so that the truncated distribution function is formed in the parallel direction. We show that the electron heating through this process occurs in the extensive region of the boundary region and the heating level is consistent with satellite observations. The strong beam electrons consist of two components originating from distinct regions. Some electrons come from the opposite boundary region of the plasma sheet along the magnetic field line, forming the cold component of the electron beam. The others are originating from the lobe region, passing through the electron diffusion region. Furthermore, we demonstrate that the Electrostatic Solitary Waves (ESW) can be evolved from the electron two-stream instability in association with magnetic reconnection. Such waves should be observed in the boundary region during reconnection.

Contents

1	General Introduction	1
1.1	Role of Magnetic Reconnection in Solar System	1
1.2	Fluid Models Explaining Fast Reconnection	6
1.3	Kinetic Aspects Beyond the MHD Framework	9
1.4	Objective of the Thesis	12
2	Electromagnetic Full Particle Code With Adaptive Mesh Refinement Technique	14
2.1	Introduction	14
2.2	Description of the Code	17
2.2.1	Data Structure and Cell Generator	17
2.2.2	Particle Splitting and Coalescence	19
2.2.3	Particle and Force Weighting within the Hierarchical Cell	21
2.2.4	Integration of the Field Equations	22
2.2.5	Integration of the Equations of Motion	26
2.3	Test Simulations	26
2.3.1	Landau Damping of the Langmuir Waves	26
2.3.2	Wave Reflections at the Boundaries of the Refined Regions	28
2.3.3	Nonlinear Evolution of the Plasma Sheet	30
2.4	Summary and Discussion	38
3	Time Evolutions of the Electron Diffusion Region and the Reconnection Rate in Large and Fully Kinetic System	40
3.1	Introduction	40
3.2	Simulation Model	42
3.3	Results	44
3.3.1	Time Evolution of the Reconnection Rate	44
3.3.2	Structure Change Around the Electron Diffusion Region	46
3.3.3	Impact on the Reconnection Rate	51

3.3.4	Comparison With the Case of $m_i/m_e = 1$	56
3.4	Summary and Discussion	58
4	A Generation Mechanism of Electrostatic Waves and Subsequent Electron Heating in the Plasma Sheet-Lobe Boundary Region During Magnetic Reconnection	62
4.1	Introduction	62
4.2	Simulation Model	64
4.3	Results	66
4.3.1	Parallel Electron Heating in the Plasma Sheet-Lobe Boundary Region	66
4.3.2	Instability Responsible for the Electron Heating	71
4.3.3	Origin of the Electron Beam	74
4.3.4	Electrostatic Solitary Waves Evolved from the Beam Instability	76
4.4	Summary and Discussion	79
5	Conclusions and Further Studies	82

CHAPTER 1

General Introduction

Magnetic reconnection is known as a fast conversion process of magnetic energy into plasma kinetic energy and believed to be a phenomenon of considerable importance in space physics and astrophysics. In this part, we briefly review theoretical and observational studies devoted toward understanding the physical mechanism of magnetic reconnection. In section 1.1, we describe why it is considered to be so important in the solar system, especially in the Earth magnetosphere, followed by discussions on magnetic reconnection proper. In sections 1.2 and 1.3, some important models explaining fast energy release due to magnetic reconnection are described. We then summarize the main problems that remain and motivate this study.

1.1 Role of Magnetic Reconnection in Solar System

We first introduce the principal physics of magnetic reconnection and explain why it is such an important process in the solar system, where the particles are highly ionized and form a plasma state.

We consider a plasma obeying a simple Ohm's law of the form

$$\mathbf{E} + \mathbf{V} \times \mathbf{B} = \eta^{eff} \mathbf{J}. \quad (1.1)$$

The left-hand side of (1.1) represents the electric field in the rest frame of the plasma flowing with velocity \mathbf{V} in the magnetic field \mathbf{B} , while the right-hand side is an Ohmic current term proportional to effective scalar resistivity η^{eff} . The parameter η^{eff} is expressed by using either inter-particle or wave-particle collision frequencies as

$$\eta^{eff} = \frac{m\nu^{eff}}{ne^2}, \quad (1.2)$$

where m and n are the mass and the number density of the plasma, and ν^{eff} is the effective collision frequency. Solving (1.1) with respect to \mathbf{E} and substituting it into

Faraday's law, and then using Ampère's law neglecting the displacement current, one can derive the induction equation which determines how \mathbf{B} develops in time

$$\frac{\partial \mathbf{B}}{\partial t} = \nabla \times (\mathbf{V} \times \mathbf{B}) + \frac{\eta^{eff}}{\mu_0} \nabla^2 \mathbf{B}. \quad (1.3)$$

The first term describes convection of the magnetic field lines with the plasma flow, while the second term represents diffusion of the magnetic field through the plasma such as to reduce the gradients. If the first term dominates so that the second term is negligible, the plasma is “frozen-in” to the magnetic field such that a fluid element which is initially located on a field line remain on the same field line forever. On the other hand, if the second term dominates the first term, the equation (1.3) becomes a diffusion equation and there is no coupling between the magnetic field and the plasma flow.

The relative importance of the two terms on the right-hand side of (1.3) is conveniently compared with the magnetic Reynolds number

$$R_m = \frac{\mu_0 U L}{\eta^{eff}} \approx \frac{|\nabla \times (\mathbf{V} \times \mathbf{B})|}{|\eta^{eff} / \mu_0 \nabla^2 \mathbf{B}|}, \quad (1.4)$$

where U is a characteristic flow speed and L is a characteristic length of the system. If R_m is large, convection dominates and frozen-in flow prevails, while if R_m is small, diffusion dominates and the coupling to the plasma flow is weak. If we consider a global structure of the Earth magnetosphere, L is the order of a few Earth radii (Re) (the scale size of the magnetospheric cavity) and U is estimated as 100 km/s (a typical magnetospheric flow speed), which leads to $R_m \gtrsim 10^{11}$. In the solar flares, on the other hand, $L \sim 10^4$ km (the size of a flare system) and $U \sim 10^2$ m/s (a typical outflow speed) result in $R_m \sim 10^8$. In both cases, the values of R_m are so large that on these scale sizes the field convection is overwhelmingly dominant and that the effect of magnetic diffusion is entirely negligible. Thus it seems that the diffusive process in the magnetosphere and the solar flares is negligible in considering their global structures.

In such a limit neglecting the diffusion term in (1.3), the behavior of plasma is strongly constrained in such a way that the particles always remain tied to the same magnetic field line as it convects with the plasma flow, and cross-field mixing of plasma elements is suppressed. Therefore when two initially separate plasma regimes come into contact with each other, one can expect that these two plasmas do not mix, instead a thin boundary layer should be formed between them separating two plasma populations and magnetic fields. Generally the boundary layer constitute a current sheet, since the fields on either side of the boundary will have different strengths and orientations tangential to the boundary. Actually, a plasma flow that is frozen-in to the magnetic field is generated on the solar surface and prevails in the solar system. The existence of so-called solar

wind, which carries magnetized plasma, was speculated by Alfvén (1957) and predicted theoretically by Parker (1958). Since the Earth magnetic field contacts with the solar wind, there indeed exists a boundary layer between them called magnetopause and it forms a current sheet (Chapman and Ferraro, 1931). Also in the Earth magnetotail and the solar flares, current sheets are formed between the anti-parallel magnetic fields and divide the two regions. Thus the perfect conductive approximation of plasma flows in the magnetic field results in thin current sheets separating distinct plasma regimes. The important is that it is not guaranteed that the effect of diffusion can be neglected in discussing the physics of these boundaries, even though it may be negligible in describing the large-scale behavior within each plasma regime. Therefore we next consider the effects of diffusion in these boundary layers.

For simplicity, we assume a boundary on which equal and opposite fields of strength B_0 contact with each other separated by a magnetic neutral sheet. The magnetic field lines in either side are along x axis so that $B_x = \pm B_0$ for $z \gtrless 0$. Then a current flowing along y axis is generated. Plasmas in either side of the boundary layer flow toward the neutral sheet with speed V , but the flow is negligible in the boundary layer such that (1.3) reduces to a diffusion equation. Now we set the half width of the equilibrium current sheet as λ . The plasma inflows are generated by the $\mathbf{E} \times \mathbf{B}$ drifts of the particles so that $V \simeq E_y/B_0$. For steady state system, Faraday's law ($\nabla \times \mathbf{E} = 0$) requires that the electric field E_y should be spatially uniform. Thus the electric field imposed outside the current sheet

$$E_y \simeq V B_0$$

can be equated by that in the current sheet where magnetic diffusion is dominant (i.e., the diffusion region)

$$E_y \simeq \eta^{eff} J_y. \quad (1.5)$$

Using Ampère's law ($J_y \simeq B_0/\mu_0\lambda$), we obtain

$$R_m = \frac{\mu_0 V \lambda}{\eta^{eff}} \simeq 1, \quad (1.6)$$

so that the width of the current sheet is sufficiently small and the diffusion becomes important.

In a practical sense, the effective topology of the magnetic field lines is described in Figure 1.1 during a steady magnetic reconnection. The magnetic field lines in either side of the boundary layer convect toward the boundary with the plasma flows, then they are reconnected to a field line convecting from the opposite side of the boundary

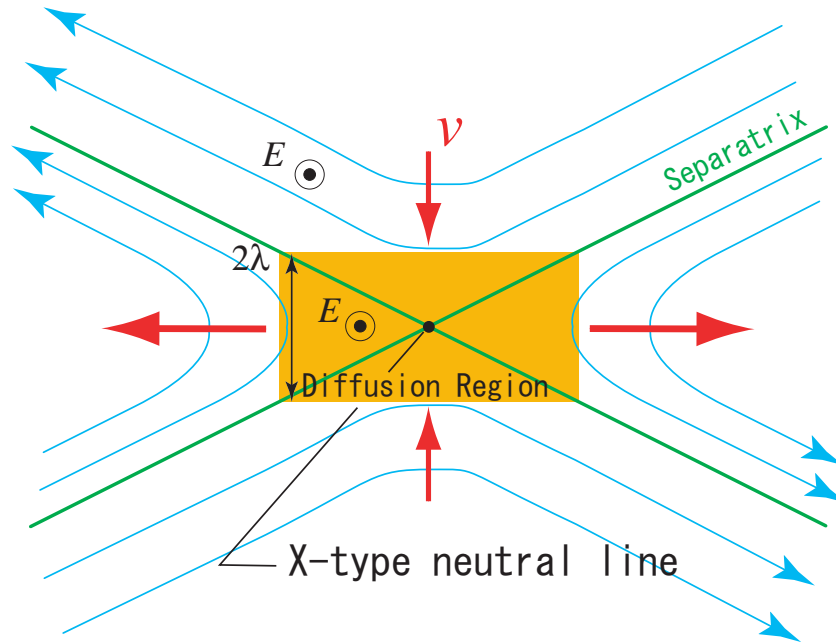


Figure 1.1: Magnetic field lines (light blue lines) and flow vectors (red arrows) around the neutral line during a steady-state magnetic reconnection. Hatched area represents the diffusion region where magnetic diffusion dominates the effect of plasma convection.

in the diffusion region. The reconnected field line is severely bent, so that the magnetic tension accelerates the inflowing plasmas away from the neutral line along the boundary layer. Thus the magnetic energy is converted to the plasma kinetic energy in the form of accelerated and heated plasma jets flowing away from the neutral line. This description of the field and plasma behavior was first suggested by Dungey (1953).

Next, let's consider the interaction between the solar wind and the Earth magnetosphere, in which we concluded in the above discussion that the perfect conductivity approximation was quite valid. If the magnetic field in the solar wind has a southward component, it is likely that the northward magnetic field originated from the magnetosphere reconnects with the solar wind magnetic field in the dayside magnetopause. In Figure 1.2, a convection model of the magnetosphere is shown in association with the dayside reconnection after Dungey (1961). Magnetic reconnection in the dayside magnetopause gives rise to open field lines connecting from the polar regions to the solar wind, allowing the solar wind plasma to enter the magnetosphere. The solar wind flow carries these field lines from the dayside to the night side of the magnetosphere and stretches them out into the magnetotail lobe. The oppositely-directing magnetic fields in the northern and southern tail lobes form a current sheet between them. Subsequently magnetic reconnection occurs in the current sheet and reconnects the open

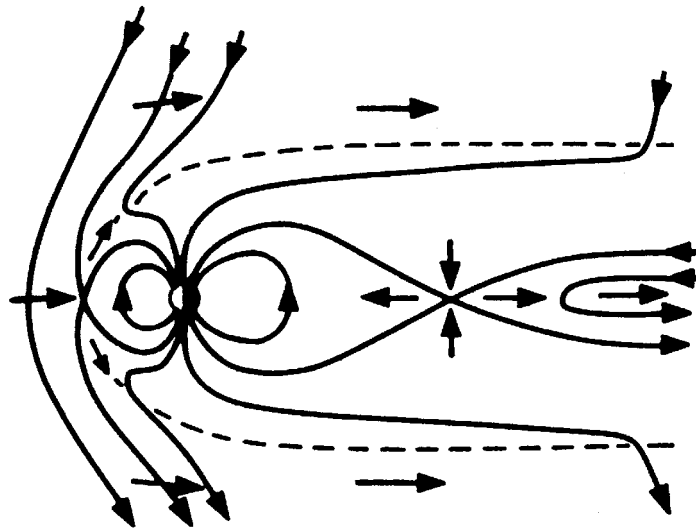


Figure 1.2: Magnetospheric model of the Earth. Magnetic reconnection occurs at the dayside magnetopause and the magnetotail current sheet, which facilitates the entry of the solar wind momentum into the magnetosphere driving a large-scale internal convection. (Adopted from Cowley (1985))

field lines of the lobes, generating closed field lines in the earthward side. These closed field lines are returned back to the near Earth magnetosphere with the plasma flow. If the dayside reconnection does not occur, the magnetospheric field is confined to a cavity surrounding the Earth as described by Chapman and Ferraro (1931). In such a case, the magnetospheric and solar wind plasmas are separated by the magnetopause, and plasma mass and momentum transfer across the boundary is weak. Thus magnetic reconnection in the Earth magnetosphere allows efficient entry of solar wind momentum into the magnetosphere, driving a large-scale internal convection.

The importance of magnetic reconnection lies in the fact that a localized breakdown of the perfect conductivity can lead to global structure changes via magnetic reconnection, even though in the global scale itself the perfect conductivity approximation is quite valid. Magnetic reconnection not only allows reconfigurations of the magnetic field to take place toward states of lower energy, but also facilitates exchanges of plasma mass, momentum, and energy between plasmas originating from different regimes.

The magnetospheric convection model driven by the dayside reconnection has been established to explain large energy releases in association with magnetic substorms (e.g., Dungey, 1961; Axford et al., 1965; Petschek, 1966). This model has been supported by extensive number of satellite observations and correlated ground observations (e.g., McPherron, 1970; Rostoker, 1972; Hones, 1973; Coroniti et al., 1980), in which the im-

portance of the dayside and nightside reconnections for substorm dynamics was demonstrated. Furthermore, subsequent satellite observations by Geotail spacecraft revealed that magnetic reconnection in the near-Earth magnetotail occurred at $X = -20$ to -30 Re in the GSM coordinate (Nagai et al., 1998), preceding a few minutes to the substorm onsets identified by the ground observations (Miyashita et al., 1999). Therefore it is overwhelming today that magnetic reconnection in the dayside and nightside of the Earth magnetosphere should play an important role in substorm dynamics (Baker et al., 1999).

Magnetic reconnection is also believed to be of importance in the solar flares as a process for effective energy releases of the accumulated magnetic energy into the plasma kinetic energy (e.g., Giovanelli, 1947; Sweet, 1958; Parker, 1963). The evidence of magnetic reconnection in the solar flares has been demonstrated through many X-ray observations (e.g., Gold, 1961; Sweet, 1969) and emphasized its responsibility for plasma energization (Lin and Hudson, 1976).

1.2 Fluid Models Explaining Fast Reconnection

In this and next sections, we discuss detailed processes of magnetic reconnection and show some important models describing the steady-state conversion processes of magnetic energy to plasma kinetic energy. The key point in the following models is how fast energy conversion as observed in the magnetospheric substorms and the solar flares can be achieved. In this section, we introduce the well established Sweet-Parker model (Sweet, 1958; Parker, 1963) and the Petschek model (Petschek, 1964), which were constructed in the framework of the magnetohydrodynamics (MHD). We will discuss more recent models beyond the MHD treatment of plasma in the subsequent section.

We start with the Sweet-Parker model shown in Figure 1.3. This model employs two-dimensional plane system and assumes that plasma acceleration occurs only in the diffusion region. Thus all the inflow plasma passes through the diffusion region and is accelerated toward the downstream region. Since the magnetic energy is converted to the plasma thermal energy due to Joule heating (via (1.5)) in the diffusion region, the plasma pressure therein must be higher than in the surrounding region. If the diffusion region has a finite length as shown in Figure 1.3 (shaded region), the pressure gradient should arise along the boundary, which accelerates the inflowing plasma toward the downstream region. Since either the flow speed in the inflow region and the magnetic field strength in the outflow region are expected to be very small, Bernoulli's law along a stream line

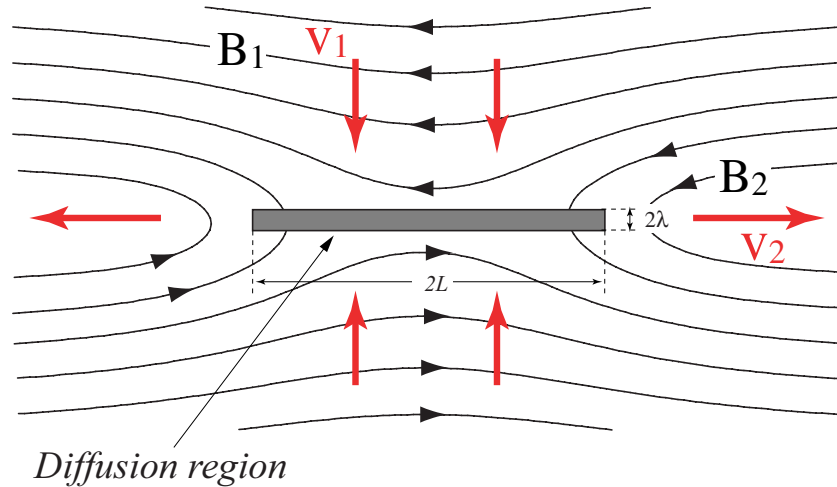


Figure 1.3: Sketch of a reconnection geometry in the Sweet-Parker model.

passing through the diffusion region gives

$$P_0 + \frac{B_1^2}{2\mu_0} \simeq P \simeq P_0 + \frac{1}{2}mnV_2^2, \quad (1.7)$$

where P_0 is the plasma pressure in the region far from the diffusion region, P the plasma pressure in the diffusion region, B_1 the magnetic field strength in the inflow region, V_2 the flow speed in the outflow region, and m and n the mass and number density of plasma, respectively. Note that we assume the plasma density is spacially uniform. Since we consider the steady-state reconnection, Faraday's law ($\nabla \times \mathbf{E} = 0$) requires that the out-of-plane electric field E_0 should be spacially uniform, so that

$$E_0 = V_1B_1 = V_2B_2, \quad (1.8)$$

where V_1 is the inflow speed, and B_2 is the magnetic field strength in the outflow region. We further assume that the plasma is incompressible, then the conservation of mass gives

$$V_1L = V_2\lambda. \quad (1.9)$$

We can obtain the outflow velocity V_2 from (1.7) as

$$V_2 \simeq \frac{B_1}{\sqrt{\mu_0nm}} \equiv V_A, \quad (1.10)$$

which indicates that the plasma is accelerated up to the order of the Alfvén velocity defined in the inflow region. We consider the reconnection rate, which means the magnetic flux reconnected per unit time and unit length along the X-line. From Faraday's law ($\partial\mathbf{B}/\partial t = \nabla \times \mathbf{E}$), it is found that the reconnection rate is simply estimated by the

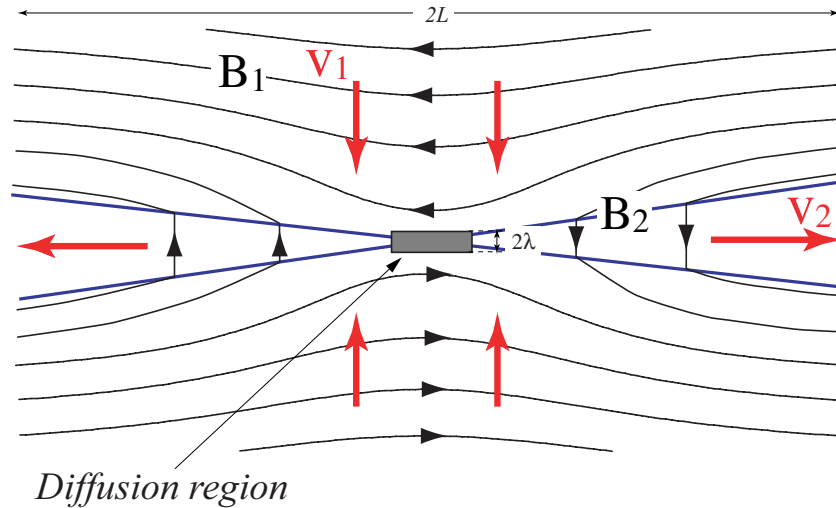


Figure 1.4: Sketch of a reconnection geometry in the Petschek model. The diffusion region has been shrunk to a center of the diagram, instead the plasma is accelerated in the slow-mode shocks (blue lines) extended from the X-line.

electric field imposed along the X-line (Dungey, 1978). Using equations (1.8), (1.9), and (1.10), one can obtain

$$E^* \simeq \frac{\lambda}{L} \simeq R_m^{-1/2}, \quad (1.11)$$

where $E^* = E_0/V_A B_1$ is the normalized electric field, and $R_m = \mu_0 v_1 L/\eta$ is the magnetic Reynolds number. We used (1.6) for the second transform. Note that the Sweet-Parker model assumes the classical resistivity η arising from the Coulomb collisions (Spitzer, 1962).

The Sweet-Parker model realizes a fast plasma outflow. However, the reconnection rate is inversely proportional to the square root of R_m defined by the system size L . Such a Reynolds number is so large in the Earth magnetosphere and the solar coronas, as we discussed before, that the reconnection rate becomes very small and insufficient to explain fast energy releases associated with the magnetospheric substorms and the solar flares.

In order to solve this problem, Petschek (1964) introduced the field configuration shown in Figure 1.4. In the Petschek model, the diffusion region is shrunk to a center of the reconnection region and most of the inflowing plasma does not pass through the diffusion region in order to be accelerated. Instead, the plasma can be accelerated in the slow-mode shocks (blue lines) extended from the X-line. The acceleration occurs due to the $\mathbf{J} \times \mathbf{B}$ force, different from the plasma pressure gradient in the Sweet-Parker model. An approximate balance of the magnetic shear stress at the separatrices and the

momentum change yields

$$mnV_1V_2 \simeq \frac{B_1B_2}{\mu_0}. \quad (1.12)$$

Combination of (1.8) and (3.5) gives (1.10) again. However, since the Petschek model does not depend on the size of the diffusion region in terms of plasma acceleration, the horizontal scale of the diffusion region can be small. This is a key to allow fast reconnection. According to Petschek (1964), the upper limit of the reconnection rate is

$$E_{max}^* \simeq \frac{\pi}{8} [\ln(M_A^2 R_m)]^{-1}, \quad (1.13)$$

where $M_A = V_1/V_A$ is the Alfvén Mach number of the inflowing plasma. The reconnection rate in this case is inversely proportional to the logarithm of R_m rather than to its square root in the Sweet-Parker system, so it can be drastically increased. For typical R_m values, E_{max}^* lies in the range 0.01 to 0.1, compared with 10^{-5} to 10^{-4} for the Sweet-Parker model. Note that the diffusion region in the Petschek model is still significant since the actual process of reconnecting the magnetic field occurs there.

Though the Petschek model achieves much faster reconnection than the Sweet-Parker model, it is still difficult to produce sufficiently high resistivity for realizing large reconnection rate in the collisionless plasma. For example, if the size of the diffusion region is assumed to be the order of the ion inertial length, $10^6 \sim 10^7$ times larger resistivity than the conventional Coulomb resistivity is required in order to achieve $E^* \simeq 0.1$, which is the case in the magnetospheric substorms. Nevertheless the Petschek model is well consistent with numerical simulations and satellite observations. For example, the slow-mode shocks are obtained in the MHD simulations (Sato, 1979; Scholer and Roth, 1987; Ugai, 1993) and detected by the Geotail observations (Saito et al., 1995). The fact that the outflow velocity from the diffusion region reaches the Alfvén velocity is also confirmed by kinetic simulations (e.g., Shay et al., 1998; Hesse et al., 1999) and the Geotail observations (Nagai et al., 1998). Thus the remaining question is what is the generation mechanism of such high resistivity, much higher than the classical resistivity due to Coulomb collisions. In the next section, we discuss more recent model to produce such high ‘effective’ resistivity beyond the MHD framework.

1.3 Kinetic Aspects Beyond the MHD Framework

As discussed in the previous sections, the ideal MHD condition breaks down in the vicinity of the X-line and the magnetic diffusion becomes dominant, forming the diffusion region. In the MHD framework, the magnetic diffusion has attributed to the resistivity

generated by the classical Coulomb collisions (Spitzer, 1962) and it was found that the values were too small to drive fast reconnection in the collisionless plasma. Our next step is to consider more general features of plasma beyond the MHD framework. In this section we start with the generalized Ohm's law in a steady state, which describes a two-fluid plasma,

$$\mathbf{E} + \mathbf{V} \times \mathbf{B} = -\frac{m_e}{e}(\mathbf{V}_e \cdot \nabla)\mathbf{V}_e - \frac{1}{ne}\nabla \cdot \mathbf{P}_e + \frac{1}{ne}\mathbf{J} \times \mathbf{B}, \quad (1.14)$$

where m_e is the electron mass, \mathbf{V}_e the electron flow velocity, and \mathbf{P}_e the electron pressure tensor. We assume that the classical resistivity term ($\eta\mathbf{J}$) is negligible. If any term in the right-hand side of (1.14) is negligibly small compared with the convection term in the left-hand side, the ideal MHD condition holds. Thus, in order to determine when the frozen-in condition can break down, it is necessary to estimate the order of magnitude of each term in the right-hand side.

The first term expresses electron inertial effects and the scale size is the order of the electron inertial length λ_e . The scale length of the second term (pressure gradient) is the order of the electron gyroradius λ_{ge} . The last term represents the decoupling between ions and electrons, so-called Hall effects, and has a scale size of the ion inertial length λ_i . When the scale length of gradient is much larger than any of these characteristic lengths, the frozen-in condition holds.

In two-fluid system consisting of ions and electrons, the inflow ions can be decoupled from the ambient magnetic field when they approach the neutral sheet as close as λ_i . Thus the region within λ_i is the diffusion region. Electrons, however, still remain magnetized at this distance, since their inertia is much smaller than those of ions. Instead, their frozen-in constraint can break down at the distance comparable with the local gyroradius λ_{ge} , within which electrons are expected to perform the meandering motions (e.g., Pei et al., 2001). This non-magnetized region for electrons is called the electron diffusion region. Therefore the diffusion region in the two-fluid system develops two-scale structure as shown in Figure 1.5, different from the MHD system (see Figure 1.1). The electron diffusion region with the scale size of λ_e is found to be embedded within the ion-scale diffusion region. Thus inside the diffusion region but outside the electron diffusion region, ions are decoupled from the ambient magnetic field but electrons are still frozen-in to the field and continue to move with the $\mathbf{E} \times \mathbf{B}$ drift motion toward the current sheet. This relative motion between ions and electrons produces currents in the vicinity of the X-line, forming the Hall current system (Sonnerup, 1979; Terasawa, 1983). Sonnerup (1979) first predicted the presence of the Hall current system theoretically in which the four current loops resulted in a quadrupole structure in the

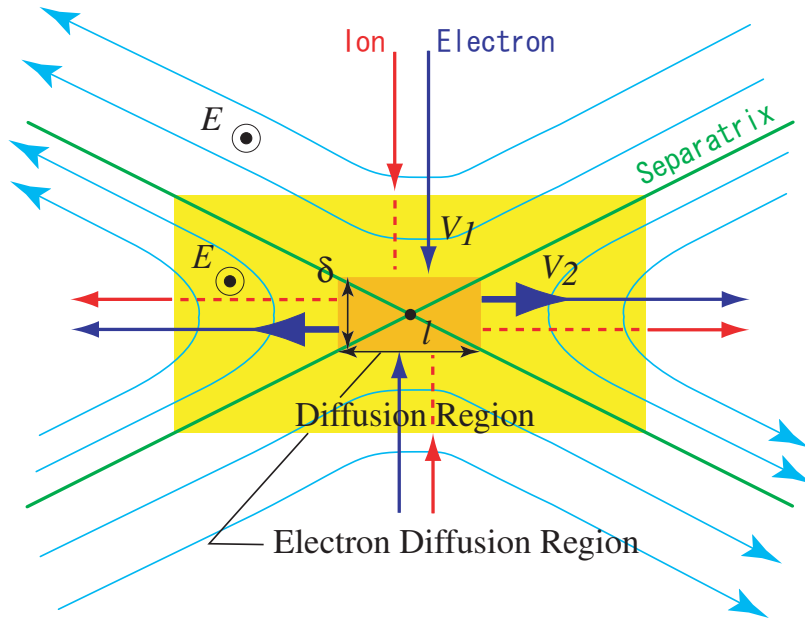


Figure 1.5: Two-fluid picture around the X-line. The diffusion region develops two-scale structure associated with the ion and electron scales, forming the electron diffusion region in side the ion-scale diffusion region. Red arrows represent the ion flow vector, while blue arrows the electron flow vector.

out-of-plane (dawn-dusk) magnetic field variations. In the past decade, not a few studies with hybrid simulations (e.g., Mandt et al., 1994; Hesse and Winske, 1994, 1998; Lin and Swift, 1996; Nakabayashi and Machida, 1997; Nakamura et al., 1998; Shay et al., 1998, 2001) and full particle simulations (e.g., Tanaka, 1995; Hoshino et al., 1998, 2001a,b; Hesse et al., 1999) have confirmed the presence of the Hall current system and the associated quadrupole magnetic field structure in the reconnection process. In these studies electrons have been ascertained to play as carriers of the Hall currents. Furthermore, Nagai et al. (2001) recently found the Hall current system (the accelerated electrons) and its effect on the magnetic field in the Earth magnetotail, using magnetic field and plasma measurements onboard the Geotail spacecraft.

In the electron diffusion region, on the other hand, the kinetic behavior of electrons becomes important. The reconnection process of the magnetic field actually proceeds in this region. It has been revealed by using two-dimensional kinetic simulations that the dissipation process in the electron diffusion region is supported by the electron inertia and the gradient of the electron pressure tensor in the generalized Ohm's law (1.14) (Hesse and Winske, 1998; Kuznetsova et al., 1998; Hesse et al., 1999). This indicates that the collision effect in a classical sense is replaced by electron inertial effects in the

collisionless reconnection. If their model is really appropriate as the dissipation model, three-dimensional features such as the anomalous resistivity arising from interactions between waves propagating along the current sheet and plasma particles would be negligible, and the reconnection process might be basically two-dimensional.

Though the dissipation process of magnetic field is supported by the electron dynamics, it has little or no effect on the reconnection rate (Biskamp et al., 1997; Shay and Drake, 1998; Birn et al., 2001). Instead ion dynamics can control the reconnection process so the electron-scale structure, in which the actual reconnection of the magnetic field takes place. They suggest that the high reconnection rate is produced by the Hall term in the generalized Ohm's law (1.14), so that the inclusion of the Hall effects should be a sufficient condition to achieve fast reconnection. Though recent simulation studies comparing MHD, Hall MHD, hybrid, and full particle simulations confirmed the importance of the Hall effect for fast reconnection, the system did not reach steady state and the reconnection rate decreased after it reached a peak value (Shay et al., 2001; Hesse et al., 2001; Pritchett, 2001; Kuznetsova et al., 2001). They attributed the reason to the periodic system in the direction of the initial magnetic field, in which compressional effects in the magnetic islands could affect the reconnection process. One of the solutions in order to suppress the boundary effects is to perform the above comparison in a large system so that the periodicity is negligible therein. However, such simulations with conventional full particle models are still hard to be carried out within the limitation of computer resources. Furthermore, recent hybrid simulations demonstrated that the Hall effects were not needed to achieve fast reconnection (Karimabadi et al., 2004), although their simulations did not include the electron kinetic effects. Therefore it is necessary to reconsider what is supporting fast reconnection in collisionless plasma system.

1.4 Objective of the Thesis

Main problems on the physical processes associated with magnetic reconnection are summarized in the following three points:

1. What trigger magnetic reconnection?
2. What supports fast reconnection in a steady state? Are the Hall effects sufficient for achieving large reconnection rate?
3. What is the energy transport process, that is, how and where can plasma be accelerated and heated?

Each of the above processes is expected to include strongly nonlinear coupling among electron-, ion-, and MHD-scale processes. Thus numerical simulations in self-consistent systems have been extensively examined to understand these subjects. The difficulty in considering the problems associated with magnetic reconnection lies in the locality of micro-scale processes embedded in macro-scale processes. In order to make a self-consistent description around the reconnection region, it is necessary to perform a large-scale kinetic simulation including from electron kinetic processes to MHD processes. However, it is still difficult to carry out such simulations by using conventional kinetic codes (e.g., particle-in-cell code, Vlasov code, and so on) because of the limitation of computer resources.

In this thesis, we first develop 2-1/2 dimensional full particle code (in which both ions and electrons are treated as finite-size superparticles) with adaptive mesh refinement (AMR) technique. The AMR technique subdivides and removes cells dynamically in accordance with a refinement criterion and it is quite effective to achieve high-resolution simulations of phenomena that locally include micro-scale processes. This new code allows us to perform large-scale simulations of magnetic reconnection, which gives two advantages on the modeling of magnetic reconnection. One is that it enables us to describe the long time evolution of the current sheet without caring the effects due to the periodic boundary condition, which is related to the second problem listed above. The other is that it is literally possible to pursue kinetic processes in an extensive region around the X-line, which leads to the understanding of electron heating mechanism in the plasma sheet-lobe boundary region (relating to the third problem).

In Chapter 2 we will give a detailed description of the new electromagnetic full particle code with the AMR technique and emphasize the efficiency compared with conventional particle codes. Chapter 3 is devoted to the long time evolution of the reconnection rate. We will show that the reconnection rate can drop after it reaches a peak value. The Hall effects shown in the previous section seem to be still important until the reconnection rate saturates. However, the meandering motion of the cold ions can lead to a structure change of the electron diffusion region, causing the damping of the reconnection rate. A generation mechanism of the heated electrons and the solitary waves, which have been often observed in the Earth magnetotail, is explained in Chapter 4. Finally, in Chapter 5, we summarize this study and present a vision for future studies. Especially it is emphasized that developing the three-dimensional version of our code is inevitable in order to understand the triggering mechanism of magnetic reconnection.

CHAPTER 2

Electromagnetic Full Particle Code With Adaptive Mesh Refinement Technique

2.1 Introduction

Magnetic reconnection plays an important role in a fast conversion process of the magnetic energy to plasma kinetic and thermal energy. It occurs in the accretion disks of astrophysical bodies, solar flares, and the Earth magnetosphere, so that it is a ubiquitous phenomenon in the universe.

In the Earth magnetosphere, magnetic reconnection facilitates the entry of particles and energy from the solar wind into the magnetosphere at the day-side magnetopause. It is also believed to affect the dynamics of magnetospheric substorms by changing the current sheet structure and the configuration of magnetic field lines in the Earth magnetotail. In a reconnection process, the ideal magnetohydrodynamic (MHD) condition breaks down in the diffusion region arising near the X-line, where dissipation processes of the magnetic field are dominant. In a sufficiently collisional plasma, the resistive MHD theory (e.g., Sweet, 1958; Parker, 1963; Petschek, 1964) is valid for describing the diffusion region by parameterizing collisional effects. However in a region where the classical collision rate is very small such as in the magnetosphere, the Sweet-Parker diffusion region is elongated and the reconnection rate is impractically low (Vasyliunas, 1975). Actually in such a collisionless plasma, the diffusion region develops a two-scale structure associated with the electron and ion scales, that is, the electron inertial length λ_e and the ion inertial length λ_i , respectively. Within a distance from the X-line of the order of λ_i , the ions are easily unmagnetized because they have large gyroradii compared with the scale size λ_i . We call this region the ion diffusion region. On the other hand, even closer to the X-line the electrons also decouple from the ambient magnetic field. This region,

which is called the electron diffusion region, has scale size of λ_e . Inside the electron diffusion region, where the electrons are unmagnetized and strongly accelerated away from the X-line, the nongyrotropic electron pressure can give rise to the reconnection electric field (Hesse and Winske, 1998), which implies that kinetic effects of the electrons are essential to dissipation mechanisms of the magnetic field in the electron diffusion region. Outside the electron diffusion region but inside the ion diffusion region, the ion motion decouples from that of the still frozen-in electrons. This difference in motion produces currents, so-called Hall current system, in the vicinity of the X-line (Sonnerup, 1979). It is suggested that the inclusion of the Hall term realizes much faster reconnection rate than that in the case of a resistive MHD (Birn et al., 2001, and references therein). Thus a full particle simulation, in which both electrons and ions are treated as particles, is very effective to describe the dynamics in the vicinity of the X-line.

Most full particle codes employ particle-in-cell (PIC) technique, in which the current and charge densities are accumulated on a spatial grid from the particle data and the forces on the particles are interpolated from the adjacent spatial grids. Though the full particle model using PIC technique is conceptually very simple and one does not introduce any approximation in the basic laws of mechanics and electromagnetism, the restrictions on the grid spacing are very severe and one must set it to be as small as the electron Debye length λ_{De} , which is the order of 10^3 m in the central current sheet of the magnetotail. On the other hand, magnetic reconnection changes the current sheet structure dynamically in MHD scale of the order of 10^9 m. Hence, for modelling of the magnetosphere including the nonlinear evolution of magnetic reconnection, the spatial dynamic range is required to be 10^6 . Furthermore, since the electromagnetic PIC code requires at least dozens of particles per cell to suppress a numerical noise, the number of particles for each species is over 10^{13} even in the two dimensional system. However a simulation with 10^{12} cells and 10^{13} particles in the two dimensional system is unrealistic today due to the limitation of computer resources. Usual compromise is to use low mass ratio of the ion to the electron, although too low mass ratio allows a spurious wave mode to grow (Daughton, 1999). However, even when the mass ratio is 100 instead of 1834 that is realistic, the required numbers of cells and particles are 10^{10} and 10^{11} , respectively. It is still difficult to conduct such a simulation with currently available computer resources.

In the Earth magnetotail, the number density of plasma is confirmed to be much higher in the central plasma sheet than in the lobe region according to the observations with satellites (e.g., Baumjohann et al., 1989; Baumjohann and Treumann, 1997), so that the electron Debye length is the smallest in the central plasma sheet. Therefore, the spatial resolution required for the numerical stability is much higher in the central

plasma sheet than in the lobe region. Since the diffusion region appears also in the central plasma sheet, the spatial resolution should be high there also in terms of the physical perspective. In conventional full particle simulations of magnetic reconnection (e.g., Pritchett, 1994; Tanaka, 1995; Hesse and Winske, 1998; Shay et al., 2001; ?), the spatial resolution has been uniform in the whole simulation area in accordance with that required in the central plasma sheet. Thus, in the lobe region which occupies most of the simulation area, the spatial resolution has been unnecessarily high. The adaptive mesh refinement (AMR) technique is beneficial to reducing the number of cells and saving computer resources by introducing finer cells hierarchically in only the regions, such as the central plasma sheet and the diffusion region, where higher spatial resolution is required (see § 2.2.1).

A block structured adaptive method was extensively developed by Berger and the coworkers to solve partial differential equations on a hierarchy of nested cells covering high-resolution regions (Berger and Olinger, 1984; Berger and Colella, 1989). An introduction of the AMR technique to a particle code has been examined for the application to the N-body simulations describing cosmological matter such as the formation and structure of galaxies (Villumsen, 1989; Jessop et al., 1994; Suisalu and Saar, 1995; Gelato et al., 1997; Kravtsov et al., 1997; Yahagi and Yoshii, 2001; Knebe et al., 2001; Teyssier, 2002). In the N-body codes, the mass density is assigned to the neighboring grids using the cloud-in-cell (CIC) algorithm, which is equivalent to the PIC algorithm for orthogonal coordinates (Birdsall and Langdon, 1991). In the early N-body codes with the AMR technique (Villumsen, 1989; Jessop et al., 1994; Suisalu and Saar, 1995; Gelato et al., 1997), they adopted nested cells as like as Berger and Olinger (1984) to increase force resolution, so that the refined regions were give in rectangular shape. Though the rectangular refinements facilitate the data structure, they are not suitable for models including the complicated structures that are difficult to cover efficiently with rectangular regions. On the other hand, a tree structured cells have been also used in order to increase the spatial resolution locally and achieve a high dynamical range simulation (Barnes and Hut, 1986; Griebel and Zumbusch, 1999; Dreher and Grauer, 2005). Kravtsov et al. (1997) developed the adaptive refinement tree (ART) code, in which the tree structured cells are connected with each other on all hierarchical levels. The ART code subdivides all cells that satisfy a refinement criterion regardless of the shape of the refined regions, so that it enables us to achieve an efficient refinement to cover a complicate structure. Although their code is adaptive only in space, recently developed codes (Yahagi and Yoshii, 2001; Knebe et al., 2001; Teyssier, 2002) are adaptive not only in space but also in time. Plasma simulations using an electrostatic PIC code with

the AMR have been recently examined in order to describe the ion beam transport in a heavy ion fusion (Vay et al., 2004).

In this paper we present a newly developed two and a half dimensional electromagnetic full particle code with the AMR technique. In this code we deal with two species of charged particles, that is, ions (protons) and electrons. The current and charge densities are assigned onto the hierarchical cell corners using the PIC algorithm, which process is similar to the mass density assignment by the CIC algorithm used in the N-body codes. The electromagnetic field is calculated via Maxwell's equations, unlike the Poisson equation used to derive the gravitational field in the N-body codes. The particles (superparticles) are also subdivided in the refined regions in order to suppress the numerical noise that arises due to the decrease in the number of the particles per cell. In the following sections we describe the details of our code (§ 2.2), and discuss the results of test simulations and application to the current sheet evolution (§ 2.3). Finally we summarize and conclude this work in § 2.4.

2.2 Description of the Code

2.2.1 Data Structure and Cell Generator

In order to increase a spatial resolution efficiently, the AMR technique subdivides only cells that satisfy a refinement criterion and add data sets for finer cells hierarchically onto the uniform base cells that cover the entire simulation area. If a base cell is refined, it has four child cells that have half the size of the base cell. These child cells can be also refined in turn and finer cells are generated, and so on. In our code, a refinement level L in the hierarchy is defined by using the cell size of the level (Δ_L) as $L \equiv \log_2(l_y/\Delta_L)$, where l_y is the vertical size of the two-dimensional simulation area. We use only cells with integer level.

The data structure in our approach is completely different from that used in the conventional electromagnetic particle codes. Cells are treated as independent units organized in refinement trees rather than elements of arrays, so that one can build a very flexible cell hierarchy that can be easily modified. The hierarchical cell structure in our code is basically the same as the fully threaded tree structure developed by Khokhlov (1998), and supported by a set of pointers as shown in Figure 2.1. Each cell is needed to have information of the parent, child, and neighboring cells. Since a cell has four child cells, if any, we group these four cells together in order to save memory for pointers and facilitate parallel computing. We call this group an oct (after an octet in the case of a cubic cell). Each cell has a pointer to the child oct (*OctCh*). Each oct has pointers to

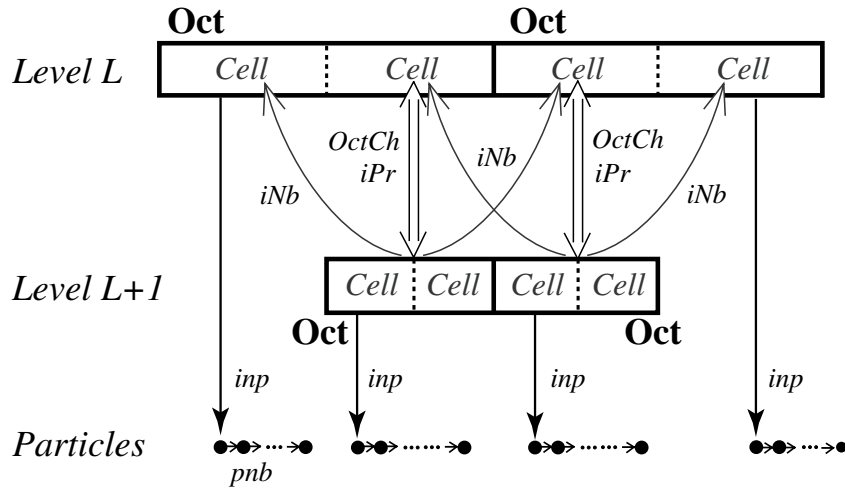


Figure 2.1: Hierarchical data structure in our code. One dimensional structure is shown for simplicity. The pointers that each cell or oct has are basically the same as those in the tree structure developed by Khokhlov (1998), but we additionally give two pointers, inp directed to a representative superparticle from each oct, and pnb directed from each particle to the neighboring particle in the same oct.

the parent cell (iPr), the parent cells of the neighboring octs (iNb), and a representative particle belonging to the oct (inp). Note that each particle belongs to the finest oct in which the particle is located. Each particle has a pointer to the neighboring particle in the same oct (pnb), which leads to a beaded structure of particles as described in Figure 2.1 (Teyssier, 2002). In addition to these pointers, each oct has information of the level of cells included therein, the integral position at a corner of the oct, and the number of particles in the oct. The level of a cell is very useful information to efficiently sweep through a level. The position of a oct and the number of particles included in the oct are helpful to construct the beaded structure of particles. Each cell also has physical data at a corner of the cell; charge density, current density, and electromagnetic fields.

A refinement process subdivides a cell that satisfies a refinement criterion and generates four child cells. In electromagnetic particle codes, one of the refinement criteria should be defined by the local electron Debye length in terms of the numerical stability. However, additional criteria can be introduced in accordance with physics that is incorporated in the code. An example in the case of nonlinear evolution of the plasma sheet is shown in § 2.3.3. When the parent cell is refined, we check if there exist the surrounding eight cells having the same level as the parent cell. Even if one of eight cells are absent, no splitting is implemented and no child cells are created. Thus, in our tree structure, no neighboring cells have level difference greater than one, which assures that there are

no sharp gradients on the boundaries of the refined regions.

The refinement procedure is similar to that in Kravtsov et al. (1997). The process is started from the base level cells and recursively proceeds to reach the dynamic range level cells at each time step. First, we put flags to cells that satisfy refinement criteria. At this point, no cells are subdivided. In order to smooth the marked region, we next put flags to the eight cells surrounding each cell flagged firstly. Furthermore, we construct buffer region surrounding the refined region by giving other flags to cells that surround the originally flagged cells but have no flags for the refinement. The buffer regions are used to set boundary conditions for calculating the electromagnetic fields in the refined region as mentioned in § 2.2.4. After that, we search again the whole cells with the target level. If a cell has a flag but has no child cells, the cell is subdivided and half-sized refined or buffer cells are generated. If a cell has no flag but has child cells, the child cells are removed from the hierarchical structure. If a cell has both a flag and child cells, or has neither a flag nor child cells, no operation is conducted for the cell. Thus the refinement operation is performed only to the cells that have any changes in terms of the refinement criteria at each time step, so that the refinement procedure is quickly completed.

The beaded structures of particles must be rearranged in association with the refinement procedure and the movement of particles. When a new oct is created, the particles located in the parent cell are removed from the beaded structure in the parent oct and reconnected to that in the child oct. On the other hand, when an oct is removed from the tree structure, the beaded structure is reconnected to that in the parent oct. Furthermore, particles moving away across oct boundaries are removed from the beaded structure in the oct and reconnected to those in new octs in which they are located.

2.2.2 Particle Splitting and Coalescence

One of the main problems in developing the electromagnetic PIC codes using the AMR technique is decrease in the number of particles per cell in the refined regions (Fujimoto and Machida, 2005a). Especially, in the vicinity of the X-line formed in association with magnetic reconnection, spatially high-resolution simulations are required because the kinetic effects of electrons are expected to be important. However, the number density of plasma in such a region is low due to inflow of the tenuous plasma in the lobe region, so that the number of particles per cell is decreased and the numerical noise is increased.

In order to solve the problem, we subdivide particles (superparticles) residing in the subdivided cells and control the number of particles per cell. We use the particle splitting-

coalescence algorithm developed by Lapenta (2002). The processes should conserve the following quantities,

1. the moments on each grid, that is, the charge and current densities,
2. the total charge and mass of particles,
3. the total momentum and energy of particles,
4. the distribution function of particles.

In the splitting algorithm in the two-dimensional system, a particle with charge q_0 , mass m_0 , position \mathbf{x}_0 , and velocity \mathbf{v}_0 can be replaced by four particles. The new particles labeled by p ($p = 1, 2, 3, 4$) have charges $q_p = q_0/4$, masses $m_p = m_0/4$, and velocities $\mathbf{v}_p = \mathbf{v}_0$. The new particles are located at $x_{1,2} = x_0 \pm \Delta r$, $x_{3,4} = x_0$, $y_{1,2} = y_0$, $y_{3,4} = y_0 \pm \Delta r$ (see Figure 2.2a). Here, Δr should be chosen so as to suppress the local fluctuation of the spatial particle distribution, which can arise from the particle splitting, as much as possible. In this context, $\Delta r = \Delta_L/\sqrt{N_p}$ is considered to be a natural choice in the two-dimensional case, where N_p is the number of particles in the cell with the size Δ_L . This algorithm exactly conserve the above mentioned four quantities, if the new particles are all located in the same cell as the old particle. If one of the new particles is expected to be placed in a neighboring cell, the splitting is not implemented.

We also conduct the coalescence of particles. This algorithm is also simple. In our code, we choose two particles labeled by 1 and 2 that are located in the same cell and have same charges $q_1 = q_2 = q$ (that is, same masses $m_1 = m_2 = m$), and proximate velocities \mathbf{v}_1 and \mathbf{v}_2 which satisfy $|\mathbf{v}_2 - \mathbf{v}_1| < \alpha v_{th}$, where v_{th} is the thermal velocity defined by $v_{th} \equiv \sqrt{2T/m}$ (T is temperature), and α is a small value which is set as $\alpha = 0.1$ in our code unless otherwise mentioned. The new particle labeled 0 has charge $q_0 = 2q$, mass $m_0 = 2m$, position $\mathbf{x}_0 = (\mathbf{x}_1 + \mathbf{x}_2)/2$, and velocity $\mathbf{v}_0 = (\mathbf{v}_1 + \mathbf{v}_2)/2$ (see Figure 2.2b). However, the coalescence process does not exactly conserve the total energy of particles and the distribution function (Lapenta, 2002). The difference in kinetic energy of particles between before and after the coalescence is found to be under $25\alpha^2$ percent of mv_{th}^2 , so that the error that arises during one coalescence is within 0.5% of the thermal energy of particles with mass m in our code ($\alpha = 0.1$). Nonetheless, we hardly conduct the particle coalescence (usually once in a few hundred time steps), and never choose the particles in the most refined cells to avoid the numerical errors in physically important regions.

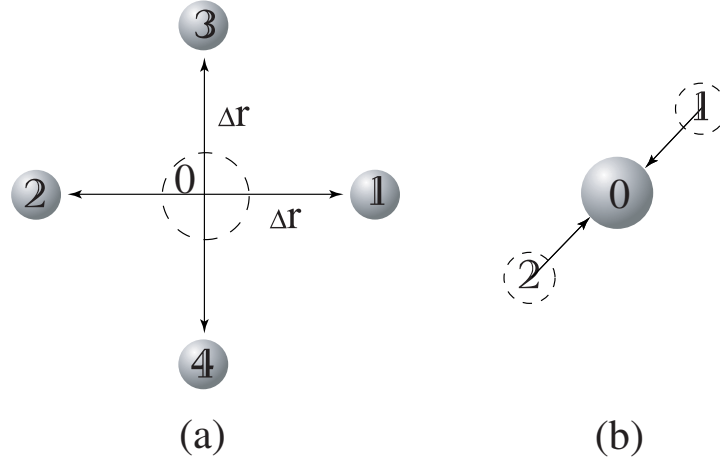


Figure 2.2: Particle splitting and coalescence method in the two-dimensional system. The splitting process in (a) subdivides a particle labeled 0 into four particles numbered 1 to 4, while the coalescence process in (b) joins two particles numbered 1 and 2 and generates a new particle labeled 0 at the midpoint.

2.2.3 Particle and Force Weighting within the Hierarchical Cell

We use the standard PIC algorithm to accumulate the charge and current densities onto each cell corner and interpolate the force on a cell corner to a particle. The charge and current that a particle located in a cell carries are assigned to the four cell corners in the following forms,

$$\rho_{l,m}^n = \sum_s \sum_j q_{sj} S_L(\mathbf{x}_{sj}^n - \mathbf{X}_{l,m}), \quad (2.1)$$

$$\mathbf{j}_{l,m}^{n+1/2} = \sum_s \sum_j q_{sj} \mathbf{v}_{sj}^{n+1/2} \frac{S_L(\mathbf{x}_{sj}^n - \mathbf{X}_{l,m}) + S_L(\mathbf{x}_{sj}^{n+1} - \mathbf{X}_{l,m})}{2}, \quad (2.2)$$

where q_{sj} , \mathbf{x}_{sj}^n , and \mathbf{v}_{sj}^n are the charge, position, and velocity of j -th particle of species s (ion and electron) at time $n\Delta t$ (Δt is a time interval and equivalent for all particles), respectively, and $\mathbf{X}_{l,m}$ represents the spatial position ($l\Delta_L, m\Delta_L$) of a cell corner. $S_L(\mathbf{x})$ is the shape function and defined by using the cell size Δ_L on each refinement level L in the form,

$$S_L(x, y) = \begin{cases} \frac{(\Delta_L - |x|)(\Delta_L - |y|)}{\Delta_L^2} & \text{if } |x| \leq \Delta_L \text{ and } |y| \leq \Delta_L \\ 0 & \text{otherwise.} \end{cases} \quad (2.3)$$

Each particle is belonging to the finest oct including the particle, which means that it is only the oct that has a direct connection to the particle without passing through the other octs. However, we solve Maxwell's equations and the Poisson equation on every

refinement level independently as described in § 2.2.4, so that the charge and current densities must be assigned onto every cell regardless of whether or not the oct including the cell has a pointer to a particle. This assignment process using equations (2.1) and (2.2) is very heavy and time consuming. So we do not adopt this manner for all the cells. Alternatively this process is carried out only for the cells belonging to the octs that have direct pointers to the particles locating in the cells, and the following operation is conducted for the other cells,

$$A_{l,m}^L = \frac{1}{16} \{ 4A_{2l,2m}^{L+1} + 2(A_{2l-1,2m}^{L+1} + A_{2l,2m-1}^{L+1} + A_{2l+1,2m}^{L+1} + A_{2l,2m+1}^{L+1}) + (A_{2l-1,2m-1}^{L+1} + A_{2l-1,2m+1}^{L+1} + A_{2l+1,2m-1}^{L+1} + A_{2l+1,2m+1}^{L+1}) \}, \quad (2.4)$$

where $A_{l,m}^L$ is a physical quantity (charge density and current density in the current case) at the spatial position of $(l\Delta_L, m\Delta_L)$ on the level L cells. The charge and current densities calculated by the use of equation (2.4) is found to be identical to those derived by equations (2.1) and (2.2), if they are known on the finer cells. This procedure is very fast compared with equations (2.1) and (2.2).

The electromagnetic fields at the positions of the level L particles are interpolated from the cell corners on the refinement level L in order to calculate the forces that works on the particles. The interpolation is also implemented by using the PIC algorithm:

$$\mathbf{E}^L(\mathbf{x}_{sj}) = \sum_l \sum_m \mathbf{E}_{l,m}^L S_L(\mathbf{x}_{sj} - \mathbf{X}_{l,m}), \quad (2.5)$$

$$\mathbf{B}^L(\mathbf{x}_{sj}) = \sum_l \sum_m \mathbf{B}_{l,m}^L S_L(\mathbf{x}_{sj} - \mathbf{X}_{l,m}), \quad (2.6)$$

where $\mathbf{E}_{l,m}^L$ and $\mathbf{B}_{l,m}^L$ are the electric and magnetic fields at the position of $(l\Delta_L, m\Delta_L)$ on the refinement level L , respectively.

2.2.4 Integration of the Field Equations

We use the complete set of Maxwell's equations to derive the electromagnetic fields. The time advancements of the electric field \mathbf{E} and magnetic field \mathbf{B} are described by Ampère's law and Faraday's law, respectively, that is,

$$\frac{\partial \mathbf{E}}{\partial t} = c^2 \nabla \times \mathbf{B} - \frac{1}{\epsilon_0} \mathbf{j}, \quad (2.7)$$

$$\frac{\partial \mathbf{B}}{\partial t} = -\nabla \times \mathbf{E}, \quad (2.8)$$

where c is the velocity of light, and ε_0 is the dielectric constant in vacuum. The time differences of equations (2.7) and (2.8) are,

$$\frac{\mathbf{E}^{n+1} - \mathbf{E}^n}{\Delta t} = c^2 \nabla \times \tilde{\mathbf{B}}^{n+1/2} - \frac{1}{\varepsilon_0} \mathbf{j}^{n+1/2}, \quad (2.9)$$

$$\frac{\mathbf{B}^{n+1} - \mathbf{B}^n}{\Delta t} = -\nabla \times \tilde{\mathbf{E}}^{n+1/2}, \quad (2.10)$$

where,

$$\tilde{\mathbf{E}}^{n+1/2} = \frac{\mathbf{E}^n + \mathbf{E}^{n+1}}{2}, \quad (2.11)$$

$$\tilde{\mathbf{B}}^{n+1/2} = \frac{\mathbf{B}^n + \mathbf{B}^{n+1}}{2}. \quad (2.12)$$

Here, the superscripts denote the time levels.

The initial fields \mathbf{E}^0 and \mathbf{B}^0 are determined self-consistently with the spatial distributions of the initial charge and current densities. To advance the field data, one eliminates \mathbf{B}^{n+1} in equation (2.9) by the use of equations (2.10), (2.11), and (2.12), and obtains,

$$\begin{aligned} \left(1 + \frac{c^2 \Delta t^2}{4} \nabla \times \nabla \times\right) \mathbf{E}^{n+1} &= \left(1 - \frac{c^2 \Delta t^2}{4} \nabla \times \nabla \times\right) \mathbf{E}^n \\ &+ c^2 \Delta t \nabla \times \mathbf{B}^n - \frac{\Delta t}{\varepsilon_0} \mathbf{j}^{n+1/2}. \end{aligned} \quad (2.13)$$

The right-hand side consists of the known fields and currents, while the left-hand side has the elliptic operator. Since the boundaries of the refined regions can have an arbitrary shape in our algorithm, methods to solve the equation are restricted and we choose the conjugate gradient method which is one of the relaxation methods (Press et al., 1992). If \mathbf{E}^{n+1} is obtained from equation (2.13), then \mathbf{B}^{n+1} is calculated from equations (2.10) and (2.11).

However, the assignments of the charge and current densities by using equations (2.1) and (2.2), or equivalently equation (2.4), may violate the continuity equation,

$$\frac{\partial \rho}{\partial t} + \nabla \cdot \mathbf{j} = 0. \quad (2.14)$$

If this equation is not satisfied, the straightforward integration of equations (2.7) and (2.8) will lead to the evolution of nonphysical fields that do not satisfy $\nabla \cdot \mathbf{E} = \rho/\varepsilon_0$. Thus we need to make a correction to ensure that $\nabla \cdot \mathbf{E} = \rho/\varepsilon_0$ is maintained (Langdon and Lasinski, 1976). If \mathbf{E} is a corrected electric field and $\overline{\mathbf{E}}$ is that computed from equation (2.7), we assume $\mathbf{E} = \overline{\mathbf{E}} - \nabla \delta \phi$. Then $\delta \phi$ is calculated by solving the Poisson

equation,

$$-\nabla^2 \delta\phi = \left(1 + \frac{\Delta_L^2}{6} \nabla^2\right) \frac{\rho}{\varepsilon_0} - \nabla \cdot \overline{\mathbf{E}}. \quad (2.15)$$

The first term of the right-hand side is worth noticing. The second term in the parentheses arises from the truncation error of the second-order central differences of $\nabla \cdot \mathbf{E}$. $\nabla \cdot \overline{\mathbf{E}}$ in the difference equation has the truncation error within the second order in space ($\sim o(\Delta_L^2)$), while the replacement of $\nabla \cdot \mathbf{E} = \rho/\varepsilon_0$ has no truncation so that no errors are included. This difference in truncation error can yield nonphysical electrostatic field because the error can become the source in the Poisson equation. If the difference form of $\nabla \cdot \mathbf{E}$ in one-dimensional system is given by $(E_{x,i+1} - E_{x,i-1})/2\Delta_L$ (the subscripts $i+1$ and $i-1$ denote the positions of cell corners), this term is approximated in the following form in the spatial fourth-order accuracy,

$$\frac{E_{x,i+1} - E_{x,i-1}}{2\Delta_L} \simeq \left. \frac{\partial E_x}{\partial x} \right|_i + \frac{\Delta_L^2}{6} \left. \frac{\partial^3 E_x}{\partial x^3} \right|_i. \quad (2.16)$$

The second term of the right-hand side of the equation expresses the truncation error within the spatial second order. We add this term explicitly. Since $\partial E_x/\partial x = \rho/\varepsilon_0$ is exactly satisfied, the right-hand side of this equation becomes the first term of the right-hand side of equation (2.15). In two- or three-dimensional system, equation (2.15) is also satisfied within the second-order accuracy. The Poisson equation is solved by using the conjugate gradient method again.

In our code, the electromagnetic fields are first calculated from equations (2.13) and (2.10) on the base level (L_B) cells, because the boundary conditions at the edge of the simulation area are assumed to be given. The solutions are interpolated onto the buffer cell corners on the next level cells as the boundary conditions as shown in Figure 2.3 (Yahagi and Yoshii, 2001). The interpolations are simply performed in the linear form,

$$\begin{aligned} A_{2l,2m}^{L+1} &= A_{l,m}^L, \\ A_{2l+1,2m}^{L+1} &= \frac{1}{2}(A_{l,m}^L + A_{l+1,m}^L), \\ A_{2l,2m+1}^{L+1} &= \frac{1}{2}(A_{l,m}^L + A_{l,m+1}^L), \\ A_{2l+1,2m+1}^{L+1} &= \frac{1}{4}(A_{l,m}^L + A_{l+1,m}^L + A_{l,m+1}^L + A_{l+1,m+1}^L). \end{aligned} \quad (2.17)$$

Then the electromagnetic fields are solved on this level ($L_B + 1$) cells by the use of equations (2.13) and (2.10). These solutions are also interpolated to the buffer cell corners on the next level cells, and the procedure is recursively carried out until the solutions on the dynamic range level (L_D) cells are obtained. After then, the field data on the L_D cells

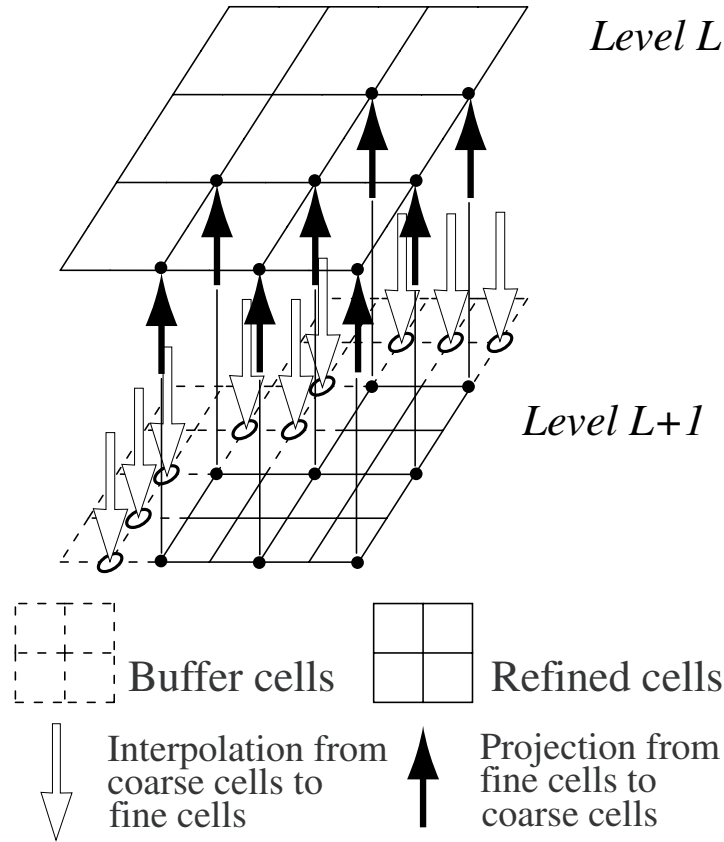


Figure 2.3: Interactions of the field data between the levels L and $L + 1$. The solutions on the level L cells are interpolated onto the buffer cell corners on the level $L + 1$ cells as the boundary conditions. The electromagnetic fields solved on the level $L + 1$ cells are in turn projected to the level L cells.

are projected onto the $L_D - 1$ cells, and the process are also recursively proceeded until the data on the L_B cells are replaced (see Figure 2.3). The projections are performed by using equation (2.4) which is found to eliminate the aliasing. Finally, the Poisson solver described in equation (2.15) must be executed to maintain $\nabla \cdot \mathbf{E} = \rho/\varepsilon_0$ on each level cells. The electromagnetic fields obtained by this procedure without recalculating under the corrected boundary conditions, however, do not give proper solutions on each refinement level, because they are not continuously differentiable at the boundaries of the refined regions (Huang and Greengard, 2000; Vay et al., 2004). Nevertheless, the test simulations described in § 2.3 indicate that numerical errors in association with the cell refinement are almost negligible, so that we consider that the influence of the inconsistency in the field solutions between refined regions is not significant. More accurate treatment of the elliptic equations will be examined in the future work.

2.2.5 Integration of the Equations of Motion

The initial particle distribution in velocity space is chosen to be Maxwellian or shifted-Maxwellian. The Maxwell's distribution is obtained using the Box-Muller method (Press et al., 1992), in which particle velocities with a thermal velocity v_{th} are described in the form,

$$\begin{aligned} v_1 &= v_{th} \sqrt{-2 \ln x_1} \cos 2\pi x_2, \\ v_2 &= v_{th} \sqrt{-2 \ln x_1} \sin 2\pi x_2, \end{aligned} \quad (2.18)$$

where x_1 and x_2 are the uniform random numbers. The velocities v_1 and v_2 are independent of each other.

The particle equations of motion to be integrated are,

$$\frac{d\mathbf{v}_{sj}}{dt} = \frac{q_{sj}}{m_{sj}} (\mathbf{E}(\mathbf{x}_{sj}) + \mathbf{v}_{sj} \times \mathbf{B}(\mathbf{x}_{sj})), \quad (2.19)$$

$$\frac{d\mathbf{x}_{sj}}{dt} = \mathbf{v}_{sj}, \quad (2.20)$$

where, m_{sj} is the mass of j -th particle of species s . \mathbf{E} and \mathbf{B} must be those on the cells whose level is the same as the particle level. The time differences of equations (2.19) and (2.20) are,

$$\begin{aligned} \frac{\mathbf{v}_{sj}^{n+1/2} - \mathbf{v}_{sj}^{n-1/2}}{\Delta t} &= \frac{q_{sj}}{m_{sj}} \left(\mathbf{E}^n(\mathbf{x}_{sj}^n) + \frac{\mathbf{v}_{sj}^{n+1/2} + \mathbf{v}_{sj}^{n-1/2}}{2} \times \mathbf{B}^n(\mathbf{x}_{sj}^n) \right), \\ \frac{\mathbf{x}_{sj}^{n+1} - \mathbf{x}_{sj}^n}{\Delta t} &= \mathbf{v}_{sj}^{n+1/2}. \end{aligned}$$

Above equations represent a standard second-order leapfrog integration scheme. We use the Buneman-Boris method to calculate $\mathbf{v}_{sj}^{n+1/2}$, in which the electric and magnetic forces are separately treated (Birdsall and Langdon, 1991).

2.3 Test Simulations

2.3.1 Landau Damping of the Langmuir Waves

Our code is firstly checked against the Landau damping of the Langmuir waves that propagate across the refined regions. The initial setting of the Langmuir waves in the two-dimensional system is given as one-dimensional plane waves with an appropriate dispersion relation, which are assumed to propagate in the x direction (the horizontal direction in the simulation area) and to be uniform in the y direction. The boundaries of the system are periodic in both x and y directions. The number of the base level

cells is $N_x \times N_y = 64 \times 64$, unless otherwise mentioned, which means $L_B = 6$. In this and next subsections, we assume the number of refined layers is only one so that $L_D = 7$ in order to avoid considerable numerical noise due to small number of particles per cell in the case that we do not conduct the particle splitting for comparison. In the run including the AMR, we initially subdivide the base level cells that satisfy the condition, $|X_j - l_x/2| < 16\Delta_{L_B}$, where X_j is the central x -coordinate of the j -th cell, and l_x represents the horizontal size of the simulation area. The refined region is assumed to be fixed to the base level region and not changed, even though a wave ridge moves from one place to another as time goes on. Thus we have an interest only in whether the waves propagate properly across the boundaries from the base region to the refined region and vice versa, and the hierarchical cells with the particle splitting-coalescence algorithm are adequately applied to the conventional PIC codes. In the runs including the AMR and particle splitting algorithms, the particles that are located in or enter the refined region can be split into four particles, and the child particles can be carefully coalesced if they move outside the region. Other initial parameters are set as $m_i/m_e = 10^4$, $T_i/T_e = 1.0$, $\omega_{ce}/\omega_{pe} = 1.0$, and $c/v_{th,e} = 10^2$, where m_s and T_s represent the mass and temperature of species s , ω_{ce} and ω_{pe} are the cyclotron frequency and plasma frequency of electrons respectively, and $v_{th,e}$ is the electron thermal velocity defined as $v_{th,e} \equiv \sqrt{2T_e/m_e}$. Adoption of an unrealistic high mass ratio indicates that we have an interest only in the electron scale processes, but not those of the ion scale. The size of the base level cells is set as $\Delta_{L_B} = 1.0 \times 10^{-2}\lambda_e$, where λ_e is the electron inertial length. The time step is chosen $\Delta t\omega_{pe} = 5.0 \times 10^{-3}$ in the whole region. The initial number of particles is 64 per base level cell, so that the total number is approximately 2.6×10^5 .

Figure 2.4 shows the time evolutions of the field energy of the wave component E_x normalized by the initial values. We have examined three cases of $\lambda = 8\Delta_{L_B}$, $12\Delta_{L_B}$, and $16\Delta_{L_B}$, where λ is the wavelength. In the runs of $\lambda = 12\Delta_{L_B}$, the number of cells in the base level is set as $N_x \times N_y = 96 \times 64$ that is compatible with the cyclic boundary conditions in this case. Energy is averaged over the base level cells. The solid, dashed, and dotted lines denote the runs without the AMR, with the AMR but not including the particle splitting, and including both the AMR and particle splitting, respectively. The thick lines represent the theoretical profiles of the growth rate described as $\gamma = \pi\omega_{pe}^2/2n_0k v(\partial f_0/\partial v)_{v=\omega/k}$, which is deduced from the linear analysis of the Landau resonance. Here, n_0 is the plasma number density averaged over the entire simulation area, k is the wavenumber, ω is the angular frequency, and f_0 is the background part of the electron distribution function assumed to be Maxwellian. We find that each simulation result provides a good fit to the theoretical profile at the stage of

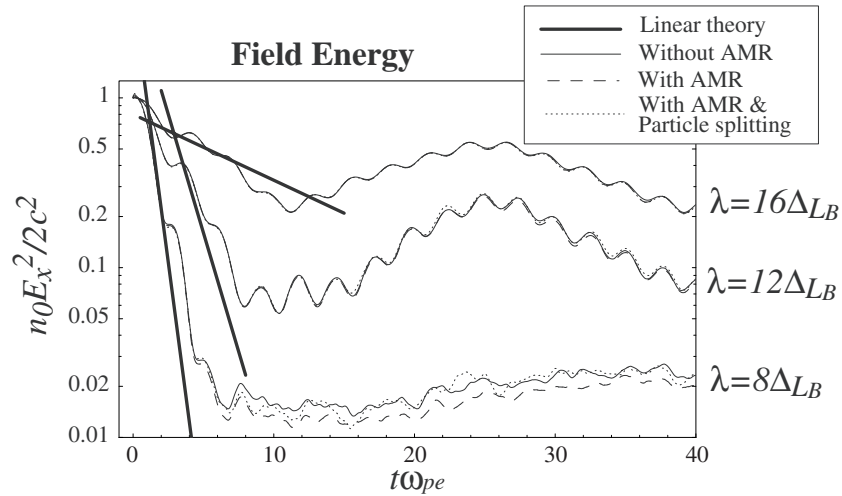


Figure 2.4: Time evolution of the field energy of the Langmuir wave E_x , normalized by the initial values. We examined three cases of wavelength $\lambda = 8\Delta_{LB}$, $12\Delta_{LB}$, and $16\Delta_{LB}$. These energies are averaged over the base level cells. The thick lines denote the theoretical profiles deduced from the linear analysis of the Landau resonance. The solid, dashed, and dotted lines represent the runs without the AMR, with the AMR but not including the particle splitting, and including both the AMR and particle splitting algorithms, respectively.

the linear evolution. We also find that the results of 'With AMR' and 'With AMR & Particle splitting' runs are in good agreement with 'Without AMR' run for each wavelength. We can see a little discrepancy at the nonlinear stage of the case $\lambda = 8\Delta_{LB}$. This is thought to arise from the difference in noise distribution due to thermal plasma and can be affected by the short wave reflections at the boundaries of the refined region. However, the discrepancy is not essential because physical phenomena we try to understand using PIC codes should have much larger amplitudes compared with the noise level. The effects of the wave reflections at the boundaries are described in detail in the next subsection.

2.3.2 Wave Reflections at the Boundaries of the Refined Regions

One of the issues when we combine the PIC and AMR techniques is wave reflections at the boundaries surrounding the refined regions. Wave dispersion relations in the framework using finite-sized particles are different from those in the system using the actual point particles, and dependent on the cloud sizes, that is, the grid spacings in our code (Birdsall and Langdon, 1991). Thus if a wave in a coarse cell region propagates into a refined region or vice versa, the inconsistency in the wave dispersions between

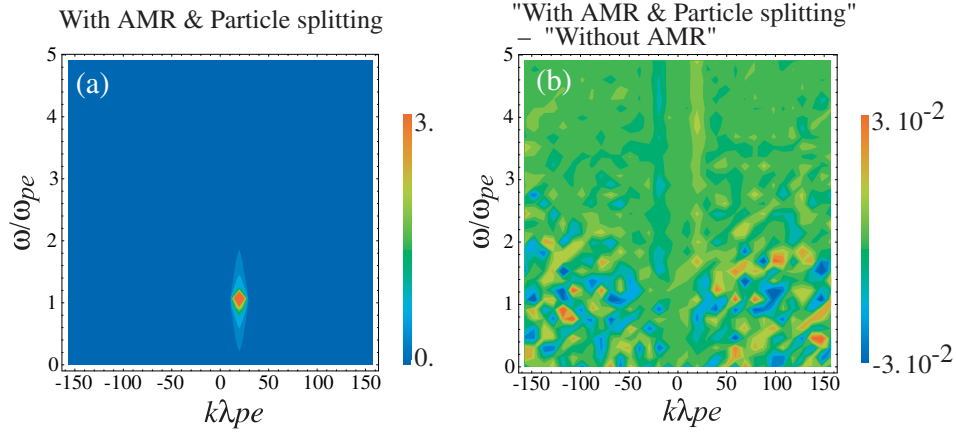


Figure 2.5: (a) Wave spectral density of E_x in the $\omega - k$ space for the 'With AMR & Particle splitting' run in the case of $\lambda = 32\Delta_{LB}$, in which the Landau resonance between the Langmuir wave and the background electrons is negligible. (b) Difference in wave spectral density between the runs of 'With AMR & Particle splitting' and 'Without AMR'. The wave lengths are again $\lambda = 32\Delta_{LB}$.

the hierarchical cell layers can cause wave reflections at the boundary. In order to check whether the reflections are significant, we test again the Langmuir waves that propagate across the boundaries. The initial settings of the hierarchical cells and plasma condition are the same as those in the previous subsection. In order to avoid wave damping due to the Landau resonance, we examine the relatively long wavelength, $\lambda = 32\Delta_{LB}$, of which the phase velocity is much larger than the electron thermal velocity, so that the resonance between the Langmuir waves and background electrons is very weak.

In Figure 2.5(a), the wave spectral density of E_x in the $\omega - k$ space is shown for the run including the AMR and particle splitting processes. Strong peak that arises at $(k, \omega) \simeq (20\lambda_e^{-1}, \omega_{pe})$ represents the normal Langmuir wave initially loaded. If the wave reflects at the boundaries of the refined region, the reflected wave should have strong peak at $(k, \omega) \simeq (-20\lambda_e^{-1}, \omega_{pe})$. However, such a peak is not shown in Figure 2.5(a). The difference in wave spectral density between the 'With AMR & Particle splitting' and 'Without AMR' runs is described in Figure 2.5(b). This difference is thought to represent any wave modulation caused by the presence of the refined cells. However, the scale of colour contour in Figure 2.5(b) is two order smaller than that in Figure 2.5(a), which indicates that the modulations including the wave reflections at the boundaries are very small, if any, compared with the source wave amplitude and can be masked by the thermal fluctuations.

2.3.3 Nonlinear Evolution of the Plasma Sheet

In this subsection, we show the electron dynamics that evolves nonlinearly from the initial plasma sheet. We use the Harris-type current sheet (Harris, 1962) as an initial condition, which is given as $B_x(z) = -B_0 \tanh(z/\lambda)$, where λ is the half width of the initial plasma sheet. We set as $\lambda = 0.5\lambda_{i0}$, where λ_{i0} is the ion inertial length defined by the initial plasma sheet density, n_{ps} . In addition to the equilibrium, we put a small perturbation of the form,

$$\begin{aligned} B_{xp}(x, z) &= -2\delta/\lambda \cos(2\pi x/l_x) \operatorname{sech}^2(z/\lambda) \tanh(z/\lambda) \\ B_{zp}(x, z) &= 2\pi\delta/l_x \sin(2\pi x/l_x) \operatorname{sech}^2(z/\lambda), \end{aligned} \quad (2.21)$$

where δ is given as $\delta = 0.03B_0\lambda_{i0}$ in the current case, so that the initial value of the reconnected magnetic field defined by $\psi \equiv \int_0^{l_x} |B_z(x, z=0)| dx$ is only $0.12 B_0\lambda_{i0}$, where l_x is the system size in the x direction. Furthermore, we add the background plasma such as $n_b = n_{b0} \tanh^2(z/\lambda)$ in order to describe the lobe plasma in the Earth magnetotail. Here, n_{b0} is the asymptotic lobe density and $n_{b0} = 0.044n_{ps}$ is loaded in the current runs. We do not give any perturbation in the initial current density consistent with the initial field perturbation. However, once the simulation starts, the initial current profile is quickly modified to adjust the field perturbation. As a result, a thinner current sheet is formed around the center of the simulation area, so that the tearing instability selectively develops therein. The system size is $l_x \times l_z = 15.4\lambda_{i0} \times 15.4\lambda_{i0}$, we assume the periodic boundary in the x direction and the conducting wall in the z direction, that is, the normal component of the electric field (E_z) and the tangential components of the magnetic field (B_x, B_y) has no gradients and the charge and current densities are vanished at the z boundaries. The initial plasma condition is $m_i/m_e = 100$, $T_{i,ps}/T_{e,ps} = 8.0$, $T_{i,lobe}/T_{e,lobe} = 1.0$, $T_{e,lobe}/T_{e,ps} = 1.0$, and $c/v_{th,e} = 5.0$, where $T_{s,ps}$ and $T_{s,lobe}$ are the temperatures of the species s at the central plasma sheet and the lobe region, respectively. Time step is $\Delta t\omega_{ci} = 8.0 \times 10^{-4}$ for all particles and refined regions in order to satisfy the Courant condition on the level L_D cells, where $\omega_{ci} = eB_0/m_i$ is the ion cyclotron frequency in the asymptotic lobe region. The cell shape is assumed to be square in the current runs.

We examine three runs for comparison: 'Without AMR', 'With AMR', and 'With AMR & Particle splitting' runs. Table I shows information on these three runs, showing whether the AMR or particle splitting algorithms are used, the base level (L_B), the dynamic range level (L_D), the number of cells, and the number of particles. In the 'Without AMR' run, the whole simulation area is initially covered only by the fine cells with level $L = 10$ and the number of particles is large enough to suppress the numerical noise even in the fine cells. The numbers of cells and particles are not changed during

Table I: Simulation information.

Run	AMR	Particle splitting	L_B	L_D	Total number of cells	Total number of particles
Without AMR	No	No	10	10	1.0×10^6	2.2×10^7
With AMR	Yes	No	7	10	8.4×10^4 ^a	2.2×10^7
With AMR & Particle splitting	Yes	Yes	7	10	9.1×10^4 ^a	4.8×10^6 ^a

^aAveraged value over the run.

the run, so that we assume results of the 'Without AMR' run are identical with those in conventional PIC simulations. In the 'With AMR' run, the AMR processes are included but the particle splitting is not implemented. Thus the number of cells is greatly reduced according to the refinement condition described later, but the number of particles is the same as the 'Without AMR' run. Finally, the 'With AMR & Particle splitting' run includes both the AMR and particle splitting processes, so that the numbers of cells and particles are reduced and changed dynamically in association with the evolution of the plasma sheet. The refinement condition is defined by three physical values. The first is the local electron Debye length, $\lambda_{De} = v_{th,e}/\sqrt{2}\omega_{pe}$, which is required to avoid a numerical heating of local plasma, where ω_{pe} is the electron plasma frequency. We use the initial value of $v_{th,e}$ for calculation of λ_{De} , because electrons are expected to be heated in the region where the electron dynamics is important, that is, we use the minimum value of λ_{De} . The second is the out-of-plane electron flow velocity (V_{ey}), because the inertial term in the generalized Ohm's law gets dominant in the region where the electron flow is strong, so that the dissipation of the magnetic field becomes strong and higher resolution is required. The third is the in-plane electron current density ($j_{exz} = \sqrt{j_{ex}^2 + j_{ez}^2}$), which is required because strong currents can excite microinstabilities so that high resolution is needed (e.g., Fujimoto and Machida, 2003). In each time step, if λ_{De} , V_{ey} , and j_{exz} calculated at the center of a cell satisfy the condition, $\Delta_L \geq 2.0\lambda_{De}$ or $V_{ey} > 2.0V_A$ or $j_{exz} > 0.5en_{ps}V_A$, the cell is subdivided and four child cells are produced, otherwise, the child cells are removed if any. Here, $V_A = B_0/\sqrt{\mu_0 n_{ps} m_i}$ is the Alfvén velocity, and μ_0 is the magnetic permeability in vacuum. The process begins from the base level cells and proceed up to the level $L_D - 1$ cells. However, for the level $L_D - 1$ cells we do not impose the criterion on λ_{De} in order to avoid making the level L_D cell region patchy. The particle splitting is performed only for the background particles with level except for L_D in the present runs. The particle coalescence algorithm is also implemented for the background particles once in a few hundred time steps, but we never choose particles in the level L_D cells to avoid the numerical errors in physically important regions.

Time evolutions of the reconnected magnetic flux ψ are shown in Figure 2.6 for the three runs: the 'Without AMR' (black solid line), 'With AMR' (black dashed line), and 'With AMR & Particle splitting' (black dotted line) runs. We found that, although the runs with the AMR require slightly more time before the onsets of fast reconnection occur, each run has the almost identical gradient so the same reconnection rate after the onset. Furthermore, the saturation levels for the runs with the AMR are clearly in agreement with that for the 'Without AMR' run. Thus we can say that the fast reconnection processes described in the three runs are physically identical, so that the adaptation of the AMR and particle splitting algorithms to the conventional PIC codes is successful. We think that the discrepancy of the onset time is caused by the difference in the noise level around the central current sheet at the initial stage in each run. Actually the initial cell size around the central current sheet in the runs with the AMR is twice of that in the 'Without AMR' run, because we do not impose the criterion on λ_{De} for the level $L_D - 1$ cells. Thus the number of particles per cell is increased four times in the former, which indicates that the initial noise level around the central current sheet is lower in the runs with the AMR. In order to make sure whether this reasoning is correct or not, we also examined a simulation which imposes the refinement criterion on λ_{De} for the level $L_D - 1$ cells. In this case, the criterion on λ_{De} is given as $\Delta_L \geq 1.4\lambda_{De}$, instead of $\Delta_L \geq 2.0\lambda_{De}$, only for the level $L = L_D - 1$ cells to avoid the patchy refined regions with level L_D . The results for two cases are shown in Figure 2.6. One describes the run using only the AMR technique (red dashed line) and the other shows that using the AMR and particle splitting techniques (red dotted line). It is found that these two runs are in good agreement with the run without the AMR, which indicates that the initial noise level around the central plasma sheet is very crucial to determine the time when the onsets of magnetic reconnection occur. Indeed, it is very difficult to discuss the time scale in which magnetic reconnection grows from noise to a significant size, because it is strongly dependent not only on the initial noise level but also on many other conditions specific to the system (e.g., Shay et al., 2004). Thus we do not treat such a problem in this paper. We only compare the description of fast reconnection, which allows us to start simulations with coarser cells around the central plasma sheet.

Efficiency of our code is measured by the elapsed time to complete each run, which is presented in Figure 2.7. Our code including both the AMR and particle splitting algorithms is shown clearly to be very efficient compared with the conventional PIC code without the AMR. This efficiency is achieved by reducing the numbers of cells and particles greatly (see Table I).

Figure 2.8 shows the evolution of the out-of-plane current density (J_y) for the run in-

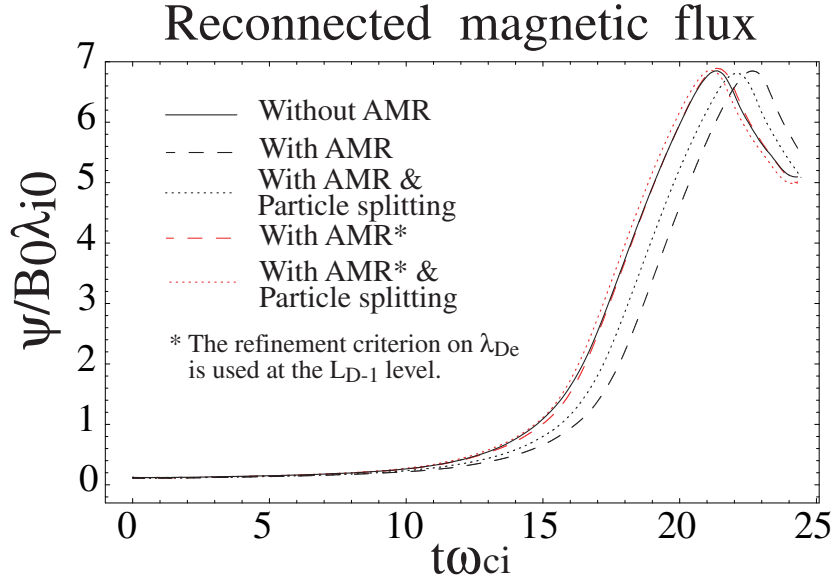


Figure 2.6: Time evolutions of the reconnected magnetic flux defined as $\psi \equiv \int_0^{l_x} |B_z(x, z = 0)| dx$, where l_x is the system size in the x direction. The black solid line shows the result of the non-AMR run, where the whole simulation area is covered by fine cells having enough background particles, while the black dashed line denotes the run using only the AMR technique so that the number of particles is the same as in the non-AMR run. The black dotted line is the result including both the AMR and particle splitting algorithms, so that the number of background particles is greatly reduced compared with that in the former two cases. In addition to them, two runs in which the refinement criterion on λ_{De} is used also at the $L_D - 1$ level are plotted in red lines.

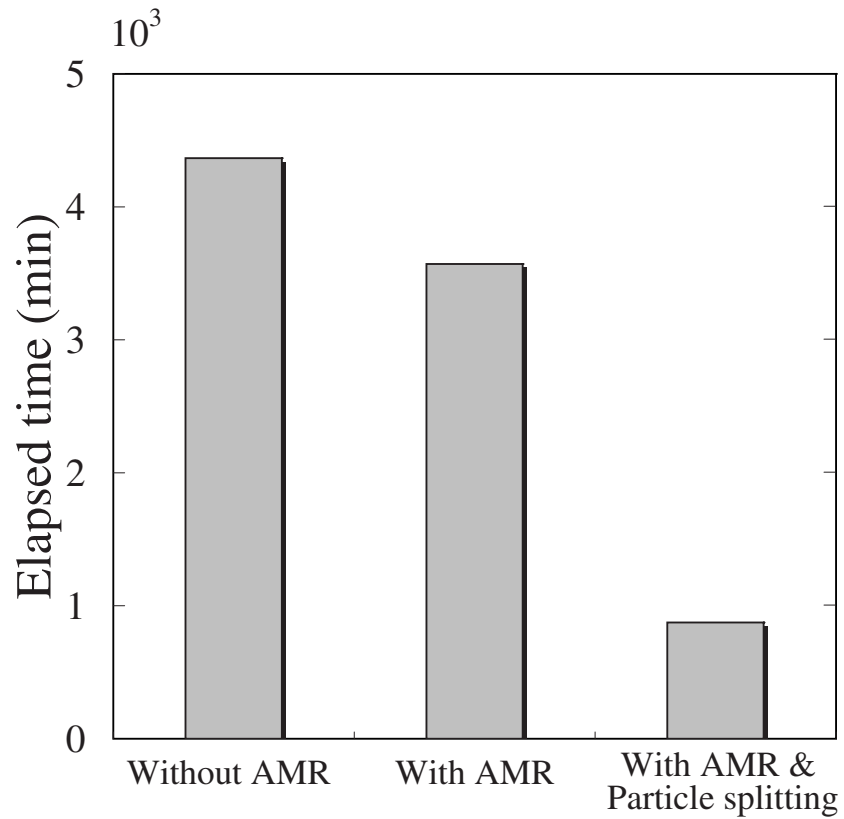


Figure 2.7: Elapsed time to complete simulations for the cases of 'Without AMR', 'With AMR', and 'With AMR & Particle splitting' runs, which correspond to the solid, dashed, and dotted lines in Figure 2.6, respectively. Each run has the same time steps. 'With AMR & Particle splitting' run is faster than 'Without AMR' and 'With AMR' runs by a factor of 5.0 and 4.1, respectively.

cluding the AMR and particle splitting algorithms. A strong thin current sheet is formed in the vicinity of the X-line ($t\omega_{ci} = 14.72$) and then fast reconnection occurs (see Figure 2.6). After the initially loaded plasma in the current sheet is carried away from the central region, the background lobe plasma enters the diffusion region and quasi-steady electron diffusion region is produced ($t\omega_{ci} = 17.92, 20.48$). In the electron diffusion region, electrons are unmagnetized from the ambient magnetic field, and conduct the meandering motions with acceleration due to the out-of-plane electric field, which generate a double-peaked current sheet therein as clearly shown in the figure. Similar properties are described also in other full particle simulations on magnetic reconnection (e.g., Shay et al., 2001; Pritchett, 2001; Hoshino et al., 2001b). The hierarchical cell distributions in association with the current sheet evolution are shown in the right-hand column of Figure 2.8. We find that the finest cells are only distributed around the diffusion region, separatrices extending from the X-line, and plasmoid, where the electron kinetic effects are expected to be important.

Figure 2.9 displays the profiles of (a) the number density of electrons (n_e), (b) the out-of-plane current density (J_y), (c) the inflow electron velocity (V_{ez}) and $E \times B$ drift velocity (dashed line), and (d) the out-of-plane electric field (E_y), along the $x/\lambda_{i0} = 7.9$ axis at the time $t\omega_{ci} = 17.92$ for the run including the AMR and particle splitting algorithms. The electron diffusion region can be defined as an area where the electron bulk velocity is inconsistent with the local $E \times B$ drift velocity. Thus the area from $z/\lambda_{i0} = -0.34$ to 0.34 is the electron diffusion region in this case. The double-peaked profiles of n_e and J_y inside the electron diffusion region are also shown in Figure 2.9a and b. The peak separation is estimated at $0.3\lambda_{i0}$, which is approximately same as the electron inertial length defined by the electron number density averaged within the electron diffusion region, $n_e/n_{ps} \simeq 0.071$. Shay et al. (2001) has constructed a model around the electron diffusion region, in which v_{ez} at the edge of the electron diffusion region and E_y within the region are given by $v_{ez} \sim B_d/\mu_0 en_e l$ and $E_y \sim -B_d^2/\mu_0 en_e l$ respectively, where B_d is the x component of the magnetic field at the edge of the electron diffusion region and l is the length of the region along the x axis. When we estimate l , we assume that electrons continue to be accelerated along x in the electron diffusion region, so that the electron bulk velocity V_{ex} should be maximized at the edge of the region. In the current case, $B_d/B_0 \simeq 0.29$ and $l/\lambda_{i0} \simeq 2.0$ are estimated from our simulation results, so that $v_{ez}/V_A \simeq 2.1$ and $E_y/V_A B_0 \simeq -0.61$ are derived, which are approximately consistent with our results described in Figure 2.9c and d. Thus the electron dynamics described in the run including the AMR and particle splitting algorithms is in good agreement with the conventional model.

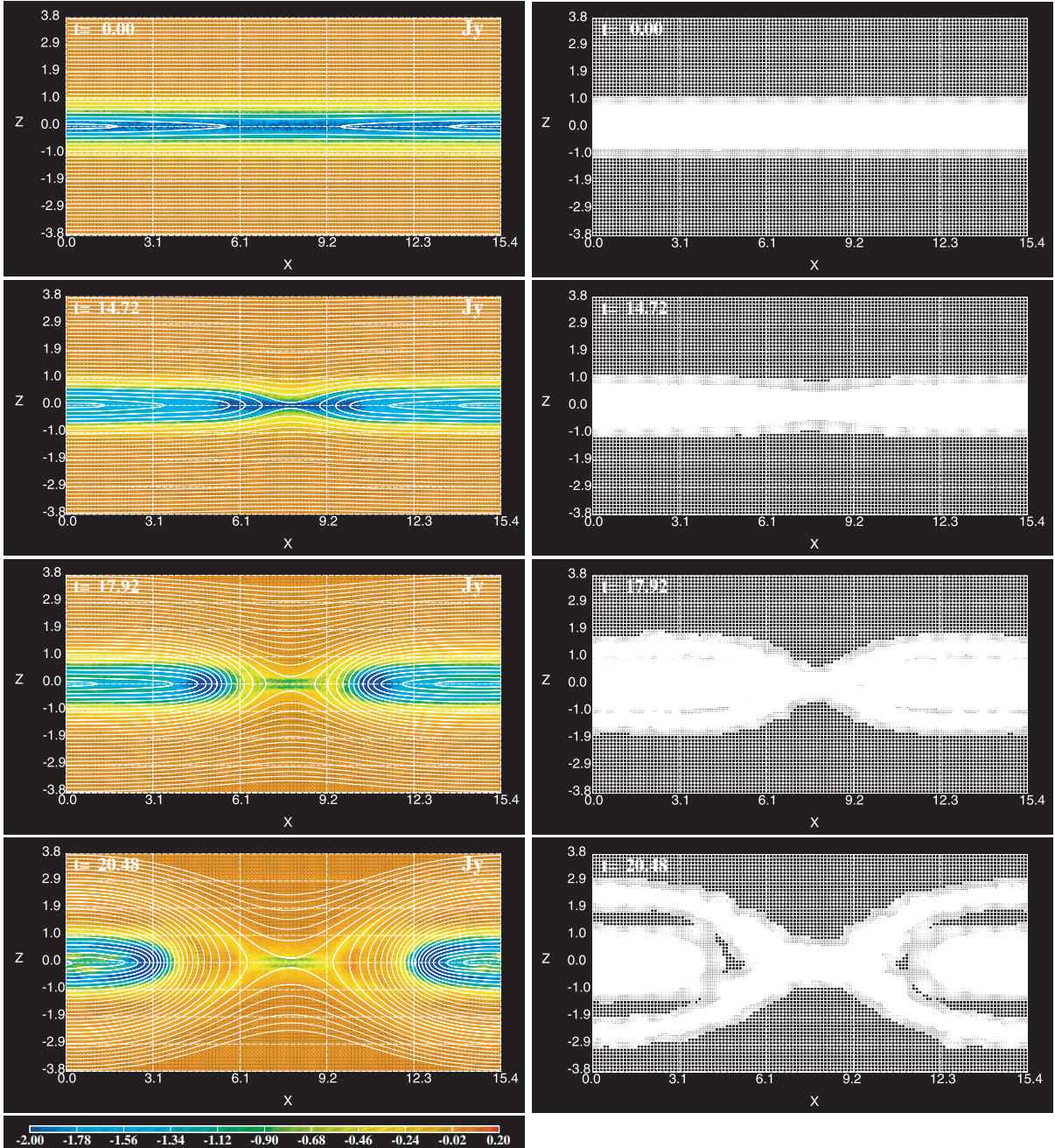


Figure 2.8: Example of the evolution of the hierarchical cell distribution associated with the current sheet evolution for the run with the AMR and particle splitting processes. Magnetic field and current density (color-coded) evolutions are shown in the left-hand column and the hierarchical cells at the times corresponding to them are described in the right-hand column. Finest cells are only distributed around the diffusion region, the separatrices extending from the X-line, and the plasmoid, where the electron kinetic effects are expected to be important.

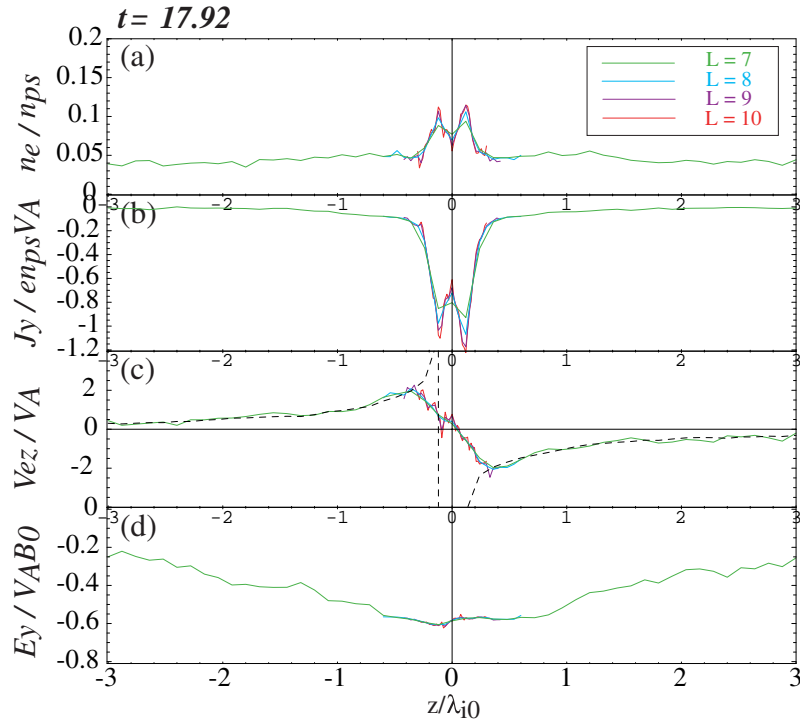


Figure 2.9: Profiles of (a) the number density of electrons, (b) the out-of-plane current density, (c) the inflow electron velocity and $E \times B$ drift velocity (dashed line), and (d) the out-of-plane electric field, along the $x/\lambda_{i0} = 7.9$ axis at the time $t\omega_{ci} = 17.92$ for the same run as in Figure 2.8. The green, blue, purple, and red lines represent the profiles on the level $L = 7, 8, 9,$ and 10 cells, respectively.

2.4 Summary and Discussion

We have described a new electromagnetic full particle code with the AMR and particle splitting algorithms. The AMR technique subdivides and removes cells dynamically in accordance with the refinement criteria and enhances the spatial resolution. On the other hand, the particle splitting algorithm divides particles that locate in finer cells, conserving the ratio of mass to charge, the total momentum, energy, and distribution function of particles, and the moments on grids. The particle splitting is indispensable for adapting the AMR to the electromagnetic particle codes, because the numerical noise increases on the subdivided cells due to the decrease in the number of particles per cell, especially around the X-line formed in association with magnetic reconnection (Fujimoto and Machida, 2005a).

We conduct several test simulations and compare three runs without the AMR, with the AMR, and with the AMR and particle splitting. Test simulations on the propagation of the Langmuir waves indicate that the AMR and particle splitting algorithms are successfully applied to the conventional PIC codes, and we have found that the wave reflections at the boundaries of the refined regions are not essential. The nonlinear evolution of the Harris-type current sheet and the electron dynamics around the X-line using our AMR code are basically the same as those in other reconnection simulations. However, the numbers of cells and particles are greatly reduced in the run including the AMR and particle splitting algorithms, so that the time to complete the simulation is considerably shortened. Thus we conclude that we have realized effectively high-resolution simulations on the evolution of the current sheet by the use of the AMR technique and particle splitting algorithm. Our code enables us to conduct large-scale particle simulations on magnetic reconnection in a wide range of the order $10^4 - 10^5$.

Our next challenge is a massively parallel computation for the AMR code using several computational nodes. Our code at the current version is parallelized only within a node of shared memory processors using OpenMP. It is worth mentioning that the accumulation of the charge and current densities onto each cell corner is parallelized by preparing temporal lists of charge and current densities for each processor. In other words, each processor has private lists of charge and current densities, and assigns particle to the lists independently of the other processors. After a sweep of the particle loop, the charge and current densities assigned to each processor are summed up respectively and substituted into the shared lists. This procedure is effectively parallelized at the expense of the computational memory. Difficulties in parallelizing our code arise mainly from the Poisson solver to calculate $\delta\phi$ by equation (2.15). The relaxation methods as used in the code are not adequate to a parallel computing. This is conceptually because a

global distribution of the source field contributes to each local potential, and technically because the iteration loop repeated until the residual error becomes small enough must be carried out sequentially. In order to avoid solving the Poisson equation, we can use the charge conservation method for example, in which the current density is determined directly from knowledge of charge motion so as to satisfy the charge continuity equation (e.g., Villasenor and Buneman, 1992). The improved version of our code will be discussed in a separate article.

CHAPTER 3

Time Evolutions of the Electron Diffusion Region and the Reconnection Rate in Large and Fully Kinetic System

3.1 Introduction

Magnetic reconnection is widely believed to play an important role in the magnetospheric substorm and solar flares as a fast conversion process of the magnetic energy to plasma kinetic and thermal energies. In reconnection processes, the ideal magnetohydrodynamic (MHD) condition breaks down in the diffusion region arising around a magnetic X-line, where dissipation processes of the magnetic field are significant (Vasyliunas, 1975). In a sufficiently collisional plasma, the resistive MHD theory (Sweet, 1958; Parker, 1963; Petschek, 1964) is valid for describing the diffusion region by parameterizing effects of the classical Coulomb collisions (Spitzer, 1962). However, in the collisionless plasma as seen in the Earth magnetosphere, the magnetic diffusion due to the classical resistivity is too small to drive fast reconnection. In such a system, we need to replace the standard Ohm's law in the resistive MHD by the generalized Ohm's law written as

$$\mathbf{E} + \mathbf{V} \times \mathbf{B} = -\frac{m_e}{e}(\mathbf{V}_e \cdot \nabla)\mathbf{V}_e - \frac{1}{ne} \nabla \cdot \mathbf{P}_e + \frac{1}{ne} \mathbf{J} \times \mathbf{B}, \quad (3.1)$$

where \mathbf{E} is the electric field, \mathbf{B} the magnetic field, \mathbf{J} the current density, n the plasma number density, \mathbf{V}_e the electron flow velocity, \mathbf{P}_e the electron pressure tensor, and m_e the electron mass. The first and second terms in the right-hand side arise from electron inertial effects, and the scale sizes are evaluated as the electron inertial length λ_e and the electron gyroradius λ_{ge} , respectively. The last term represents the decoupling between

ions and electrons, so-called Hall effects, and has a scale size of the ion inertial length λ_i . When the scale length of gradient is much larger than any of these characteristic lengths, the frozen-in condition holds.

In two-fluid system consisting of ions and electrons, the inflowing ions can be decoupled from the ambient magnetic field when they approach the neutral sheet as close as λ_i . Thus the region within λ_i is the diffusion region where the frozen-in condition breaks down. Electrons, however, still remain magnetized at this distance, since their inertia is much smaller than those of ions. Instead, their frozen-in constraint can break down at the distance comparable with the local gyroradius λ_{ge} , within which electrons are expected to perform the meandering motions (e.g., Pei et al., 2001). This non-magnetized region for electrons is called the electron diffusion region. Therefore the diffusion region in the two-fluid system develops two-scale structure, embedding the electron diffusion region within the ion-scale diffusion region.

Inside the diffusion region but outside the electron diffusion region, ions are decoupled from the ambient magnetic field but electrons are still frozen-in to the field and continue to move with the $\mathbf{E} \times \mathbf{B}$ drift motion toward the current sheet. This relative motion between ions and electrons produces currents in the vicinity of the magnetic X-line, forming the Hall current system (Sonnerup, 1979; Terasawa, 1983). On the other hand, the kinetic behavior of electrons becomes important in the electron diffusion region. It has been revealed by using two-dimensional kinetic simulations that the dissipation process in the electron diffusion region is supported by the electron inertia term and the gradient term of the electron pressure tensor in the generalized Ohm's law (3.1) (Cai and Lee, 1997; Hesse and Winske, 1998; Kuznetsova et al., 1998; Hesse et al., 1999; Swisdak et al., 2005). Though reconnecting of the magnetic field actually proceeds in this region, it has been suggested that the electron dynamics should have little or no effect on the reconnection rate (Biskamp et al., 1997; Birn et al., 2001). Instead, ion dynamics can control the reconnection processes so the electron-scale structure. They conclude that a high reconnection rate results from the Hall term in the generalized Ohm's law (3.1), so that the inclusion of the Hall effects is a sufficient condition to achieve fast reconnection. This indicates that three-dimensional effects arising along the current sheet would not be essential for obtaining the high reconnection rate (Huba and Rudakov, 2004). Though recent simulation studies comparing MHD, Hall MHD, hybrid, and full particle simulations confirmed the importance of the Hall effects, the system did not reach steady state and the reconnection rate decreased after it reached a peak value (Shay et al., 2001; Hesse et al., 2001; Pritchett, 2001; Kuznetsova et al., 2001). They attributed the depression to the periodic system in the direction of the initial magnetic

field, in which compressional effects in the magnetic islands could affect the reconnection processes. One of the solutions in order to suppress the boundary effects is to perform the simulations in a large system so that the periodicity is negligible therein.

Such large-scale simulations including the Hall effects were examined using a two-dimensional hybrid code (Shay et al, 1999) and a two-dimensional two-fluid code (Shay et al., 2004). Both results also indicate the importance of the Hall effects for fast reconnection and show a quasi-steady reconnection with the reconnection rate of the order of $0.1V_{A0}B_0$, where V_{A0} and B_0 are, respectively, the Alfvén velocity and the magnetic field defined in the asymptotic lobe region, and the reconnection rate is estimated by the electric field strength along the X-line. However, Karimabadi et al. (2004) recently compared two different hybrid simulations with and without the Hall term under an open boundary condition, and demonstrated that ion kinetic behavior alone could give rise to fast reconnection even in the absence of the Hall effects. Thus the Hall effects may not be necessarily required for fast reconnection.

The present work shows results from 2-1/2 dimensional full particle simulations in a large system, in which both ions and electrons are treated as superparticles. The purpose of this study is to see a long evolution of the diffusion region in a fully kinetic system. The main concern is how the ion dynamics affects the electron-scale structure so the reconnection processes. It is still difficult to conduct large-scale simulations using conventional particle-in-cell (PIC) codes because of limited computer resources. Thus we employed the adaptive mesh refinement (AMR) technique and the particle splitting algorithm to the conventional PIC code (Fujimoto and Machida, 2005b). Adoption of these techniques enables us to perform effectively high-resolution simulations including kinetic processes of magnetic reconnection.

3.2 Simulation Model

The present study employs a 2-1/2 dimensional electromagnetic PIC code with the AMR technique and the particle splitting algorithm, which has been described by Fujimoto and Machida (2005b). The AMR technique subdivides and removes computing cells dynamically in accordance with a refinement criterion and quite effective to achieve high-resolution simulations of phenomena that locally include micro-scale processes. In our code, the spatial resolution is increased by introducing finer cells hierarchically onto the uniform base cells that cover the entire simulation area. If a base cell is refined, four child cells that have half the size of the base cell are generated. These child cells can be also refined in turn and finer cells are produced, and so on. One of the main problems in

developing the electromagnetic PIC codes using the AMR technique is the decrease in the number of particles per cell in the refined region. In order to solve this problem, we subdivide particles residing in the subdivided cells and control the number of particles per cell. We employ the particle splitting algorithm developed by Lapenta (2002), in which the moments on each grid (the charge and current densities), the total charge, mass, momentum, and energy of particles, and the distribution function of particles are retained between before and after the particle splitting. Each cell is needed to have information of the parent, child, and neighboring cells, and the particles residing in the cell. The communication between cells or between a cell and the particles in the cell is supported by a set of pointers, constructing the fully threaded tree structure (Khokhlov, 1998). A refinement level L in the hierarchical cell structure is defined by using the cell size of the level (Δ_L) as $L \equiv \log_2(l_z/\Delta_L)$, where l_z is the vertical size of the two-dimensional simulation area. We use only cells with integer level. More detailed description on our code is shown in Fujimoto and Machida (2005b).

The refinement condition in the current study is defined by three physical values. The first is the local electron Debye length, $\lambda_{De} = v_{th,e}/\sqrt{2}\omega_{pe}$, which is required to avoid a numerical heating of local plasma, where $v_{th,e} = \sqrt{2T_e/m_e}$ is the electron thermal velocity (T_e and m_e are the temperature and mass of electrons, respectively), and ω_{pe} is the electron plasma frequency. We use the initial value of $v_{th,e}$ for calculation of λ_{De} , because electrons are expected to be heated in the region where the electron dynamics is important, that is, we use the minimum value of λ_{De} . The second is the out-of-plane electron flow velocity (V_{ey}), because the inertial term (the first term of the right-hand side) in the generalized Ohm's law (3.1) becomes dominant in the region where the electron flow is strong, so that the dissipation of the magnetic field becomes strong and higher resolution is required. The third is the in-plane electron current density ($J_{exz} = \sqrt{J_{ex}^2 + J_{ez}^2}$), which is required because intense currents can excite microinstabilities so that electron-scale waves are expected to arise. In each time step, if λ_{De} , V_{ey} , and J_{exz} calculated at the center of a cell satisfy the condition, $\Delta_L > 2.0\lambda_{De}$ or $V_{ey} > 2.0V_A$ or $J_{exz} > 0.5en_{ps}V_A$, the cell is subdivided and four child cells are produced, otherwise, the child cells are removed if any. Here, V_A is the Alfvén velocity defined by the initial lobe field (B_0) and plasma sheet density (n_{ps}), and e is the electron charge. The particle splitting is also performed in each time step, but this is done only for the background particles whose initial distribution is described later. We carry out not only particle splitting but also particle coalescence in order to reduce the number of particles in the unrefined region. The particle coalescence algorithm is implemented once in a few hundred time steps for the background particles. In both the particle splitting and

coalescence algorithms, we never choose particles in the most refined (finest) cells to avoid numerical errors in physically important regions. In the present study, the hierarchical cell structure consists of four cell layers.

The initial magnetic field configuration is given as $B_x(z) = -B_0 \tanh(z/\lambda)$, and the corresponding density is $n(z) = n_{ps} \operatorname{sech}^2(z/\lambda)$, where λ is the half width of the initial plasma sheet and set as $\lambda = 0.5\lambda_{i0}$ (λ_{i0} is the ion inertial length defined by n_{ps}). In addition to the equilibrium, a small perturbation is superposed in the form

$$\begin{aligned} B_{xp}(x, z) &= 2a_0/\lambda \operatorname{sech}^2((x - l_x/2)/L') \operatorname{sech}^2(z/\lambda) \tanh(z/\lambda) \\ B_{zp}(x, z) &= -2a_0/L' \operatorname{sech}^2((x - l_x/2)/L') \operatorname{sech}^2(z/\lambda) \tanh((x - l_x/2)/L'), \end{aligned} \quad (3.2)$$

where, l_x is the horizontal length of the simulation area, and a_0 and L' provide the amplitude and horizontal size of the perturbation, respectively. In the present study, $a_0 = 0.15B_0\lambda_{i0}$, $L' = 3.8\lambda_{i0}$, and $l_x \times l_z = 122.9\lambda_{i0} \times 30.7\lambda_{i0}$ are chosen, unless otherwise mentioned. Furthermore, the background plasma is loaded as $n_b(z) = n_{b0} \tanh^2(z/\lambda)$ and $n_{b0} = 0.044n_{ps}$ in order to describe the lobe plasma in the magnetospheric tail. Although there appears a weak pressure imbalance due to this background profile, it is quickly justified without any significant modification of the current sheet structure. Once the simulation starts, the initial plasma sheet density and current profiles are quickly modified to adjust the field perturbation. As a result, a thinner current sheet is formed near the center of the simulation area ($x = l_x/2, z = 0$), so that the tearing instability selectively develops therein. The cell size is $\Delta_{LB} = 0.12\lambda_{i0}$ for the coarsest cells and $\Delta_{LD} = 0.015\lambda_{i0}$ for the finest cells, and the time step is $\Delta t\omega_{ci} = 8.0 \times 10^{-4}$ for all particles and refined regions in order to satisfy the Courant condition on the finest cells, where ω_{ci} is the ion cyclotron frequency defined by the lobe field (B_0). The initial plasma condition is $m_i/m_e = 100$, $T_{i,ps}/T_{e,ps} = 8.0$, $T_{i,lobe}/T_{e,lobe} = 1.0$, $T_{e,lobe}/T_{e,ps} = 1.0$, unless otherwise mentioned, and $c/V_A = 16.7$, where $T_{s,ps}$ and $T_{s,lobe}$ are the temperatures of the species s at the central plasma sheet and the magnetic lobe, respectively, and c is velocity of light. We assume the periodic boundary in the x direction and the conducting wall in the z direction.

3.3 Results

3.3.1 Time Evolution of the Reconnection Rate

The evolution of the reconnected magnetic flux, $\psi = \int_0^{l_x/2} |B_z(x, z = 0)| dx$, is plotted in Figure 3.1a. Here, it is assumed that the X-line is formed at the center of the simulation area ($x = l_x/2, z = 0$). It increases very slowly in the first half of the simulation time, but

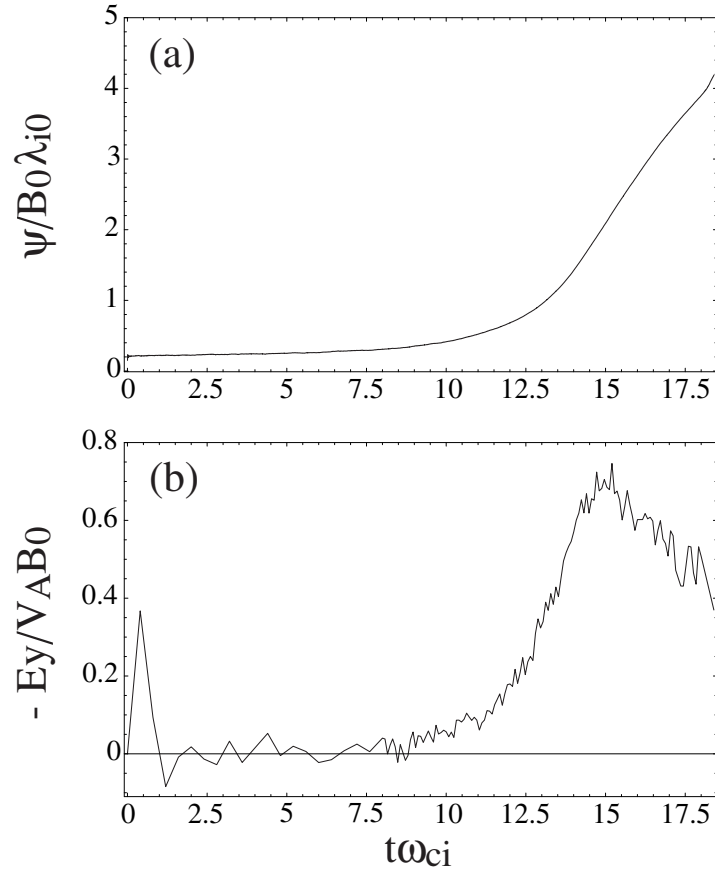


Figure 3.1: Time evolutions of (a) the reconnected magnetic flux, (b) the out-of-plane electric field at the center of the simulation area ($x = l_x/2$, $z = 0$).

develops at drastically high rate after $t\omega_{ci} \approx 12.5$, so that fast reconnection is switched on. The reconnection rate should be given by the instantaneous growth rate of ψ , which is derived from Faraday's law as $\partial\psi/\partial t = -E_y(x = l_x/2, z = 0)$, which expresses the electric field imposed along the X-line. Figure 3.1b shows the time evolution of the out-of-plane electric field at the center of the simulation area. The reconnection rate develops associated with the evolution of the magnetic reconnection until it reaches a peak at $t\omega_{ci} \approx 15$, and a fast reconnection with $|E_y| \sim 0.7V_A B_0 = 0.15V_{A0} B_0$ is achieved. However, after then it starts to decrease and fall to nearly the half of the peak value at the end of the simulation. This time history is similar to those obtained in other particle simulations having smaller simulation areas, in which the periodicity of the system has tended to affect the reconnection rate and slow down reconnection processes (Shay et al., 2001; Hesse et al., 2001; Pritchett, 2001; Kuznetsova et al., 2001). In the present run, however, the simulation area is large enough to describe longer time evolutions of reconnection without the effects of the periodic boundaries. Actually the plasma density at the edge of the simulation area ($x = 0, z = 0$), which is initially set as $n = 1.00n_{ps}$, is only slightly increased to $n = 1.04n_{ps}$ at the end of the simulation. This indicates that the compressive effects in the magnetic island as expected in the periodic system are mostly negligible in the present large system.

3.3.2 Structure Change Around the Electron Diffusion Region

The density profiles along the z direction at $x = l_x/2$ are shown in Figure 3.2b for ions (red solid lines) and electrons (blue solid lines) at two different times: $t\omega_{ci} = 12.8$ (left) and 16.7 (right). At $t\omega_{ci} = 12.8$, both ion and electron density profiles have peaks at $z = 0$ that are reminiscent of the initial equilibrium profiles. On the other hand, at $t\omega_{ci} = 16.7$, electrons have still a peak at $z = 0$ while ion peaks appear at the flanks of the electron peak and a density hole is formed at $z = 0$. The double-peaked structure in the ion density profile as seen at $t\omega_{ci} = 16.7$ indicates that most ions experience meandering motions near the X-line, staying long around the turning points and passing fast around $z = 0$. The red dashed lines in Figure 3.2a denote the density profiles of the background cold ions, which are initially loaded only in the lobe region. Its profile at $t\omega_{ci} = 12.8$ is not yet changed from the initial profile in essence. However, as magnetic reconnection proceeds, the background ions approach toward the X-line and start the meandering motions. It is found that the double-peaked structure at $t\omega_{ci} = 16.7$ is mainly produced by the background ions meandering around the X-line. Because the hot ions initially loaded in the current sheet have large velocity in the out-of-plane direction in order to produce the current supporting the initial magnetic field profile, they can easily

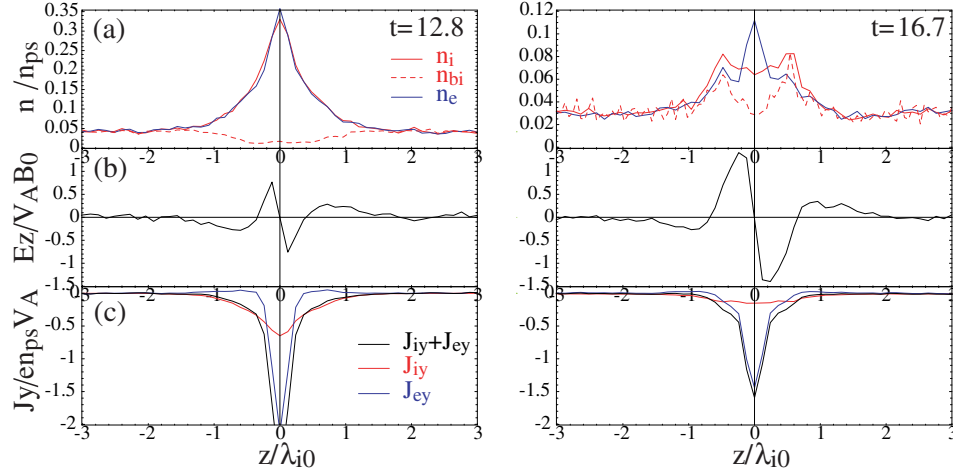


Figure 3.2: Comparison of structures along the z direction through the center of the simulation area ($x = l_x/2$, $z = 0$) at two different times: $t\omega_{ci} = 12.8$ (left) and 16.7 (right). (a) The number densities of ions (red solid lines) and electrons (blue solid lines). The red dashed lines represent the contribution from the background cold ions. (b) The electric field along the z direction. (c) The out-of-plane current densities (black solid lines), which are calculated by summing up the ion and electron current densities (red and blue lines, respectively).

escape from the diffusion region due to the Lorentz force before their meandering motions become dominant. Thus, as the density of the background cold ions dominates that of the plasma sheet ions in the vicinity of the X-line, the double-peaked structure becomes dominant. This structure change occurs around $t\omega_{ci} = 15$ in the present run.

The difference in density peak position between ions and electrons are mainly caused by their inertia difference, and give rise to a strong polarization electric field E_z directing toward the neutral sheet in the electron inflow region. Its profiles along the z direction are shown in Figure 3.2b, and the two-dimensional snapshots are also given in Figure 3.3. We find that the meandering motions of the background ions enhance the amplitude of E_z and broaden its imposed region not only in the z direction but also in the x direction around the X-line. The time evolution of the electric field directing toward the neutral sheet $\overline{E_z} = -z/|z| E_z$, averaged over the electron inflow region ($l_x/2 - 0.2\lambda_{i0} \leq x \leq l_x/2 + 0.2\lambda_{i0}$, $0.25\lambda_{i0} \leq |z| \leq 0.5\lambda_{i0}$), is plotted in Figure 3.4. $\overline{E_z}$ develops after $t\omega_{ci} \approx 13$ as magnetic reconnection proceeds. Especially, its growth rate is enhanced after $t\omega_{ci} \approx 15$, indicating that the background ions carrying out the meandering motions become dominant around the X-line. Figure 3.2c shows the comparison of the out-of-plane current density profiles (black lines), which are calculated by summing up the ion and electron current densities (denoted by red and blue lines, respectively). We find that

the polarization electric field E_z forces the inflow electrons to execute the $\mathbf{E} \times \mathbf{B}$ drift toward the out-of-plane direction and enhances the out-of-plane electron current density in the electron inflow region.

In order to see the role of the enhanced electron current in the electron inflow region, we plot in Figure 3.5 the time evolution of each term in the right-hand side of Ampère's law, $\partial E_y / \partial t = -J_y / \varepsilon_0 + c^2(\partial B_x / \partial z - \partial B_z / \partial x)$, averaged over the electron inflow region ($l_x/2 - 0.2\lambda_{i0} \leq x \leq l_x/2 + 0.2\lambda_{i0}$, $0.25\lambda_{i0} \leq |z| \leq 0.5\lambda_{i0}$). The term contributed by the electron current (blue solid line) decreases until $t\omega_{ci} \approx 13.5$, which results from the thinning of the electron current sheet. Then this term, however, increases again due to the enhancement of the out-of-plane electron drift caused by the polarization electric field. The important point in this figure is that the contribution from the x -gradient of the magnetic field B_z also has a peak at $t\omega_{ci} \approx 13.5$. The absolute value of $\partial B_z / \partial x$ in the electron inflow region reflects a curvature of the magnetic field lines, which is expressed as $\kappa \simeq |B_x / B^2 \partial B_z / \partial x|$ when $|B_z / B| \ll 1$, where $B = \sqrt{B_x^2 + B_z^2}$. Since B_x (not shown) is almost constant after $t\omega_{ci} \approx 14$, κ is mostly proportional to $|\partial B_z / \partial x|$ at its declining phase. Therefore it is found that the curvature of the magnetic field lines decreases as the out-of-plane electron current in the electron inflow region is enhanced. This means that the magnetic field lines in the upstream region tends to be parallel to the x direction, leading to the extension of the electron meandering region along the x direction. Note that the left-hand side of Ampère's law ($\partial E_y / \partial t$, not shown) is mostly zero within the present simulation time in comparison with each term in the right-hand side.

Figure 3.6 shows the snapshots of the out-of-plane electron velocity V_{ey} with the magnetic field lines (white solid lines) around the X-line. The strong electron velocity seen near the center of the simulation area indicates that electrons are accelerated by E_y and perform the meandering motions. Thus this region is mostly interpreted as the electron diffusion region. As the curvature of the magnetic field lines decreases in the electron inflow region, the electron meandering region so the electron diffusion region tends to extend along the x direction. This is also evident in Figure 3.7, which describes time evolutions of (a) the length l , (b) the width δ , and (c) the aspect ratio δ/l of the electron diffusion region. The length l and the width δ of the electron diffusion region are properly determined from the simulation results at a give time. The electron diffusion region should be the region where the dissipation process are mainly supported by the electron dynamics, that is, the region where electrons are accelerated by the inductive electric field E_y and experience the meandering/Speiser motions (Speiser, 1965). Thus the downstream edge of the electron diffusion region is determined by the location

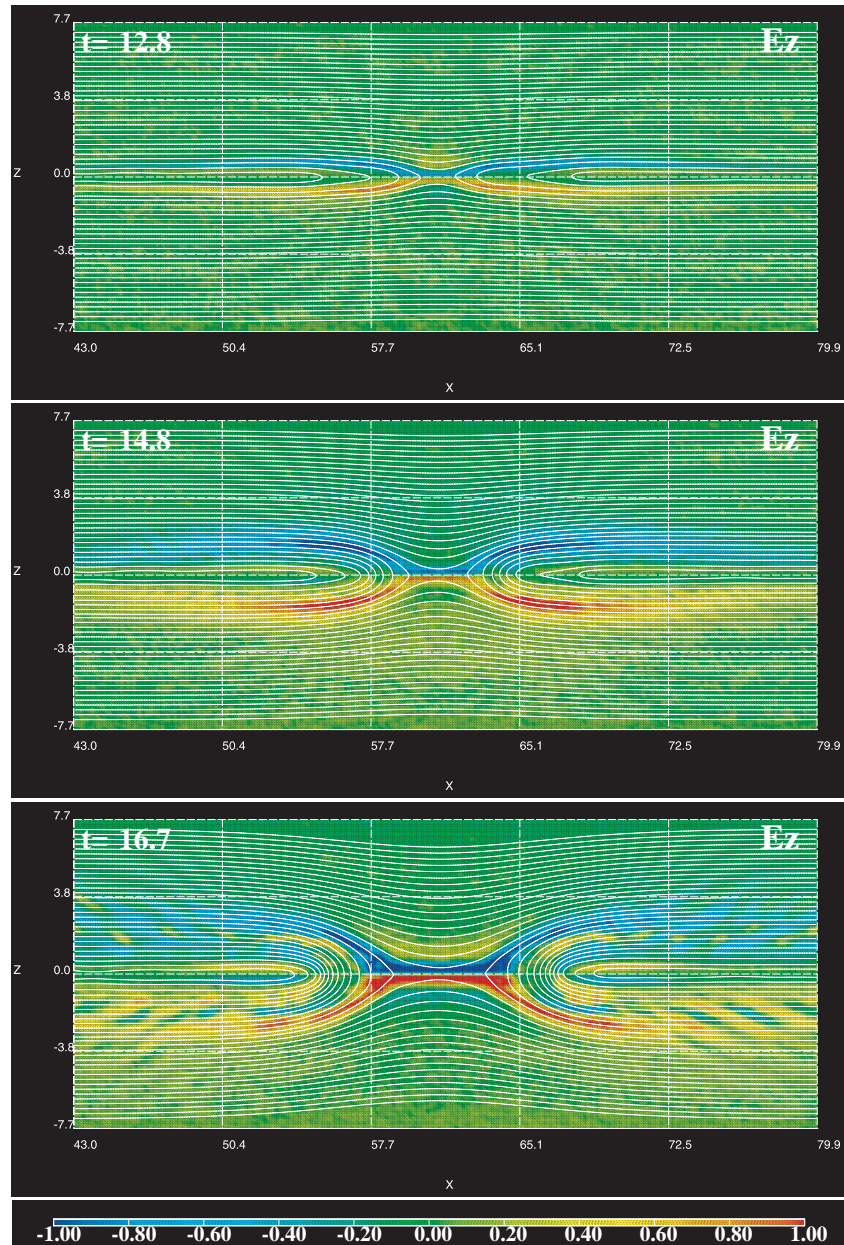


Figure 3.3: Snapshots of the electric field along the z direction at $t\omega_{ci} = 12.8$, 14.8, and 16.7. Magnetic field lines (white solid lines) are superposed on each panel.

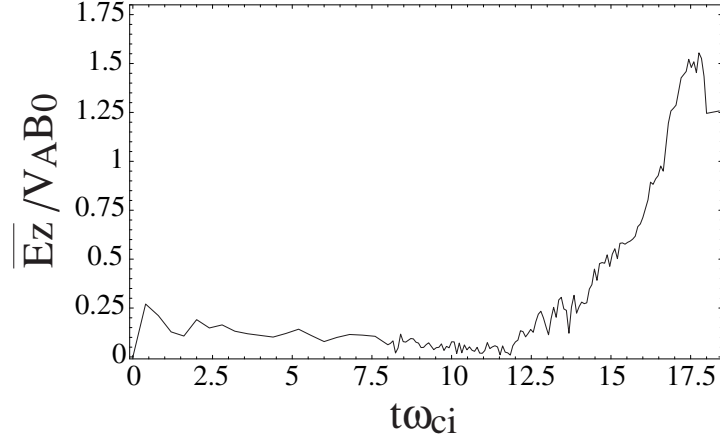


Figure 3.4: Time evolution of the electric field directing toward the neutral sheet $\overline{E_z} = -z/|z| E_z$, averaged over the electron inflow region ($l_x/2 - 0.2\lambda_{i0} \leq x \leq l_x/2 + 0.2\lambda_{i0}$, $0.25\lambda_{i0} \leq |z| \leq 0.5\lambda_{i0}$).

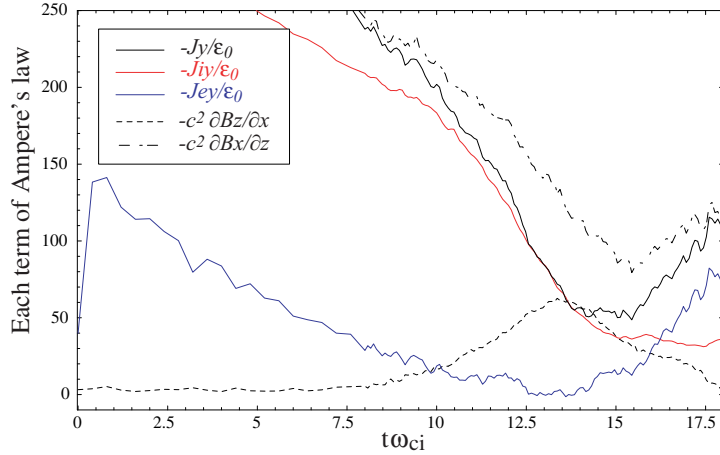


Figure 3.5: Time history of each term in the right-hand side of Ampère's law ($\partial E_y/\partial t = -J_y/\epsilon + c^2(\partial B_x/\partial z - \partial B_z/\partial x)$) averaged over the electron inflow region. The black solid line denotes the contribution of the current density, which is calculated by summing up the ion and electron current densities (red and blue solid lines, respectively). The dashed and dashed-dotted lines represent the contribution from the rotation of the magnetic field.

where the electron outflow velocity along the x axis reaches a peak value. Outside the edge, electrons are decelerated and the electron flow energy is partly converted to its thermal energy. On the other hand, the upstream edge of the electron diffusion region is determined by the turning point of the electron meandering motions. The amplitude of the electron meandering orbit is given by $\delta_m = \lambda_g(\delta_m)$, where $\lambda_g(z) = v_{th}/\omega_c$ is the local Larmor radius of electrons, $v_{th} = \sqrt{2T_e/m_e}$ is the electron thermal velocity, and $\omega_c = -eB_x/m_e$ is the electron cyclotron frequency. The width δ is defined by $\delta = \delta_m^+ + (-\delta_m^-)$, where δ_m^\pm denotes the location of the upstream edge in the $\pm z$ region. The length l of the electron diffusion region increases as time goes on after $t\omega_{ci} \approx 13.5$ (Figure 3.7a) when the curvature of the magnetic field lines reaches the peak. Since the width δ is mostly constant in time (Figure 3.7b), the aspect ratio δ/l decreases after $t\omega_{ci} \approx 13.5$, especially after $t\omega_{ci} \approx 15$, so that a long and narrow diffusion region is formed (Figure 3.7c).

In Figure 3.8, a schematic field structure around the electron diffusion region is described with the polarization electric field E_z and the out-of-plane current density J_y . The electric field directing toward the neutral sheet is significant in the shadowed regions. The out-of-plane current density J_y in the shadowed region is enhanced in the manner that the polarization electric field E_z forces the inflow electrons to perform the $\mathbf{E} \times \mathbf{B}$ drift to the out-of-plane direction and enhances the out-of-plane electron current density. Since the out-of-plane current density is almost uniform along the upstream edge of the electron diffusion region, the magnetic field B_z does not appear near the X-line. Thus the magnetic field lines in the electron inflow region should be parallel to the upstream edge, so that the curvature of the magnetic field lines is reduced in association with the enhancement of J_y in the electron inflow region. On the other hand, near the downstream edge of the shadowed region, J_y has a gradient along the x direction, which gives rise to the magnetic field fluctuation δB_z (dashed arrows in Figure 3.8) and also reduces the curvature of the magnetic field lines. As a result, the magnetic field lines in the electron inflow region tend to be parallel to the x axis, leading to the extension of the electron meandering region so the electron diffusion region along the x direction.

3.3.3 Impact on the Reconnection Rate

We consider here how the structure change of the electron diffusion region affects the reconnection rate, that is, the electric field along the X-line. Figure 3.9 shows the flow velocity of electrons along the z direction at $x = l_x/2$. This profile is useful to understand the electron behavior around the X-line, when the intense polarization electric field is imposed. The dashed line expresses the $\mathbf{E} \times \mathbf{B}$ drift velocity in the z

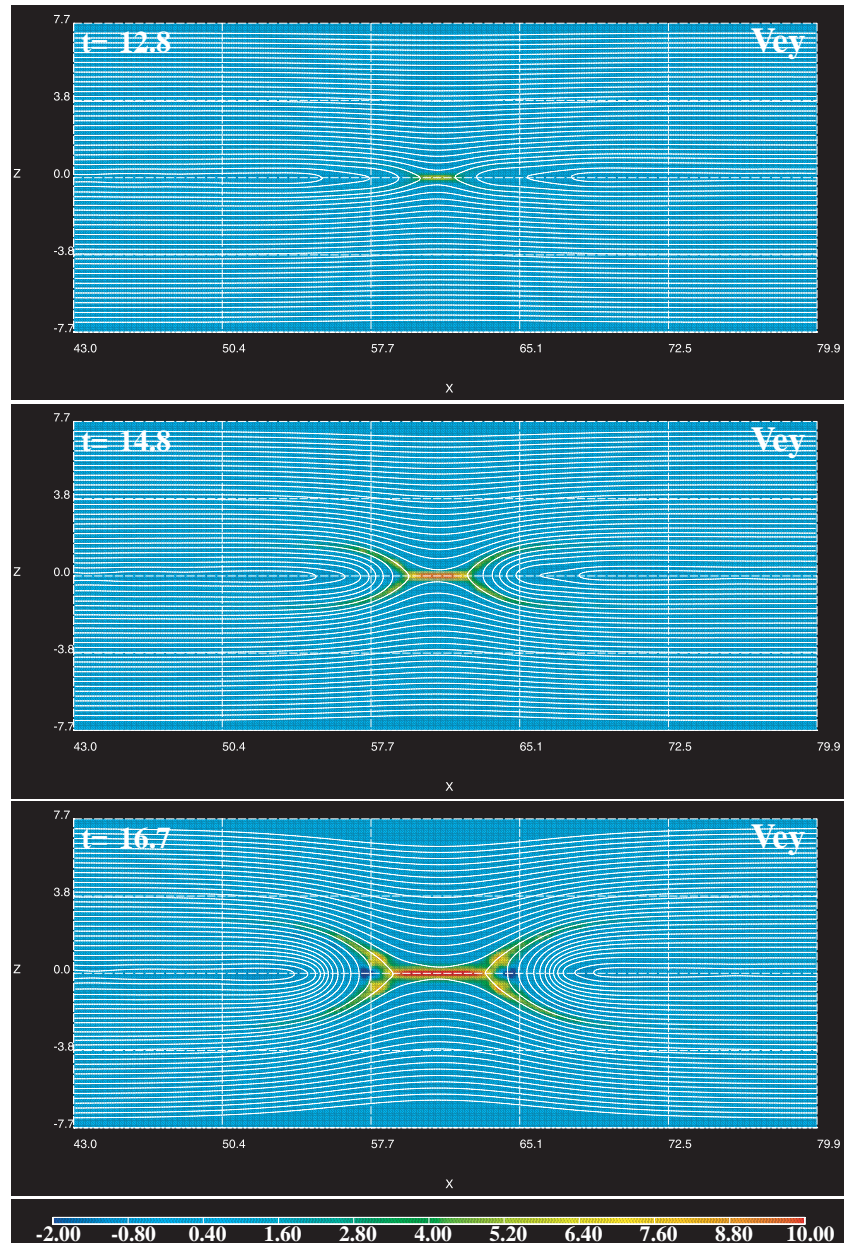


Figure 3.6: Snapshots of the out-of-plane electron flow velocity at $t\omega_{ci} = 12.8$, 14.8, and 16.7. Magnetic field lines (white solid lines) are superposed on each panel.

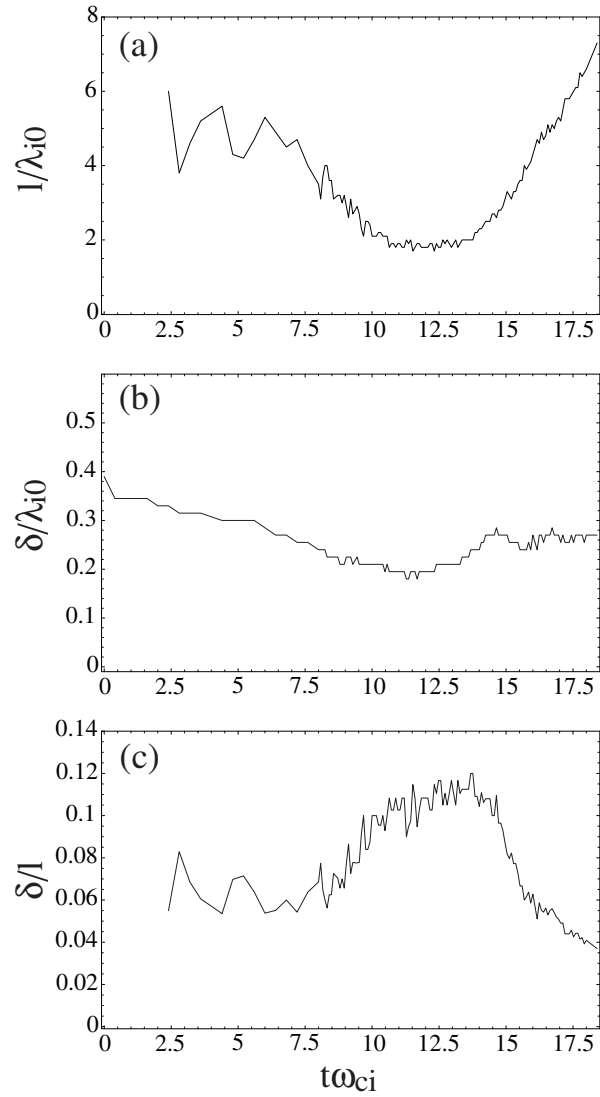


Figure 3.7: Time evolutions of (a) the length, (b) the width, and (c) the aspect ratio of the electron diffusion region, respectively.

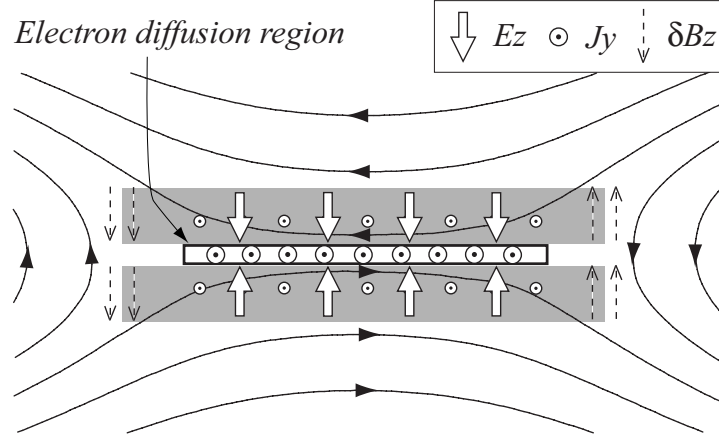


Figure 3.8: Schematic field structure including the polarization electric field E_z and out-of-plane current around the electron diffusion region. The electric field directing toward the neutral sheet is significant in the shaded regions. The out-of-plane currents in the shaded regions produce the magnetic field δB_z (dashed arrows) at the edges, which reduces the curvature of the field lines in the electron inflow region and extends the electron diffusion region along the x axis.

direction, that is, $-E_y/B_x$. The $\mathbf{E} \times \mathbf{B}$ drift velocity diverges from the electron flow velocity at $z \approx \pm 0.7\lambda_{i0}$, thereby the frozen-in condition for electrons breaks down in the region between $z \approx \pm 0.7\lambda_{i0}$. However, the upstream edges of the electron diffusion region where meandering electrons turn back to the neutral sheet is located at $z \approx \pm 0.15\lambda_{i0}$ in our definition. Actually, the strong polarization electric field imposed inside the ion-scale diffusion region makes the inertial term in the generalized Ohm's law (3.1) considerably large and suppresses the electron inflow velocity. In this case, the generalized Ohm's law (3.1) can be expressed in the form

$$E_y + V_{ez}B_x \simeq -\frac{m_e}{e} V_{ez} \frac{\partial V_{ey}}{\partial z}, \quad (3.3)$$

where $V_{ey} \simeq E_z/B_x$ is a good approximation. Thus we can obtain the electron inflow velocity

$$V_{ez} \simeq -\frac{1}{1 + \omega_{ce}^{-1} \partial V_{ey} / \partial z} \frac{E_y}{B_x}, \quad (3.4)$$

where ω_{ce} is the local electron cyclotron frequency. We call this velocity the “modified $\mathbf{E} \times \mathbf{B}$ drift velocity”. This profile is plotted by the dotted line in Figure 3.9. The modified $\mathbf{E} \times \mathbf{B}$ drift velocity diverges from the electron inflow velocity at $z \approx \pm 0.15\lambda_{i0}$, which are consistent with the upstream edges of the electron diffusion region.

Assuming that the inflow electrons along the z direction are mostly accelerated toward the x direction by the magnetic tension in the electron diffusion region, we can obtain

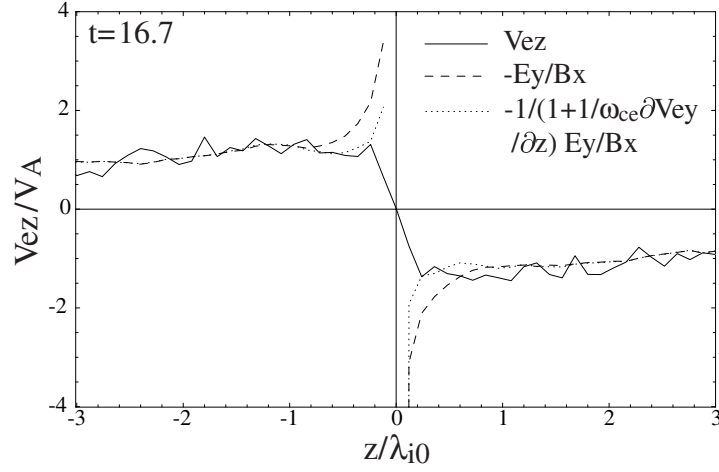


Figure 3.9: Flow velocity of electrons (solid line) along the z direction at $x = l_x/2$ and $t\omega_{ci} = 16.7$. Dashed line denotes the $\mathbf{E} \times \mathbf{B}$ drift velocity defined by $-E_y/B_x$, and dotted line is a velocity described by $-1/(1 + 1/\omega_{ce}\partial V_{ey}/\partial z) E_y/B_x$, which expresses the “modified $\mathbf{E} \times \mathbf{B}$ drift velocity” due to a large E_z .

the approximation

$$-m_e n_{e1} V_{e1} V_{e2} \simeq \frac{B_1 B_2}{\mu_0}, \quad (3.5)$$

where n_{ej} , V_{ej} , and B_j are, respectively, the electron density, velocity, and magnetic field in the location denoted by j ($j = 1$ and 2 represent the upstream and downstream edges of the electron diffusion region, respectively), that is, $V_{e1} = V_{ez}(x = l_x/2, z = \delta_m^+)$, $V_{e2} = V_{ex}(x = l^+, z = 0)$, $B_1 = B_x(x = l_x/2, z = \delta_m^+)$, $B_2 = B_z(x = l^+, z = 0)$, and l^+ is the location of the right-hand-side edge of the electron diffusion region. The out-of-plane electric field E_y is assumed to be spatially uniform around the electron diffusion region, so that

$$E_y \simeq -V'_{e1} B'_1 \simeq -V_{e1} B_1 - \frac{m_e}{e} V_{e1} \left(\frac{\partial V_{ey}}{\partial z} \right)_1 \simeq V_{e2} B_2, \quad (3.6)$$

where the prime denotes the location at which the electron inflow velocity diverges from the $\mathbf{E} \times \mathbf{B}$ drift velocity ($-E_y/B_x$), that is, $V'_{e1} = V_{ez}(x = l_x/2, z = 0.7\lambda_{i0})$, and $B'_1 = B_x(x = l_x/2, z = 0.7\lambda_{i0})$ at $t\omega_{ci} = 16.7$, for example. We further assume $V'_{e1} \simeq V_{e1}$, which implies for the incompressible fluid that all the electrons entering the region where the frozen-in condition breaks down reach the electron diffusion region defined in the

present study. From (3.5) and (3.6) using $l|V_{e1}| \simeq \delta|V_{e2}|$ for continuity, one can derive

$$V_{e2} \simeq -\sqrt{\frac{B'_1}{B_1}} V_{Ae}, \quad (3.7)$$

$$E_y \simeq -\frac{\delta}{l} \left[1 + \frac{1}{\omega_{ce,1}} \left(\frac{\partial V_{ey}}{\partial z} \right)_1 \right]^{3/2} B_1 V_{Ae}, \quad (3.8)$$

where $V_{Ae} = B_1/\sqrt{\mu_0 n_{e1} m_e}$ is called the electron Alfvén velocity. Since $B'_1/B_1 \gtrsim 1$, it is found that the electron outflow velocity can exceed the electron Alfvén velocity defined at the upstream edge of the electron diffusion region. The theoretical prediction of the out-of-plane electric field using (3.8) is plotted as a function of time in Figure 3.10 (dashed line), superposed on the direct measurement from the simulation results (solid line). This theoretical prediction is calculated from the upstream parameters (n_{e1} , B_1 , and $(\partial V_{ey}/\partial z)_1$) and the size of the electron diffusion region (δ and l) determined by the simulation results at each given time. It increases as time goes on until it reaches a peak at $t\omega_{ci} \approx 15$ and then starts to drop associated with the reduction of the aspect ratio (δ/l), that is, with the extension of the electron diffusion region. This profile is consistent with the simulation results (solid line). The damping rate of E_y after $t\omega_{ci} \approx 15$ is slightly different between the simulation results and the theoretical prediction. We think that this is caused by the underestimation of δ . In our model, we assume that all the inflow electrons are accelerated toward the x direction only in the electron diffusion region defined in the present study. However the polarization electric field E_z directing to the neutral sheet forces the inflow electrons toward the out-of-plane direction, even when they reside outside the electron diffusion region. Thus the acceleration region should be wider along the z direction than the electron meandering region, though it is difficult to correctly determine the effective value of δ .

3.3.4 Comparison With the Case of $m_i/m_e = 1$

In order to emphasize the role of the polarization electric field caused by the ion meandering motions around the X-line, we compare the results discussed in the previous sections with those obtained from the simulations under $m_i/m_e = 1$, in which the decoupling between ions and electrons does not arise, so that the polarization electric field is eliminated. At the same time, we check the effects of the conducting wall located at the boundary of the simulation area in the z direction by performing same simulations in larger system in the z direction. In the runs with $m_i/m_e = 1$, the temperature ratio in the initial plasma sheet ($T_{i,ps}/T_{e,ps}$) is also set as unity in order to avoid the electrostatic field arising from the difference in Larmor radius between ions and electrons. The system

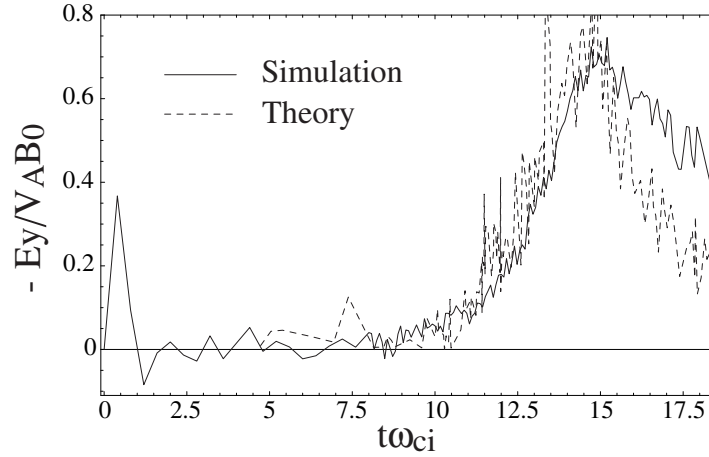


Figure 3.10: Comparison of the time evolutions of the out-of-plane electric field. The solid line denotes the direct measurement of the simulation results at the center of the simulation area. The dashed line is the theoretical prediction calculated from the upstream parameters (n_{e1} , B_1 , and $(\partial V_{ey}/\partial z)_1$) and the size of the electron diffusion region (δ and l) determined by the simulation results.

parameters in the case of $m_i/m_e = 1$ are $\Delta_{LB} = 0.96\lambda_{i0}$, $\Delta_{LD} = 0.12\lambda_{i0}$, $\Delta t\omega_{ci} = 0.01$, and $c/V_A = 6.0$. The other conditions are the same as the case of $m_i/m_e = 100$. We examine several system sizes: $l_x \times l_z = 122.9\lambda_{i0} \times 30.7\lambda_{i0}$, and $122.9\lambda_{i0} \times 61.4\lambda_{i0}$ for the $m_i/m_e = 100$ runs, and $l_x \times l_z = 122.9\lambda_{i0} \times 30.7\lambda_{i0}$, $122.9\lambda_{i0} \times 61.4\lambda_{i0}$, and $122.9\lambda_{i0} \times 122.9\lambda_{i0}$ for the $m_i/m_e = 1$ runs.

The time evolution of the out-of-plane electric field at the center of the simulation area (the reconnection rate) is shown in Figure 3.11 for each run. In the case of $m_i/m_e = 1$, we find that a steady-state reconnection is achieved in larger system, although the reconnection rate in the smaller system ($l_x \times l_z = 122.9\lambda_{i0} \times 30.7\lambda_{i0}$) tends to drop due to the effects of the conducting wall boundary. On the other hand, in the case of $m_i/m_e = 100$, the time evolution of the reconnection rate is independent of the system size, rising until $t\omega_{ci} \approx 15$ and then falling down associated with the extension of the electron diffusion region. These results demonstrate the importance of the polarization electric field E_z in suppressing the reconnection processes. Another important point is that the asymptotic reconnection rate in the $m_i/m_e = 1$ runs ($|E_y| \sim 0.45V_A B_0 = 0.09V_{A0} B_0$) is large enough to explain fast dissipative events, even though the Hall effects are not included. Therefore it is suggested that the Hall effects should not be necessarily required for fast reconnection. This is well consistent with the results of Karimabadi et al. (2004)

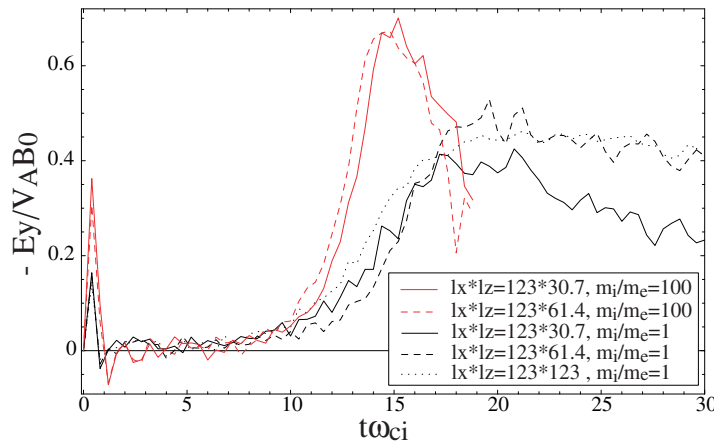


Figure 3.11: Comparison of the time evolutions of the out-of-plane electric field at the center of the simulation area (the reconnection rate). Red lines denote the runs for $m_i/m_e = 100$, and black lines the runs for $m_i/m_e = 1$. Two system sizes are examined under each mass ratio: $l_x \times l_z = 122.9\lambda_{i0} \times 30.7\lambda_{i0}$ (solid lines), and $122.9\lambda_{i0} \times 61.4\lambda_{i0}$ (dashed lines). Larger system size with $l_x \times l_z = 122.9\lambda_{i0} \times 122.9\lambda_{i0}$ is also employed under $m_i/m_e = 1$ (shown by black dotted line).

3.4 Summary and Discussion

In this paper, we have investigated long time evolutions of the electron diffusion region embedded in the ion-scale diffusion region and the resulting reconnection rate associated with magnetic reconnection in a fully kinetic and large system. We performed 2-1/2 dimensional full particle simulations with the adaptive mesh refinement (AMR) technique and the particle splitting algorithm (Fujimoto and Machida, 2005b). The adoption of these techniques to the conventional particle-in-cell (PIC) code enables us to perform effectively high-resolution simulations including kinetic processes of magnetic reconnection. Previous reconnection studies using full particle simulations in the periodic system (Shay et al., 2001; Hesse et al., 2001; Pritchett, 2001; Kuznetsova et al., 2001) achieved fast reconnection, but the system did not reach steady state and the reconnection rate decreased after it reached a peak value. This is because the compressional effects in the magnetic islands affect the reconnection processes in small periodic systems. The full particle code with the AMR and particle splitting employed in the present study allows us to take a large system, in which the effects of the periodic boundary hardly affect the reconnection processes within the present simulation time.

We find that the reconnection rate increases associated with magnetic reconnection and reaches a peak value large enough for fast reconnection, but then it decreases as time goes on, even though the periodicity of the system is negligible. The key process

responsible for slowing magnetic reconnection is the extension of the electron diffusion region associated with the evolution of the strong polarization electric field E_z imposed in the electron inflow region. The polarization electric field directing toward the neutral sheet is caused by the inertia difference between ions and electrons, and enhanced by the meandering motions of the background ions. Because the hot ions initially loaded in the Harris-type current sheet have a large velocity in the out-of-plane direction, they can easily escape from the diffusion region due to the Lorentz force before their meandering motions become dominant. Thus their impact on the strong E_z is small. The polarization electric field E_z forces the inflow electrons to move toward the out-of-plane direction by the $\mathbf{E} \times \mathbf{B}$ drift and enhances the out-of-plane current density J_y in the electron inflow region. The role of J_y is to reduce the curvature of the magnetic field lines so that they are mostly parallel to the x direction near the X-line, in such a way that J_y becomes uniform along the upstream edge of the electron diffusion region. As a result, the electron meandering region so the electron diffusion region extends along the x direction.

We performed a Sweet-Parker-like analysis around the electron diffusion region, taking into account the breakdown of the electron frozen-in condition in the electron inflow region, and demonstrate that the extension of the electron diffusion region can suppress the reconnection rate. In order to emphasize the role of the polarization electric field and the Hall effects, we compare the simulation runs with $m_i/m_e = 1$ and $m_i/m_e = 100$. It is found that (1) a steady-state reconnection is achieved in the $m_i/m_e = 1$ cases where the polarization electric field does not appear, different from the $m_i/m_e = 100$ cases, (2) a large reconnection rate with $|E_y| \sim 0.09V_{A0}B_0$ is obtained in the $m_i/m_e = 1$ runs, even though they do not include the Hall effects, so that the Hall effects are not necessarily required for fast reconnection.

The polarization electric field E_z caused by the ion meandering motions has been seen in previous studies within large systems using hybrid simulations (Shay et al, 1999; Arzner and Scholer, 2001). However, their systems achieved a quasi-steady reconnection, different from the present results. This inconsistency is possibly attributed to the absence of the electron meandering effects in the previous simulations. The damping of the reconnection rate results from the extension of the electron diffusion region in which electrons carry out the meandering motions. The electron meandering effects should be incorporated into the term arising from the nongyrotropic electron pressure of the generalized Ohm's law (the second term in the right-hand side of (3.1)) (Cai and Lee, 1997; Hesse and Winske, 1998; Kuznetsova et al., 1998; Hesse et al., 1999; Swisdak et al., 2005). However, both of the previous studies did not include this term.

A long time evolution of the diffusion region using full particle simulations has been

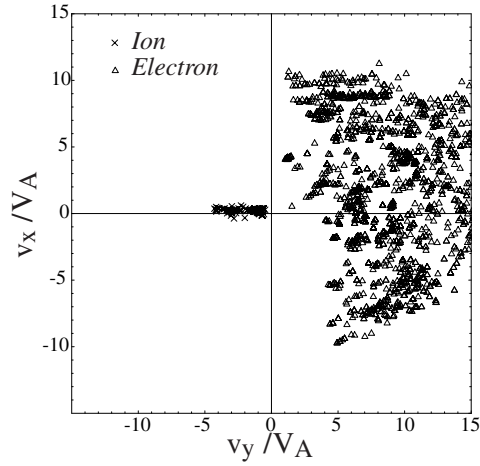


Figure 3.12: Distributions in the v_x - v_y velocity space of ions (crosses) and electrons (open triangles) at the center of the simulation area at $t\omega_{ci} = 14.8$.

investigated by Pei et al. (2001) under an open system. Their system also reached a steady-state reconnection and the structure was mostly unchanged during the simulation time. Magnetic reconnection in their system is driven by an external electric field, supplying an external plasma into the system. The reconnection rate in such a driven system is mainly controlled by the external driving electric field (Sato and Hayashi, 1979; Pei et al., 2001). Thus the size of the diffusion region should be determined in the manner that the output of the plasma and magnetic field flux from the system becomes consistent with the input from the external region. Thus the reconnection processes in the driven system are essentially different from those in the spontaneous system as employed in the present study, in which there is no energy input from the external region.

The question that remains is what can support fast reconnection in actual space plasma after the reconnection rate reaches the peak. In fact, the peak value of the reconnection rate obtained in the present runs is $\sim 0.7V_A B_0$. If we take $B_0 \sim 10$ nT and $n_{ps} \sim 0.5$ cm $^{-3}$, we can calculate $|E_y| \sim 2.2$ mV/m, which is not unrealistic compared with observational results (Asano et al., 2004). However, in our model, the reconnection rate is expected to continue decreasing after the meandering motions due to the background cold ions have been dominant around the X-line. Thus it is supposed that other mechanisms that are not included in the model might play an important role in enhancing the reconnection rate. In the two-dimensional system employed in the present study, plasma instabilities excited along the y direction are suppressed in principle. Actually, since electrons in the electron diffusion region can be strongly accelerated toward the y direction beyond the electron Alfvén velocity defined in the upstream region, a

large velocity difference between ions and electrons is expected to arise. In Figure 3.12, distribution in $v_x - v_y$ space at the center of the simulation area and $t\omega_{ci} = 14.8$ are shown for ions (crosses) and electrons (open triangles). The velocity difference between ions and electrons along the y direction is beyond the thermal spread of the electron distribution function. In such a condition, the Buneman-type instability can be excited along the y direction. Indeed, such an instability and its nonlinear structure have been demonstrated in the three-dimensional system with a strong guide field (Drake et al., 2003), and can give rise to the anomalous resistivity, so that the reconnection rate ($|E_y|$) is enhanced. In order to investigate the role of the Buneman-type instability in the electron diffusion region, it is necessary to perform a large-scale kinetic simulation in the three-dimensional system.

CHAPTER 4

A Generation Mechanism of Electrostatic Waves and Subsequent Electron Heating in the Plasma Sheet-Lobe Boundary Region During Magnetic Reconnection

4.1 Introduction

Magnetic reconnection is widely believed to play an important role in the magnetospheric substorm and solar flares as a fast conversion process of the magnetic energy to kinetic and thermal energy of ions and electrons. In fact, electron heating and acceleration arising during a number of phenomena in space are recognized as signatures of magnetic reconnection. For example, in the Earth magnetotail, bursts of high energy electrons have been reported in association with topological change of the near-Earth field line, so that they have been attributed to magnetic reconnection (Terasawa and Nishida, 1976; Baker and Stone, 1976). In solar flares, x-ray observations indicate that a large part of the total energy is released in energetic electrons accelerated via magnetic reconnection (Lin and Hudson, 1976; Lin et al., 2003). Plasma heating and acceleration processes in association with magnetic reconnection have been discussed over the last decades. However, our understanding on the energization mechanisms of electrons still remains poor.

It is well known that non-Maxwellian electrons selectively heated parallel to the ambient magnetic field, having an velocity distribution of the flat-topped form, have been often observed in the plasma sheet-lobe boundary region located between the magnetotail lobe and the plasma sheet in association with magnetic reconnection (Saito et al.,

1995; Shinohara et al., 1998; Hoshino et al., 2001a). One of the candidates responsible for the anomalous heating is the acceleration in the slow-mode shocks (Schwartz et al., 1987; Saito et al., 1995), which can explain a fast energy conversion from the stored magnetic energy to the plasma kinetic energy (Petschek, 1964). However, Saito et al. (1995) have demonstrated that the plasma sheet-lobe boundaries do not necessarily satisfy the slow mode jump condition even if the electron flat-topped distributions are observed in the downstream region. This indicates that the conventional slow-mode shocks might not play a significant role in the electron heating in the Earth magnetotail. Shinohara et al. (1998) also observed the flat-topped electrons associated with an electromagnetic turbulence near the X-type neutral line. They concluded that the electromagnetic turbulence results from the lower hybrid drift instability (LHDI) and suggested that the electron heating should be closely related with the LHDI. Hoshino et al. (2001a), on the other hand, discussed the physical processes producing the flat-topped electrons by comparing the satellite observations and the electromagnetic particle-in-cell (PIC) simulations. They suggested that the Buneman instability (Buneman, 1958) excited due to the velocity difference between the stationary ions and the beam electrons accelerated near the X-type neutral line and/or the electron bump-on-tail instability (Omura et al., 1996) arising between the weak beam electrons and the stationary hot electrons should be responsible for the electron scattering in the plasma sheet-lobe boundary region. However, they do not specify the nature of the instabilities in detail possibly because the simulation area with the periodic boundaries is too small to describe the nonlinear feature of such instabilities. In fact, a small system with the periodic boundaries can affect nonlinear wave-particle interactions in the boundary region via high energy particle passing across the boundaries.

Wave activities in the plasma sheet-lobe boundary region of the Earth magnetotail have been extensively studied by means of the Geotail satellite observations (e.g., Matsumoto et al., 1994; Kojima et al., 1994). Their main finding is that most of the broadband noise in the wave spectrum obtained in the boundary region are not continuous noise but are composed of a series of solitary pulses called the electrostatic solitary waves (ESW). The generation mechanism of the ESW observed in the magnetotail is explained by the nonlinear mode of the electron two-stream instabilities (e.g., Omura et al., 1996) including bump-on-tail instability or the Buneman instability as reported by Drake et al. (2003). Therefore the electron beam flowing relatively to the background electrons or ions is inevitable in order to generate the ESW. Magnetic reconnection can be one of the strong candidates for the process producing such an electron beam (Kojima et al., 1994). Actually, the satellite observations on the dayside magnetopause boundary

reported by Matsumoto et al. (2003) suggest that magnetic reconnection should be related to the ESW activities. Recently, Cattell et al. (2005) have observed large-amplitude solitary waves and associated electron holes in the plasma sheet-lobe boundary region of the magnetotail when near-Earth reconnection has occurred. Their conclusion is that the detected ESW result from the Buneman instability, and not from the electron two-stream instabilities. The observations by Matsumoto et al. (2003) and Cattell et al. (2005) indicate that the electrostatic wave activities may play an important role in the electron energization in the plasma sheet-lobe boundary region during magnetic reconnection.

In this paper, we study electron heating process in detail expected in the boundary between the magnetotail lobe and the plasma sheet associated with magnetic reconnection by performing large-scale PIC simulations using the adaptive mesh refinement (AMR) and particle splitting techniques (Fujimoto and Machida, 2005b). We show that intense electrostatic waves are excited in the plasma sheet-lobe boundary region by the electron two-stream instability between the cold electrons loaded in the lobe and the strong beam electrons with high temperature. The electrostatic waves propagating along the ambient magnetic field scatter and heat the electrons along the field line, and form the flat-topped electron distribution function. We also demonstrate that the ESW are generated as a result of the nonlinear evolution of the electron two-stream instability during magnetic reconnection, even when a strong guide field as imposed in Drake et al. (2003) is absent.

4.2 Simulation Model

The present study employs a 2-1/2 dimensional electromagnetic PIC code with the AMR technique and the particle splitting algorithm, which has been described by Fujimoto and Machida (Fujimoto and Machida, 2005a,b). The AMR technique subdivides and removes computing cells dynamically in accordance with a refinement criterion and quite effective to achieve high-resolution simulations of phenomena that locally include micro-scale processes. In our code, the spatial resolution is increased by introducing finer cells hierarchically onto the uniform base cells that cover the entire simulation area. If a base cell is refined, four child cells that have half the size of the base cell are generated. These child cells can be also refined in turn and finer cells are produced, and so on. One of the main problem in developing the electromagnetic PIC codes using the AMR technique is the decrease in the number of particles per cell in the refined region (Fujimoto and Machida, 2005a). In order to solve this problem, we subdivide particles residing in the subdivided cells and control the number of particles per cell. We employ the particle splitting algorithm developed by Lapenta (2002), in which the moments on

each grid (the charge and current densities), the total charge, mass, momentum, and energy of particles, and the distribution function of particles are retained between before and after the particle splitting. Each cell is needed to have information of the parent, child, and neighboring cells, and the particles residing in the cell. The communication between cells or between a cell and the particles in the cell is supported by a set of pointers, constructing the fully threaded tree structure (Khokhlov, 1998). A refinement level L in the hierarchical cell structure is defined by using the cell size of the level (Δ_L) as $L \equiv \log_2(l_z/\Delta_L)$, where l_z is the vertical size of the two-dimensional simulation area. We use only cells with integer level. More detailed description on our code is shown in Fujimoto and Machida (2005b).

The refinement condition in the current study is defined by three physical values. The first is the local electron Debye length, $\lambda_{De} = v_{th,e}/\sqrt{2}\omega_{pe}$, which is required to avoid a numerical heating of local plasma, where $v_{th,e} = \sqrt{2T_e/m_e}$ is the electron thermal velocity (T_e and m_e are the temperature and mass of electrons, respectively), and ω_{pe} is the electron plasma frequency. We use the initial value of $v_{th,e}$ for calculation of λ_{De} , because electrons are expected to be heated in the region where the electron dynamics is important, that is, we use the minimum value of λ_{De} . The second is the out-of-plane electron flow velocity (V_{ey}), because the inertial term in the generalized Ohm's law becomes dominant in the region where the electron flow is strong, so that the dissipation of the magnetic field becomes strong and higher resolution is required. The third is the in-plane electron current density ($j_{exz} = \sqrt{j_{ex}^2 + j_{ez}^2}$), which is required because intense currents can excite microinstabilities so that electron-scale waves are expected to arise. In each time step, if λ_{De} , V_{ey} , and j_{exz} calculated at the center of a cell satisfy the condition, $\Delta_L > 2.0\lambda_{De}$ or $V_{ey} > 2.0V_A$ or $j_{exz} > 0.5en_{ps}V_A$, the cell is subdivided and four child cells are produced, otherwise, the child cells are removed if any. Here, V_A is the Alfvén velocity defined by the initial lobe field (B_0) and plasma sheet density (n_{ps}), and e is the electron charge. The particle splitting is performed only for the background particles whose distribution is described later. The particle coalescence algorithm is also implemented for the background particles once in a few hundred time steps. However, in both the particle splitting and coalescence algorithms, we never choose particles in the most refined (finest) cells to avoid numerical errors in physically important regions. In the present study, the hierarchical cell structure consists of four cell layers.

The initial magnetic field configuration is given as $B_x(z) = -B_0 \tanh(z/\lambda)$, and the corresponding density is $n(z) = n_{ps} \operatorname{sech}^2(z/\lambda)$, where λ is the half width of the initial plasma sheet and set as $\lambda = 0.5\lambda_{i0}$ (λ_{i0} is the ion inertial length defined by n_{ps}). In

addition to the equilibrium, a small perturbation is superposed in the form,

$$\begin{aligned} B_{xp}(x, z) &= 2a_0/\lambda \operatorname{sech}^2((x - l_x/2)/L') \operatorname{sech}^2(z/\lambda) \tanh(z/\lambda) \\ B_{zp}(x, z) &= -2a_0/L' \operatorname{sech}^2((x - l_x/2)/L') \operatorname{sech}^2(z/\lambda) \tanh((x - l_x/2)/L'), \end{aligned} \quad (4.1)$$

where, l_x is the horizontal length of the simulation area, and a_0 and L' provide the amplitude and horizontal size of the perturbation, respectively. In the present study, $a_0 = 0.15B_0\lambda_{i0}$, $L' = 3.8\lambda_{i0}$, and $l_x \times l_z = 122.9\lambda_{i0} \times 30.7\lambda_{i0}$ are chosen. Furthermore, the background plasma is loaded as $n_b(z) = n_{b0} \tanh^2(z/\lambda)$ and $n_{b0} = 0.044n_{ps}$ in order to describe the lobe plasma in the magnetospheric tail. Although there appears a weak pressure imbalance due to this background profile, it is quickly justified without any significant modification of the current sheet structure. Once the simulation starts, the initial plasma sheet density and current profiles are quickly modified to adjust the field perturbation. As a result, a thinner current sheet is formed near the center of the simulation area, so that the tearing instability selectively develops therein. The cell size is $\Delta_{LB} = 0.12\lambda_{i0}$ for the coarsest cells and $\Delta_{LD} = 0.015\lambda_{i0}$ for the finest cells, and the time step is $\Delta t\omega_{ci} = 8.0 \times 10^{-4}$ for all particles and refined regions in order to satisfy the Courant condition on the finest cells, where ω_{ci} is the ion cyclotron frequency defined by the lobe field (B_0). The initial plasma condition is $m_i/m_e = 100$, $T_{i,ps}/T_{e,ps} = 8.0$, $T_{i,lobe}/T_{e,lobe} = 1.0$, $T_{e,lobe}/T_{e,ps} = 1.0$, and $c/V_A = 16.7$, where $T_{s,ps}$ and $T_{s,lobe}$ are the temperatures of the species s at the central plasma sheet and the magnetic lobe, respectively, and c is velocity of light. We assume the periodic boundary in the x direction and the conducting wall in the z direction.

4.3 Results

4.3.1 Parallel Electron Heating in the Plasma Sheet-Lobe Boundary Region

In order to investigate the electron heating process in the plasma sheet-lobe boundary region, we have performed large-scale kinetic simulations so that the non-realistic effects arising from the periodicity of the system, such as the compression of the magnetic field and plasma in the magnetic island and high energy particles passing across the periodic boundary are negligible in the extensive region around the X-line. A snapshot of the out-of-plane current density with magnetic field lines at $t\omega_{ci} = 15.6$ is shown in Figure 4.1a. It is clearly shown that a strong current sheet with narrow width is formed around the X-line, supporting fast reconnection resulting from an intense magnetic dissipation due to the electron inertia effects (e.g., Vasyliunas, 1975; Hesse et al., 1999). Figure

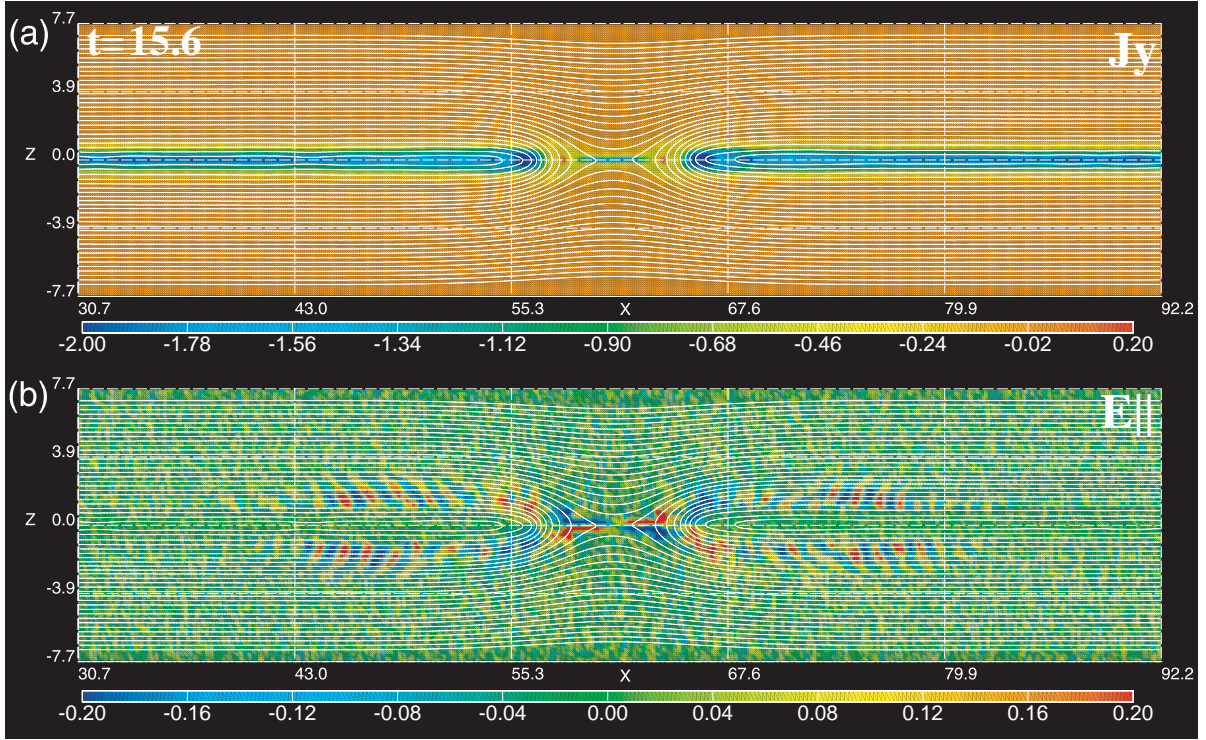


Figure 4.1: (a) Out-of-plane current density (J_y) and (b) electric field parallel to the local magnetic field (E_{\parallel}) at $t\omega_{ci} = 15.6$. The magnetic field lines (white solid lines) are superposed in each figure.

4.1b presents a contour map of the electric field parallel to the in-plane magnetic field described by the white solid lines, that is, $E_{\parallel} = \mathbf{E} \cdot \mathbf{b}$, where $\mathbf{b} = [(B_x, 0, B_z)/\sqrt{B_x^2 + B_z^2}]^T$. It is found that wave-like structures of E_{\parallel} are induced almost along the magnetic field lines around the edge of the plasma sheet, that is, in the plasma sheet-lobe boundary region. It is worth noticing that the wave-active region is inside the magnetic separatrices where the fast outflow of electrons accelerated near the X-line is expected to present. The magnification of the right-hand plane of Figure 4.1b is shown in Figure 4.2.

In order to reveal the role of the waves, we have investigated the time evolutions of the $v_{e\parallel} - x$ phase space distribution and E_{\parallel} profile along a magnetic field line passing through the wave-active region at $t\omega_{ci} = 15.6$, where $v_{e\parallel} = \mathbf{v}_e \cdot \mathbf{b}$ is the electron velocity parallel to the in-plane magnetic field. Figure 4.3 shows the snapshots of such profiles at (a) $t\omega_{ci} = 13.6$, (b) 15.6, and (c) 17.2. We choose the field line passing through $(x/\lambda_{i0}, z/\lambda_{i0}) = (84.0, -1.32)$ at each time, the trace of which is presented in Figure 4.2 by the white dashed line. The magnetic field line at $t\omega_{ci} = 13.6$ is not yet reconnected. At this time, the electrons locating along the field line are slowly pulled into the diffusion region due to E_{\parallel} induced near the X-line. Counter-streaming electrons coming from

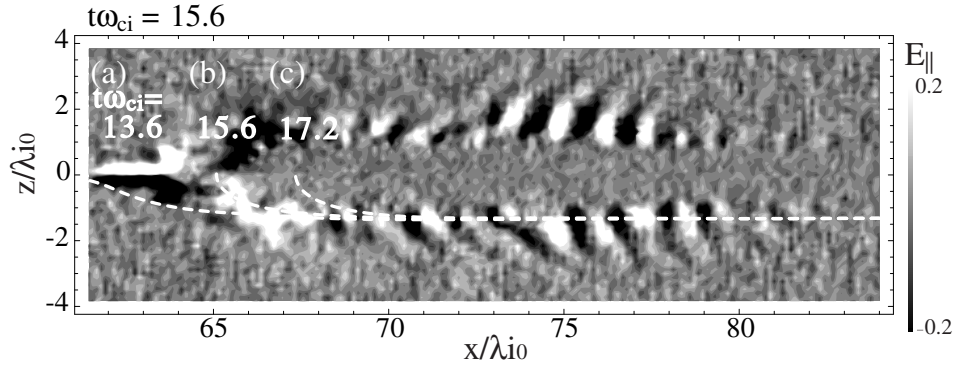


Figure 4.2: Magnification of Figure 4.1(b) for the right-hand side of the X-line. White dashed lines represent the magnetic field lines passing through $(x/\lambda_{i0}, z/\lambda_{i0}) = (84.0, -1.32)$ at (a) $t\omega_{ci} = 13.6$, (b) 15.6, and (c) 17.2.

the left-half plane of Figure 4.1b appear only near the X-line, and the wave activity is weak in most region. On the other hand, the magnetic field line has been reconnected at $t\omega_{ci} = 15.6$ and passes through the downstream region of the fast electron flow generated near the X-line. At this time, a strong electron beam flowing away from the plasma sheet appears in the extensive region along the field line and the wave activity becomes strong. It is shown that some of electrons are trapped by the electrostatic potential of the waves and form the electron holes in the $v_{e\parallel} - x$ phase space (see Figure 4.3b). At $t\omega_{ci} = 17.2$, the magnetic field line reaches further downstream region and the electrons residing along the line are found to be heated parallel to the ambient magnetic field, so that the waves are damped due to the Landau resonance with the heated electrons. The electron heating due to the waves is also evident in Figure 4.4, which shows the electron distribution function at $(x/\lambda_{i0}, z/\lambda_{i0}) = (71.8, -1.32)$ for each time presented in Figure 4.3. The electron distribution function at $t\omega_{ci} = 13.6$ consists of one component of a cold isotropic electrons with a weak bulk velocity, $V_{e\parallel} \approx -V_A$, along the magnetic field line. At $t\omega_{ci} = 15.6$, in addition to this cold component, a strong beam component with $V_{e\parallel} \approx 7V_A$ and high perpendicular temperature has arisen. Then electrons are finally heated selectively parallel to the ambient magnetic field due to the scattering by the waves and form the flat-topped distribution function.

In order to clarify the heating mechanism, it is important to estimate the heating level resulting from the electron trapping by the electrostatic potential wells along the field line. In this case, the trapping width v_t can be a good benchmark for the heating level, where v_t means the absolute value of the velocity in the rest frame of the waves, below which electrons are trapped by the electrostatic potential wells. The trapping

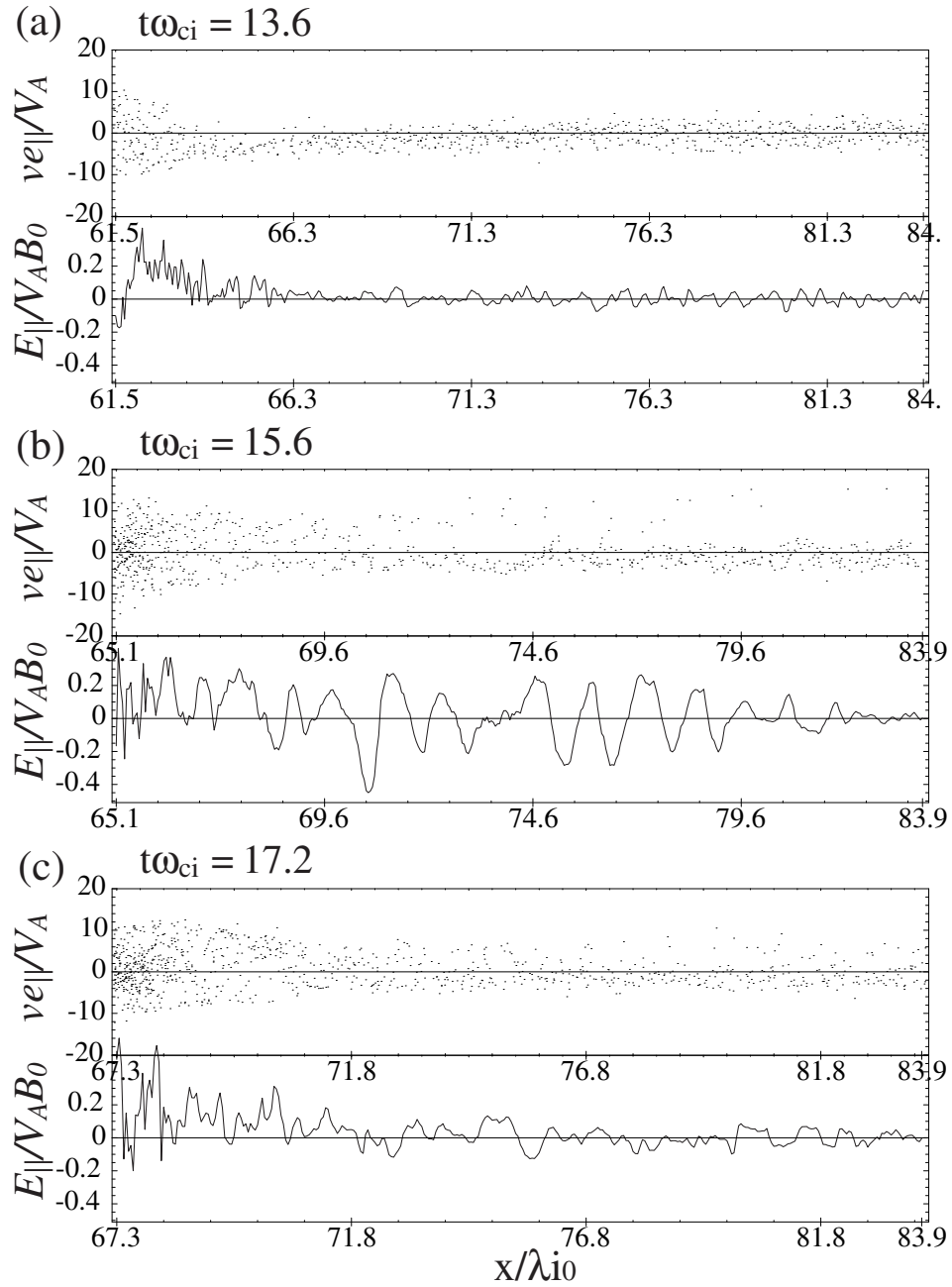


Figure 4.3: Electron velocity ($v_{e\parallel}$) and electric field (E_{\parallel}) parallel to the in-plane magnetic field are plotted along the field lines passing through $(x/\lambda_{i0}, z/\lambda_{i0}) = (84.0, -1.32)$ at (a) $t\omega_{ci} = 13.6$, (b) 15.6, and (c) 17.2, each of which is represented by the white dashed line in Figure 4.2.

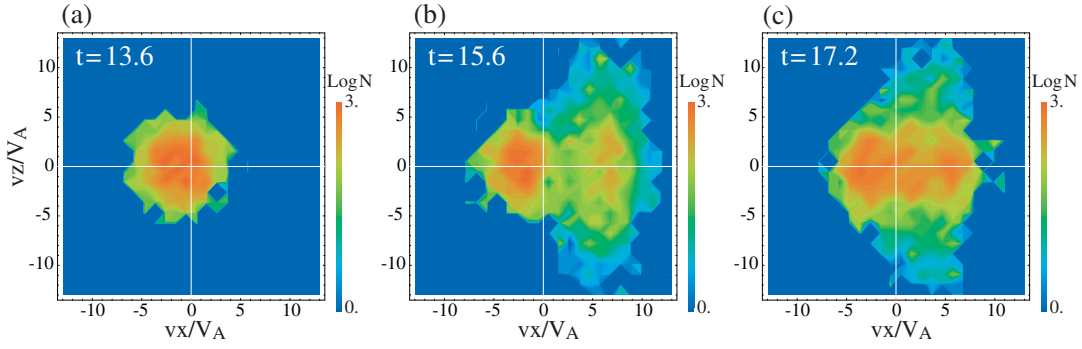


Figure 4.4: Electron distribution functions at the position $(x/\lambda_{i0}, z/\lambda_{i0}) = (71.8, -1.32)$ and the time (a) $t\omega_{ci} = 13.6$, (b) 15.6, and (c) 17.2.

width v_t is related to the amplitude of the wave potential ϕ_0 by,

$$\frac{1}{2}m_e v_t^2 \sim 2e\phi_0. \quad (4.2)$$

The potential amplitude ϕ_0 is represented as,

$$\phi_0 = \frac{E_0}{k}, \quad (4.3)$$

where we assume $E_x(x) = E_0 \sin kx$ and $E_x \simeq E_{\parallel}$ in the rest frame of the waves. Thus v_t is estimated as,

$$v_t \sim 2\sqrt{\frac{eE_0}{m_e k}} \quad (4.4)$$

In our simulations, the wave amplitude reaches $E_0 \approx 0.40V_A B_0$ and the typical wave length is $\lambda_w \approx 1.3\lambda_{i0}$ which corresponds to $k\lambda_{i0} \approx 4.8$ (see also Figure 4.7). Thus the trapping width is calculated using (4.4) as $v_t \approx 5.8V_A$, so that the shoulder width of the flat-topped electron distribution is estimated as $2v_t \approx 12V_A$, which is fairly consistent with our simulation results (see Figure 4.4c). The shoulder energy of the flat-topped electrons can be also obtained from $\mathcal{E}_{sh} \sim m_e v_t^2/2$. Taking typical parameters in the Earth magnetotail, $B_0 \sim 20$ nT and $n_{ps} \sim 0.3$ cm $^{-3}$, the shoulder energy can be calculated to be $\mathcal{E}_{sh} \sim 1$ keV, which is consistent with satellite observations (e.g., Shinohara et al., 1998).

It is also valuable to estimate the bouncing time τ_b of trapped electrons in order to know the time scale for the electron heating. We consider a single electron trapped by the sinusoidal electrostatic potential. This electron obeys the equation of motion,

$$\begin{aligned} m_e \frac{d^2 x}{dt^2} &= -eE_0 \sin kx \\ &\simeq -eE_0 kx, \end{aligned} \quad (4.5)$$

where we assume a small amplitude of the electron displacement compared to the wave length. Thus the bouncing frequency of the trapped electron is obtained as

$$\omega_b = \sqrt{\frac{ekE_0}{m_e}}, \quad (4.6)$$

so that τ_b is estimated to be

$$\tau_b \sim \omega_b^{-1} = \sqrt{\frac{m_e}{ekE_0}}. \quad (4.7)$$

Using the same parameters employed in the above discussion, we get $\tau_b \sim 0.072 \omega_{ci}^{-1}$, which indicates that the time scale for the electron heating is quite shorter than the Alfvén transit time $\tau_A \sim 1.0 \omega_{ci}^{-1}$ that is thought to govern the structure change of the current sheet associated with magnetic reconnection. Therefore such electron heating should occur in the extensive region in the plasma sheet-lobe boundary region where the intense wave activity appears. This is confirmed by Figure 4.5, which shows the profiles of the electron temperatures ($T_{e\parallel}$, $T_{e\perp}$, and T_{ey}) at $t\omega_{ci} = 17.2$ along the magnetic field line traced in Figure 4.2. The temperatures are defined by,

$$T_{ej} = \frac{m_e}{n} \int (v_{ej} - \overline{v_{ej}})^2 f(\mathbf{v}_e) d^3v, \quad (4.8)$$

where,

$$\overline{v_{ej}} = \frac{1}{n} \int v_{ej} f(\mathbf{v}_e) d^3v, \quad (4.9)$$

$$n = \int f(\mathbf{v}_e) d^3v. \quad (4.10)$$

Here, $f(\mathbf{v}_e)$ is the local distribution function of electrons, j ($=\parallel, \perp$, and y) denotes the each component, $v_{e\parallel} = \mathbf{v}_e \cdot \mathbf{b}$ with $\mathbf{b} = [(B_x, 0, B_z)/\sqrt{B_x^2 + B_z^2}]^T$, $v_{e\perp} = \mathbf{v}_e \cdot (\mathbf{b} \times \hat{\mathbf{e}}_y)$, and $v_{ey} = \mathbf{v}_e \cdot \hat{\mathbf{e}}_y$ ($\hat{\mathbf{e}}_y$ is the unit vector directing toward $+y$). It is found that the flat-topped electrons, which have higher temperature in the parallel direction, widely appear along the field line.

4.3.2 Instability Responsible for the Electron Heating

In the previous subsection, we have found that the electron heating parallel to the ambient magnetic field occurs in the plasma sheet-lobe boundary region due to the electron trapping by the electrostatic potential wells associated with the waves, so that the flat-topped electron distribution is formed. In this subsection, we investigate how the unstable waves are excited in the boundary region.

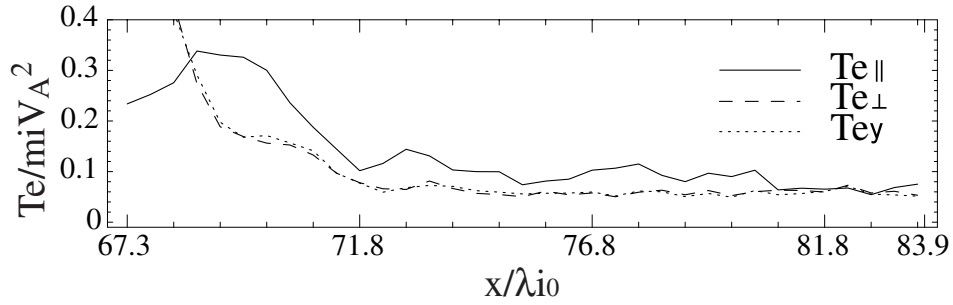


Figure 4.5: Electron temperature profiles along the field line passing through $(x/\lambda_{i0}, z/\lambda_{i0}) = (84.0, -1.32)$ at $t\omega_{ci} = 17.2$. Solid, dashed, and dotted lines denote $T_{e\parallel}$, $T_{e\perp}$, and T_{ey} , respectively.

Figure 4.6 shows the time evolution of E_x profile along the x axis at $z/\lambda_{i0} = -1.32$, where the waves are quite active (see Figure 4.2). It is found that the waves are propagating away from the diffusion region almost along the magnetic field line. The phase velocity is $V_{ph} \sim 4V_A$ in the early stage and increases as they propagate downstream. These waves hardly propagate across the magnetic field line (i.e., in the z direction in the boundary region) and the perpendicular component is quite small, indicating that they are highly electrostatic.

The wave spectrum of E_x in the ω - k space is shown in Figure 4.7(contours). The sampling region is $68.0 \leq x/\lambda_{i0} \leq 75.6$ at $z/\lambda_{i0} = -1.32$ and the time interval is $14.2 \leq t\omega_{ci} \leq 15.3$, which is the region surrounded by the white dashed line in Figure 6 where the number of the trapped electrons are so small that the linear theory is expected to be available. It is found that the spectrum has a clear peak around $k\lambda_{e0} \simeq 0.48$ and $\omega \simeq 0.11\omega_{pe0}$, where ω_{pe0} is the electron plasma frequency defined by n_{ps} , and $\lambda_{e0} = c/\omega_{pe0}$ is the electron inertial length. Figure 4.3 and Figure 4.4 indicate that the strong electron beam along the magnetic field line seems to be responsible for the unstable waves, providing the free energy. In this case, two kinds of instability are prospective. One is the electron two-stream instability between the strong beam electrons and the almost stationary electrons, and the other is the Buneman instability excited due to the velocity difference between the strong beam electrons and the stationary ions.

The unstable waves excited by the electron two-stream instability have the following dispersion relation at the linear stage,

$$1 - \frac{\omega_{pe,s}^2}{(\omega - kV_s)^2} - \frac{\omega_{pe,f}^2}{(\omega - kV_f)^2} = 0, \quad (4.11)$$

where $\omega = \omega_r + i\gamma$, subscripts s and f denote the slow (or stationary) and fast beam electrons, respectively, and V_j ($j = s, f$) is the beam velocity of component j . In Figure

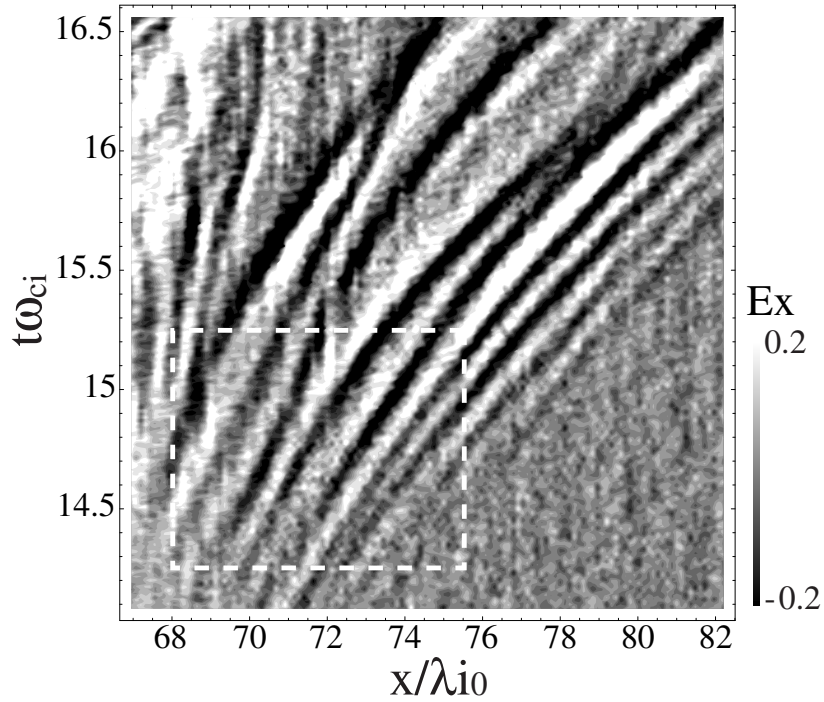


Figure 4.6: Time evolution of E_x profile along the x axis at $z/\lambda_{i0} = -1.32$.

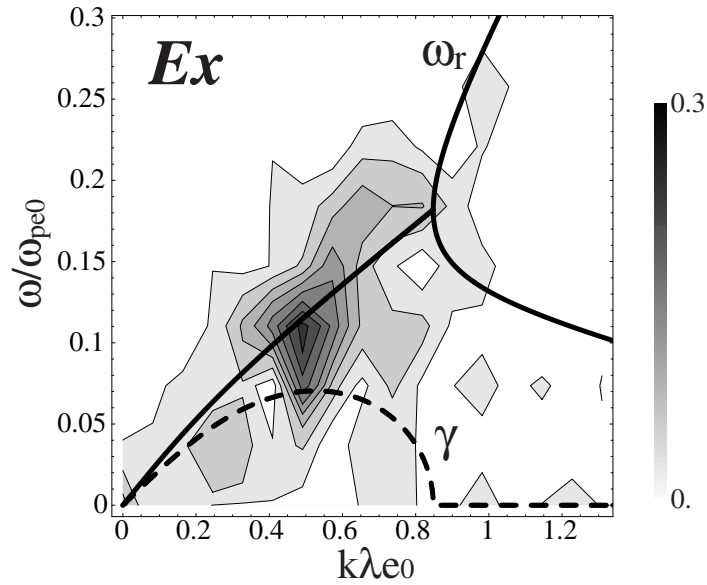


Figure 4.7: Wave spectrum of E_x (contours). The sampling region is $68.0 \leq x/\lambda_{i0} \leq 75.6$ at $z/\lambda_{i0} = -1.32$, and the time interval is $14.2 \leq t\omega_{ci} \leq 15.3$, which is the region surrounded by the white dashed line in Figure 4.6. Bold solid and dashed lines are the theoretical profiles of the wave frequency (ω_r) and growth rate (γ), respectively, deduced from the linear analysis of the electron two-stream instability.

4.7, the wave frequency ω_r and growth rate γ satisfying the dispersion equation (4.11) are superposed by the bold solid and dashed lines, respectively, for the case of $V_s = -1.0 V_A$, $V_f = 7.0 V_A$, $n_{e,s} = 0.031 n_{ps}$, and $n_{e,f} = 0.013 n_{ps}$, where $n_{e,j}$ ($j = s, f$) is the number density of the electrons involved in component j . These theoretical profiles well agree with the simulation results, that is, the wave spectrum obtained from our simulations has an intense peak being consistent with a theoretical dispersion relation (bold solid line), where the growth rate from the theory (bold dashed line) reaches a maximum value. There remains a slight ambiguity in the values of the adopted parameters (i.e., V_s , V_f , $n_{e,s}$, and $n_{e,f}$), but the theoretical profiles are essentially unchanged even if the parameters are slightly shifted.

On the other hand, the linear dispersion relation of the Buneman instability is represented as,

$$1 - \frac{\omega_{pi}^2}{\omega^2} - \frac{\omega_{pe,f}^2}{(\omega - kV_f)^2} = 0, \quad (4.12)$$

where ω_{pi} is the ion plasma frequency, and we assume that the ion beam velocity is negligible compared with the electron beam velocity. The unstable waves excited by the Buneman instability are expected to have $\omega_r \sim (\omega_{pi}^2 \omega_{pe,f})^{1/3} = 0.037 \omega_{pe0}$, and $k \sim \omega_{pe,f}/V_f = 0.27 \lambda_{e0}^{-1}$, using $n_i = 0.044 n_{ps}$, $n_{e,f} = 0.013 n_{ps}$, and $V_f = 7.0 V_A$, where n_i is the number density of ions (Buneman, 1958). Therefore the dispersion relation of the Buneman instability is inconsistent with the spectral peak obtained from our simulations. Furthermore, the growth rate is estimated as $\gamma \sim \omega_r \sim 0.037 \omega_{pe0}$, which is smaller than that of the electron two-stream instability. Thus we can conclude that the instability responsible for the electron heating should be the electron two-stream instability, and not the Buneman instability. A weak peak that appears at the lower left of the intense peak probably represents the Buneman instability.

4.3.3 Origin of the Electron Beam

In this subsection, we study how the strong electron beam with high perpendicular temperature as shown in Figure 4.4b is produced. In order to investigate the origin of the electron beam, we pick out the electrons forming the beam component with $v_{e\parallel} > 4.0$ at $t\omega_{ci} = 15.6$ and trace their trajectories backward in time. Figure 4.8 shows the positions of such electrons at $t\omega_{ci} = 15.6$ (filled circles) and 14.0 (blue triangles and red squares), and the magnetic field lines at $t\omega_{ci} = 14.0$ (solid lines). Note that we classify the electrons chosen at $t\omega_{ci} = 15.6$ into two categories, that is, the electrons with low perpendicular energies ($\sqrt{v_{e\perp}^2 + v_{ey}^2} < v_{th,e0}$) and those with high perpendicular

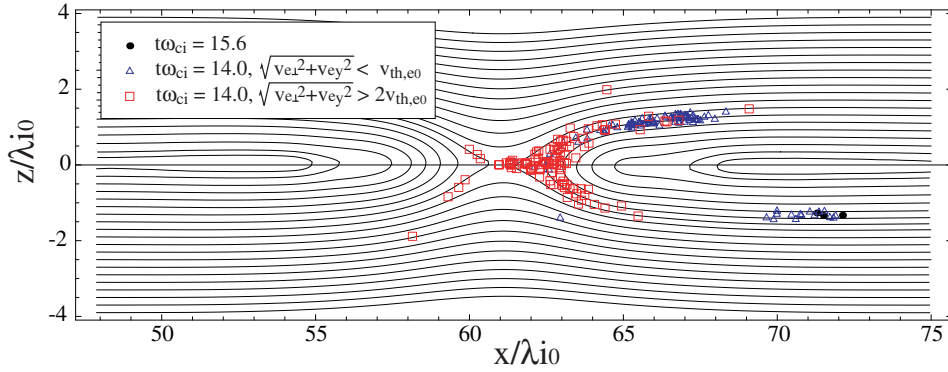


Figure 4.8: Positions of electrons at $t\omega_{ci} = 14.0$ (triangles and squares) traced backward in time from the positions denoted by the filled circles at $t\omega_{ci} = 15.6$. Here, we choose the electrons forming the beam component with $v_{e\parallel}/V_A > 4.0$ at $t\omega_{ci} = 15.6$ as shown in Figure 4.4b. Of these electrons, triangles and squares represent those having low perpendicular energy ($\sqrt{v_{e\perp}^2 + v_{ey}^2} < v_{th,e}$) and high perpendicular energy ($\sqrt{v_{e\perp}^2 + v_{ey}^2} > 2v_{th,e}$) at $t\omega_{ci} = 15.6$, respectively. Magnetic field lines at $t\omega_{ci} = 14.0$ are superposed.

energies ($\sqrt{v_{e\perp}^2 + v_{ey}^2} < 2v_{th,e0}$), where $v_{th,e0} = \sqrt{2T_{e,ps}/m_e}$ is the initial electron thermal velocity and $v_{th,e0} = 3.33 V_A$ in the present case. The positions of the former electrons at $t\omega_{ci} = 14.0$ are indicated by the blue triangles and those of the latter electrons are by the red squares in Figure 4.8.

We find that the origin of the electrons with the low perpendicular energy is clearly different from that with the high perpendicular energy. Most electrons having the high perpendicular energy at $t\omega_{ci} = 15.6$ have passed through the region quite near the X-line. Thus we think that those electrons are originating from the lobe region and accelerated by the inductive electric field E_y in the electron diffusion region and experience the meandering/Speiser motion (Speiser, 1965). Some of them reflect at the magnetic mirror points depending on their pitch angles after they are ejected from the plasma sheet, and start the bouncing motion around the central plasma sheet. Such electrons can gain more kinetic energy by performing the ∇B drift and the curvature drift in the opposite direction of E_y (Hoshino et al., 2001b) and/or by experiencing the betatron acceleration resulting from the increase of the magnetic field strength in the pileup region of the field lines (Birn et al., 2000). Both of these processes can contribute to the increase of the perpendicular energy of electrons. On the other hand, most electrons forming the cold beam component with the low perpendicular energy at $t\omega_{ci} = 15.6$ are located in the opposite side of the plasma sheet at $t\omega_{ci} = 14.0$. They are accelerated by E_{\parallel} (see Figure 4.1b) toward the plasma sheet along the magnetic field line and quickly pass through the

downstream region in the vicinity of the X-line where strong E_y is imposed. Thus these electrons arrive at the opposite side of the plasma sheet without experiencing significant acceleration in the perpendicular direction.

4.3.4 *Electrostatic Solitary Waves Evolved from the Beam Instability*

It is known that the nonlinear evolution of the electron two-stream instabilities can result in the generation of the ESW (e.g., Matsumoto et al., 1994; Kojima et al., 1994; Omura et al., 1996), which have been observed in the dayside magnetopause (Matsumoto et al., 2003) and the near-Earth magnetotail (Cattell et al., 2005) in association with magnetic reconnection. In this subsection, we check whether the electron two-stream instability excited in the plasma sheet-lobe boundary region evolves into the ESW. Figure 4.9a shows the scatter plot in the $(-v_{e\parallel}) - x$ phase space along the x axis at $z/\lambda_{i0} = 1.44$ and $t\omega_{ci} = 17.2$. It is found that the electron holes are clearly formed at $x/\lambda_{i0} \simeq 74.6$ and 77.2 associated with the bipolar structures of E_{\parallel} presented in Figure 4.9b. These bipolar E_{\parallel} structures result from the electrostatic potential, because the depressions in the electron density relative to the ion density appear in Figure 4.9c, in which the ion and electron densities are plotted by the dashed and solid lines, respectively. Thus we can understand that the electron holes in the phase space represent the electron trapping in the electrostatic potential wells.

In Figure 4.10, we show the time evolution of E_x profile along the x axis at the same position in z as Figure 4.9. The bipolar structures seen in Figure 4.9b are found to be a part of the waves excited by the electron two-stream instability in the early stage before $t\omega_{ci} \approx 15.6$. After $t\omega_{ci} \approx 15.6$, the bipolar structures are separated from the unstable waves and start to propagate independently. We consider that the difference in the phase velocity attributes to the difference in the density of the electron beam component. This idea comes from the fact that the phase velocity of the waves excited by the electron two-stream instability increases as the density of the beam component decreases so that the plasma frequency in the rest frame of the electron beam is dropped. The density drop in the beam component is caused by the decrease of the high energy particles, which are trapped by the electrostatic potential wells and excluded from the beam component. However, the density in the source region of the electron beam continues to increase as the reconnected field line moves from the X-line toward the pileup region of the field lines. Therefore the wave packets locating near the source region (i.e., near the plasma sheet along the field line) are dragged away from the main part of the unstable waves as the density of the beam component increases.

The important point in Figure 4.10 is that the bipolar structures are stable for much

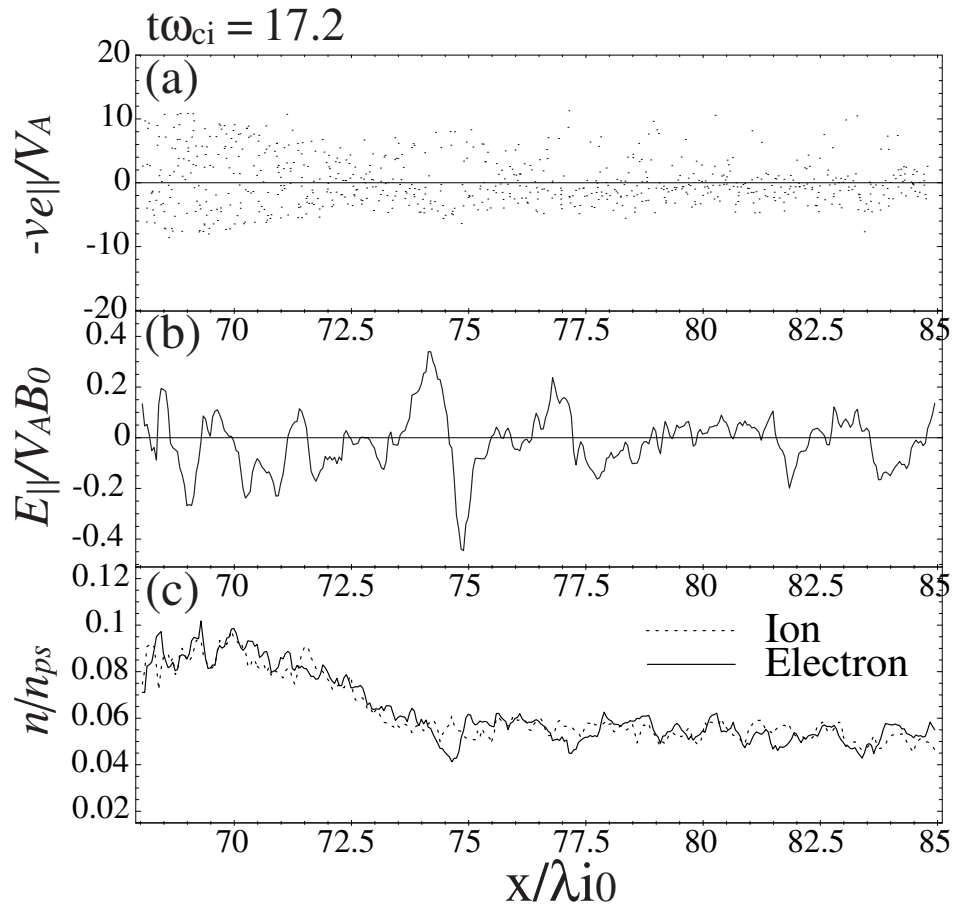


Figure 4.9: (a) Parallel electron velocity ($v_{e\parallel}$), (b) parallel electric field (E_{\parallel}), and (c) ion and electron densities (dotted and solid lines, respectively) along the x axis at $z/\lambda_{i0} = 1.44$ and $t\omega_{ci} = 17.2$.

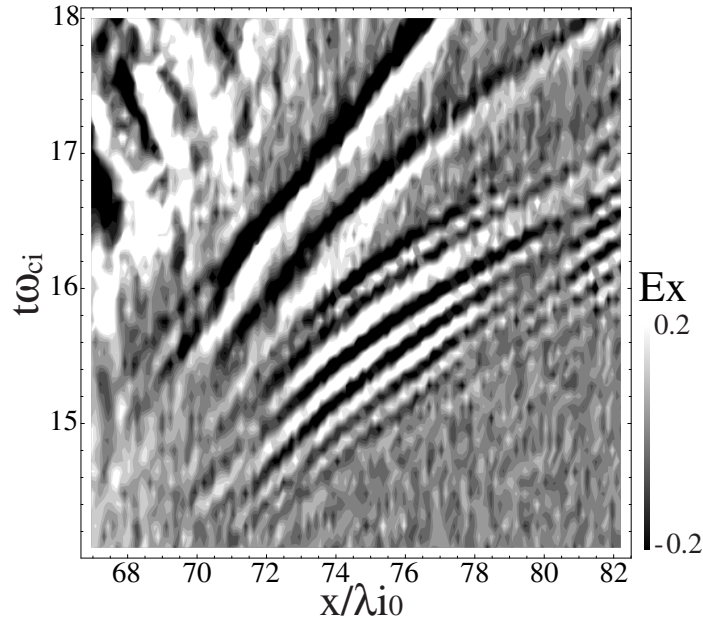


Figure 4.10: Time evolution of E_x profile along the x axis at $z/\lambda_{i0} = -1.44$.

longer time compared with the electron bouncing time ($\sim 0.1 \omega_{ci}^{-1}$). Thus we identify these bipolar structures with the ESW. The left packet of the ESW located at $x/\lambda_{i0} \simeq 74.6$ in Figure 4.9b, which seems to be more stable than the right one, is propagating downstream with the velocity $V_{ESW} \simeq 3V_A$ and the wave length $\lambda_{ESW} \simeq 1.5 \lambda_{i0}$, which are comparable with the wave properties excited from the electron two-stream instability.

The ESW have arisen in association with magnetic reconnection also in earlier simulations using a three-dimensional particle-in-cell code (Drake et al., 2003). However, the generation mechanism of the ESW in their simulations is different from those in our simulations, in that their ESW are evolved from the Buneman instability. The ESW in our simulations are also different from the satellite observations reported by Cattell et al. (2005) for the same reason. Nevertheless, the generation mechanism in our study can be one of the strong candidates to explain the ESW associated with magnetic reconnection, because a large number of observations in the plasma sheet-lobe boundary region have detected the ESW resulting from the electron two-stream instabilities (e.g., Matsumoto et al., 1994; Kojima et al., 1994), which, we showed, are responsible for the formation of the flat-topped electrons as often observed during magnetic reconnection (e.g., Saito et al., 1995; Shinohara et al., 1998). We think that the Buneman instability dominantly evolves in the regions where electrons are entirely flowing relatively to ions so that the number of the stationary electrons are negligibly small, such as in the electron diffusion region. Though it is impossible to study such current-aligned instabilities in our two-

dimensional simulations, it is important to investigate the role of the instabilities in a large three-dimensional system without the guide field.

4.4 Summary and Discussion

We have demonstrated the electron heating mechanism expected in the plasma sheet-lobe boundary region specifically of the Earth magnetotail. We used the newly developed 2-1/2 dimensional PIC code with the AMR and particle splitting techniques, which enables us to perform large-scale kinetic simulations including the extensive downstream region of the X-line. Our main finding is that the electron two-stream instability between the background cold electrons and the strong beam electrons with high perpendicular temperature should be responsible for the formation of the flat-topped electrons, which have been often observed in the plasma sheet-lobe boundary region in association with magnetic reconnection. Both the bump-on-tail instability and the Buneman instability do not play a significant role in the electron heating process in the boundary region.

The heating mechanism of electrons is simple. Electrons are trapped by the electrostatic potential wells resulting from the electron two-stream instability and scattered along the ambient magnetic field, so that the truncated (i.e., flat-topped) distribution function is formed in the parallel direction. The amplitude of the electrostatic turbulence is large enough to produce the flat-topped electrons having a high shoulder energy up to a few keV. The heating process is quickly completed in comparison with the time scale of the dynamic change of the current sheet, so that, once magnetic reconnection is triggered, the flat-topped electrons should be observed in the extensive region of the boundary region. The strong beam electrons consist of two components originating from distinct regions. Some electrons come from the opposite boundary region of the plasma sheet along the magnetic field line, forming the cold component of the electron beam. The others are originating from the lobe region, passing through the electron diffusion region. These electrons are strongly accelerated in the perpendicular direction near the X-line, forming the hot component of the electron beam. We have also revealed that the ESW, which have been often observed in the plasma sheet-lobe boundary region, are evolved from the electron two-stream instability in association with magnetic reconnection. Thus we conclude that the electron two-stream instability presented in the current study should be responsible not only for the formation of the flat-topped electron distribution, but also for the generation of the ESW in the plasma sheet-lobe boundary region when magnetic reconnection has occurred.

Another important candidate responsible for the formation of the flat-topped elec-

trons is the LHDI driven by the cross-field current flowing in the boundary region (Huba et al., 1978; Shinohara et al., 1998). The unstable waves excited by the LHDI propagate obliquely to the ambient magnetic field, so that electrons can be scattered along the magnetic field by the waves. Though it is impossible to study the effects of the LHDI by using our two-dimensional simulations because they omit wave modes propagating in the direction of the sheet current (i.e., the y direction), it is possible alternatively to speculate on the instability by resorting to the linear theory. As shown in Figure 4.7, the growth rate of the electron two-stream instability is estimated as $\gamma_{ETS} \sim 0.1 \omega_{pe}$, where ω_{pe} is the local plasma frequency of electrons. On the other hand, the growth rate of the LHDI can be approximated by $\gamma_{LHD} \sim 0.1 \omega_{LH}$, where $\omega_{LH} = \sqrt{\omega_{ci}\omega_{ce}}$ (ω_{ci} and ω_{ce} are the local cyclotron frequencies of ions and electrons, respectively, here) is the local lower hybrid frequency (Davidson et al., 1977). If the relation $\omega_{pe} \approx \omega_{ce}$ is assumed, $\gamma_{LHD} \sim \sqrt{m_e/m_i} \gamma_{ETS}$ is derived. Therefore the growth rate of the LHDI is much smaller than that of the electron two-stream instability, which indicates that the LHDI could not affect the formation of the flat-topped electrons so much as the electron two-stream instability.

Slow-mode shocks can be also a candidate for the electron scattering in the parallel direction (Schwartz et al., 1987). However, we could not obtain a clear structure of the slow-mode shocks in the present simulation within an allowed simulation time. We think that more large-scale simulations lasting for longer time are necessary for the generation of the slow-mode shocks (Arzner and Scholer, 2001). This indicates that it takes much longer time for the slow-mode shocks to affect the electron heating compared with the electron two-stream instability. Thus we suggest that the heating in the slow-mode shocks would not be effective for the formation of the flat-topped electron distribution in the vicinity of the X-line.

Finally, we make a comment on the net acceleration due to E_{\parallel} that the electrons ejected from the plasma sheet may experience during passing through the wave active region along the magnetic field line. Such acceleration could be one of the generation mechanisms for high energy electrons in association with magnetic reconnection. In Figure 4.11, we show the kinetic energy $W_{e\parallel}$ that a representative electron can gain from E_{\parallel} while it moves from the center of the plasma sheet ($z/\lambda_{i0} = 0$) along the magnetic field line at $t\omega_{ci} = 15.6$. Here, $W_{e\parallel}$ is defined by,

$$W_{e\parallel}(x(l)) = \int_{s=0}^{s=l} (-e)E_{\parallel}(s) ds, \quad (4.13)$$

where s denotes the field-aligned coordinate starting at the center of the plasma sheet, and l is the distance from the origin along the coordinate. The electron is strongly

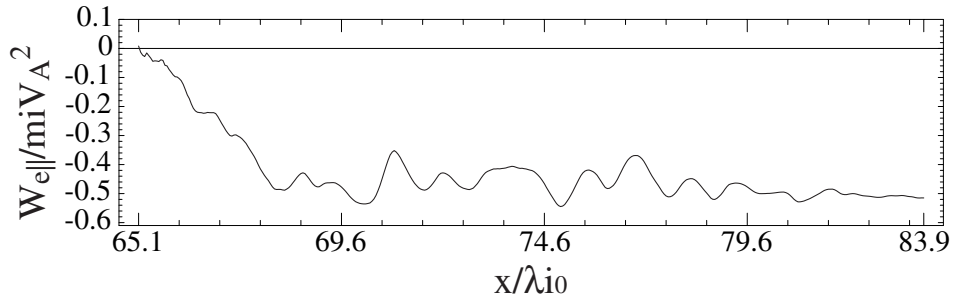


Figure 4.11: Kinetic energy that an electron can gain from the electric field while it moves from the center of the plasma sheet ($z/\lambda_{i0} = 0$) along the magnetic field line passing through $(x/\lambda_{i0}, z/\lambda_{i0}) = (84.0, -1.32)$ at $t\omega_{ci} = 15.6$ as shown in Figure 4.2.

decelerated by E_{\parallel} during the fast ejection from the plasma sheet. In the wave active region, the electron repeats acceleration and deceleration in accordance with the wave structure, but the net energy gain through the region is absent. Therefore the net acceleration due to E_{\parallel} along the wave active region does not seem to occur in our simulations. Nevertheless, this problem should be carefully considered. Recent study by Hoshino (2005) has demonstrated that electrostatic waves having 10 times larger amplitude than that in our simulations can be excited in association with a driven reconnection. Such large waves may contribute to the net energy gain of the outflowing electrons.

CHAPTER 5

Conclusions and Further Studies

So far, a large number of simulation studies using PIC codes have been devoted to understanding a nonlinear evolution of the current sheet associated with magnetic reconnection. However, it has been difficult to describe a large-scale dynamics of magnetic reconnection by the kinetic simulations due to limited computer resources. The main unresolved issues in the reconnection processes include the triggering mechanism, the reconnection rate in the steady-state reconnection, and the energy transport mechanism. The difficulty in approaching such issues lies in the fact that macro-scale structures can be strongly affected by localized micro-scale processes, in which the kinetic treatment of plasma is required.

In order to overcome the difficulty, we first developed a new electromagnetic kinetic code that employs the AMR technique and the particle splitting algorithm to conventional PIC codes. The AMR technique subdivides and removes cells dynamically in accordance with a refinement criterion and enhances the spacial resolution locally. On the other hand, the particle splitting algorithm divides particles locating in fine cells so that it conserves the mass per charge, the total momentum, energy, and distribution of function of particles, and the moments on grids. The particle splitting is needed in order to control the number of particles per cell. Too small number of particles per cell can lead to a significant numerical noise. We performed some test simulations and compared three runs without the AMR, with the AMR, and with both the AMR and the particle splitting. These results indicate not only that the AMR and particle splitting algorithms are successfully applied to the conventional PIC codes, but also that they are quite effective to achieve high-resolution simulations on the evolution of the current sheet associated with magnetic reconnection. Thus the new code allows us to implement a large-scale kinetic simulation on magnetic reconnection.

One of our goals by using large-scale simulations is to investigate a long time evolution of the diffusion region and to see what supports fast reconnection in a steady state. Our

results showed that fast reconnection was quickly achieved in a fully kinetic system but the system did not reach steady state and the reconnection rate went down significantly, even though the effects of the periodic system were almost excluded. We conclude that the key process responsible for slowing magnetic reconnection is the extension of the electron diffusion region associated with the evolution of the strong polarization electric field imposed in the electron inflow region. The polarization electric field directing toward the neutral sheet is caused by the inertia difference between ions and electrons, and enhanced by the meandering motions of the background ions. Because the hot ions initially loaded in the Harris-type current sheet have a large velocity in the out-of-plane direction, they can easily escape from the diffusion region due to the Lorentz force before their meandering motions become dominant. Thus their impact on the strong electrostatic field is small. The polarization electric field forces the inflow electrons to move toward the out-of-plane direction by the $\mathbf{E} \times \mathbf{B}$ drift and enhances the out-of-plane current density in the electron inflow region. The role of the current is to reduce the curvature of the magnetic field lines so that they are mostly parallel to the x direction near the X-line, in such a way that the current density becomes uniform along the upstream edge of the electron diffusion region. As a result, the electron meandering region so the electron diffusion region extends along the x direction. In order to confirm the role of the polarization electric field, we compare the simulation results with $m_i/m_e = 1$ and 100. It is found that (1) a steady-state reconnection is achieved in the system where the polarization electric field does not arise, (2) a large reconnection rate is obtained even in the system without the Hall effects. It is suggested that other mechanisms that are not included in the present model might play an important role in enhancing the reconnection rate. One of the candidates is the anomalous resistivity arising from nonlinear interactions between waves and particles. Indeed the Buneman-type instability is expected to arise in the y direction, because there exists a large velocity difference between ions and electrons beyond the electron thermal velocity in the electron diffusion region. In order to investigate the role of the Buneman-type instability, it is necessary to perform a large-scale kinetic simulation in the three-dimensional system.

Another goal is to reveal energy transport processes associated with magnetic reconnection, that is, where and how plasma is accelerated and heated. In the present study, we paid attention to an electron heating mechanism in the plasma sheet-lobe boundary region, where the truncated (i.e., flat-topped) distribution function of electrons was often observed in the Earth magnetotail during magnetic reconnection. We found that the electron two-stream instability between the background cold electrons and the strong beam electrons with high perpendicular temperature should be responsible for the for-

mation of the flat-topped electrons. Electrons are trapped by the electrostatic potential wells resulting from the electron two-stream instability and scattered along the ambient magnetic field, so that the truncated distribution function is formed in the parallel direction. We showed that the electron heating through this process occurred in the extensive region of the boundary region and the heating level was consistent with satellite observations. The strong beam electrons consist of two components originating from distinct regions. Some electrons come from the opposite boundary region of the plasma sheet along the magnetic field line, forming the cold component of the electron beam. The others are originating from the lobe region, passing through the electron diffusion region. Furthermore, we revealed that the ESW could be evolved from the electron two-stream instability in association with magnetic reconnection. Thus such waves should be observed in the boundary region during reconnection.

The important issue which we could not access through this study is the triggering mechanism of magnetic reconnection. In the present study, magnetic reconnection is initialized with a small perturbation in the magnetic field, so that the resulting thinner current sheet enhances the growth rate of the tearing instability (Furth et al., 1963; Drake and Lee, 1977). However, since the current sheet width typically reaches a few Re in the Earth magnetotail (e.g., Sergeev et al, 1993), it is difficult for the tearing mode alone to trigger fast reconnection within a sufficiently short time scale. Recent two-dimensional simulations in the plane orthogonal to the initial magnetic field (in which the tearing instability does not arise) have revealed that the LHDI is excited at the edge of the current sheet and it modifies the initial structure, so that a Kelvin-Helmholtz instability (KHI) develops at much faster rate than predicted by linear theories based on the initial equilibrium (Shinohara et al., 2001; Lapenta and Brackbill, 2002). Furthermore, recent three-dimensional simulations have suggested that the modification of the initial profile caused by the LHDI can allow the onset of magnetic reconnection and enhance the growth of the tearing instability (Lapenta et al., 2003; Scholer et al., 2003; Ricci et al., 2004). However, the system sizes employed in their simulations are not large enough for the KHI (which has a MHD scale) to arise because of limited computer resources. Thus it is an open question how the KHI affects the tearing instability. Three-dimensional version of our code would enable us to perform 10 – 50 times larger-scale simulations than the previous simulations. It is a promising tool to study the relationship between the tearing instability, the LHDI, and the KHI, and a key to open a new era.

This thesis was written on the basis of the following papers.

1. Fujimoto, K., and S. Machida (2005), Full particle simulation of the plasma sheet using adaptive mesh refinement (AMR) technique, *Adv. Space Res.*, in press, doi:10.1016/j.asr.2005.03.096.
2. Fujimoto, K., and S. Machida (2005), Electromagnetic full particle code with adaptive mesh refinement technique: Application to the current sheet evolution, *J. Comput. Phys.*, in press, doi:10.1016/j.jcp.2005.10.003.
3. Fujimoto, K., and S. Machida (2005), A generation mechanism of electrostatic waves and subsequent electron heating in the plasma sheet-lobe boundary region during magnetic reconnection, *J. Geophys. Res.*, submitted.

Acknowledgments

The author would like to express grateful appreciation to Prof. S. Machida for useful discussions and financial support. The author also wishes to thank all colleagues of Department of Geophysics, Kyoto University for their valuable instruction and technical support, and would like to express thanks to the staffs of the Academic Center for Computing and Media Studies of Kyoto University for their technical advices to improve the performance of the simulation code. Some calculations were performed by FUJITSU HPC2500 installed at the Academic Center for Computing and Media Studies of Kyoto University, the Information Technology Center of Nagoya University, and the Research Institute for Sustainable Humanosphere (RISH) of Kyoto University. Finally, the author acknowledges the Research Fellowships of the Japan Society for the Promotion of Science (JSPS) for Young Scientists. This work has been partly supported by the Grant-in-Aid for JSPS Fellows.

References

- Alfvén H. (1957), On the theory of comet tails, *Tellus*, *9*, 92–96.
- Arzner, K., and M. Scholer (2001), Kinetic structure of the post plasmoid plasma sheet during magnetotail reconnection, *J. Geophys. Res.*, *106*, 3827–3844.
- Asano, Y., T. Mukai, M. Hoshino, Y. Saito, H. Hayakawa, and T. Nagai (2004), Current sheet structure around the near-Earth neutral line observed by Geotail, *J. Geophys. Res.*, *109*, A02212, doi:10.1029/2003JA010114.
- Axford, W. I., H. E. Petschek, and G. L. Siscoe (1965), Tail of the magnetosphere, *J. Geophys. Res.*, *70*, 1231–1236.
- Baker, D. N., and E. C. Stone (1976), Energetic electron anisotropies in the magnetotail: Identification of open and closed field lines, *Geophys. Res. Lett.*, *3*, 557–560.
- Baker, D. N., T. I. Pulkkinen, J. Büchner, and A. J. Klimas (1999), Substorms: A global instability of the magnetosphere-ionosphere system, *J. Geophys. Res.*, *104*, 14,601–14,611.
- Barnes, J., and P. Hut (1986), A hierarchical $O(N \log N)$ force-calculation algorithm, *Nature*, *324*, 446–449.
- Baumjohann, W., G. Paschmann, and C. A. Cattell (1989), Average plasma properties in the central plasma sheet, *J. Geophys. Res.*, *94*, 6597–6606.
- Baumjohann, W., and R. A. Treumann (1997), *Basic Space Plasma Physics*, Imperial College Press, London.
- Berger, M. J., and J. Olinger, Adaptive mesh refinement for hyperbolic partial differential equations, *J. Comput. Phys.*, *53*, 484–512.
- Berger, M. J., and P. Colella (1989), Local adaptive mesh refinement for shock hydrodynamics, *J. Comput. Phys.*, *82*, 64–84.

- Birdsall, C. K. and A. B. Langdon (1991), *Plasma physics via computer simulation*, Institute of Physics Publishing, London.
- Birn, J., M. F. Thomsen, J. E. Borovsky, G. D. Reeves, and M. Hesse (2000), Particle acceleration in the dynamic magnetotail, *Phys. Plasmas*, *7*, 2149–2156.
- Birn, J., J. F. Drake, M. A. Shay, B. N. Rogers, R. E. Denton, M. Hesse, M. Kuznetsova, Z. W. Ma, A. Bhattacharjee, A. Otto, and P. L. Pritchett (2001), Geospace environmental modeling (GEM) magnetic reconnection challenge, *J. Geophys. Res.*, *106*, 3715–3719.
- Biskamp, D., E. Schwarz, and J. F. Drake (1997), Two-fluid theory of collisionless magnetic reconnection, *Phys. Plasmas*, *4*, 1002–1009.
- Buneman, O. (1958), Instability, turbulence, and conductivity in current-carrying plasma, *Phys. Rev. Lett.*, *1*, 8–9.
- Cai, H. J., and L. C. Lee (1997), The generalized Ohm’s law in collisionless magnetic reconnection, *Phys. Plasmas*, *4*, 509–520.
- Cattell, C., J. Dombek, J. Wygant, J. F. Drake, M. Swisdak, M. L. Goldstein, W. Keith, A. Fazakerley, M. André, E. Lucek, and A. Balogh (2005), Cluster observations of electron holes in association with magnetotail reconnection and comparison to simulations, *J. Geophys. Res.*, *110*, A01211, doi:10.1029/2004JA010519.
- Coroniti, F. V., L. A. Frank, D. J. Williams, R. P. Lepping, F. L. Scarf, S. M. Krimigis, and G. Gloeckler (1980), Variability of plasma sheet dynamics, *J. Geophys. Res.*, *85*, 2957–2977.
- Cowley, S. W. H. (1985), Magnetic reconnection, in *Solar System Magnetic Fields*, edited by E. R. Priest, pp. 121-155, Reidel, Dordrecht.
- Chapman, S., and V. C. A. Ferraro (1931), A new theory of magnetic storms, *Terr. Magn. Atmos. Electr.*, *36*, 77–97.
- Daughton, W. (1999), The unstable eigenmodes of a neutral sheet, *Phys. Plasmas*, *6*, 1329–1343.
- Davidson, R. C., N. T. Gladd, C. S. Wu, and J. D. Huba (1977), Effects of finite plasma beta on the lower-hybrid-drift instability, *Phys. Fluids*, *20*, 301–310.

- Drake, J. F., and Y. C. Lee (1977), Kinetic-theory of tearing instabilities, *Phys Fluids*, *20*, 1341–1353.
- Drake, J., M. Swisdak, C. Cattell, M. Shay, B. Rogers, and A. Zeiler (2003), Formation of electron holes and particle energization during magnetic reconnection, *Science*, *299*, 873–877.
- Dreher, J., and R. Grauer (2005), Racocon: A parallel mesh-adaptive framework for hyperbolic conservation laws, *Parallel Computing*, *31*, 913–932, doi:10.1016/j.parco.2005.04.011.
- Dungey, J. W. (1953), Conditions for the occurrence of electrical discharges in astrophysical systems, *Phil. Mag., Ser. 7*, *44*, 725–738.
- Dungey, J. W. (1961), Interplanetary magnetic field and the auroral zones, *Phys. Rev. Lett.*, *6*, 47–48.
- Dungey, J. W. (1978), The history of the magnetopause regions, *J. Atmos. Terr. Phys.*, *40*, 231–234.
- Fujimoto, K., and S. Machida (2003), An electron heating mechanism in the outflow region from the X-type neutral line, *J. Geophys. Res.*, *108*, 1349, doi:10.1029/2002JA009810.
- Fujimoto, K., and S. Machida (2005a), Full particle simulation of the plasma sheet using adaptive mesh refinement (AMR) technique, *Adv. Space Res.*, in press, doi:10.1016/j.asr.2005.03.096.
- Fujimoto, K., and S. Machida (2005b), Electromagnetic full particle code with adaptive mesh refinement technique: Application to the current sheet evolution, *J. Comput. Phys.*, in press, doi:10.1016/j.jcp.2005.10.003.
- Furth, H. P., J. Killeen, and M. N. Rosenbluth (1963), Finite-resistivity instabilities of a sheet pinch, *Phys. Fluids*, *6*, 459–484.
- Gelato, S., D. F. Chernoff, and I. Wasserman (1997), An adaptive hierarchical particle-mesh code with isolated boundary conditions, *Astrophys. J.*, *480*, 115–131.
- Giovanelli, R. G. (1947), Magnetic and electric phenomena in the sun’s atmosphere associated with sunspots, *Mon. Notices Roy. Astron. Soc.*, *107*, 338–355.

- Gold, T. (1961), Present evidence concerning magnetic fields and particle fluxes in the solar system, *Space Res.*, *2*, 828–836.
- Griebel, M., and G. Zumbusch (1999), Parallel multigrid in an adaptive PDE solver based on hashing and space-filling curves, *Parallel Computing*, *25*, 827–843.
- Harris, E. G. (1962), On a plasma sheath separating regions of oppositely directed magnetic field, *Nuovo Cimento*, *23*, 115–121.
- Hesse, M. and D. Winske (1994), Hybrid simulations of collisionless reconnection in current sheets, *J. Geophys. Res.*, *99*, 11,177–11,192.
- Hesse, M. and D. Winske (1998), Electron dissipation in collisionless magnetic reconnection, *J. Geophys. Res.*, *103*, 26,479–26,486.
- Hesse, M., K. Schindler, J. Birn, and M. Kuznetsova (1999), The diffusion region in collisionless magnetic reconnection, *Phys. Plasmas*, *6*, 1781–1795.
- Hesse, M, J. Birn, and M. Kuznetsova (2001), Collisionless magnetic reconnection: Electron processes and transport modeling, *J. Geophys. Res.*, *106*, 3721–3735.
- Hones, E. W., Jr. (1973), Plasma flow in the plasma sheet and its relation to substorms, *Radio Sci.*, *8*, 979–990.
- Hoshino, M., T. Mukai, T. Yamamoto, and S. Kokubun (1998), Ion dynamics in magnetic reconnection: Comparison between numerical simulation and Geotail observations, *J. Geophys. Res.*, *103*, 4509–4530.
- Hoshino, M., K. Hiraide, and T. Mukai (2001a), Strong electron heating and non-Maxwellian behavior in magnetic reconnection, *Earth Planets Space*, *53*, 627–634.
- Hoshino, M., T. Mukai, T. Terasawa, and I. Shinohara (2001b), Suprathermal electron acceleration in magnetic reconnection, *J. Geophys. Res.*, *106*, 25,979–25,997.
- Hoshino, M. (2005), Electron surfing acceleration in magnetic reconnection, *J. Geophys. Res.*, *110*, A10215, doi:10.1029/2005JA011229.
- Huang, J., and L. Greengard (2000), A fast direct solver for elliptic partial differential equations on adaptively refined meshes, *SIAM J. Sci. Comput.*, *21*, 1551–1566.
- Huba, J. D., N. T. Gladd, and K. Papadopoulos (1978), Lower-hybrid-drift wave turbulence in the distant magnetotail, *J. Geophys. Res.*, *83*, 5217–5226.

- Huba, J. D., and L. I. Rudakov (2004), Hall magnetic reconnection rate, *Phys. Rev. Lett.*, *93*, 175003.
- Jessop, C., M. Duncan, and W. Y. Chau (1994), Multigrid methods for N-body gravitational systems, *J. Comput. Phys.*, *115*, 339–351.
- Karimabadi, H., D. Krauss-Varban, J. D. Huba, and H. X. Vu (2004), On magnetic reconnection regimes and associated three-dimensional asymmetries: Hybrid, Hall-less hybrid, and Hall-MHD simulations, *J. Geophys. Res.*, *109*, A09205.
- Khokhlov, A. M. (1998), Fully threaded tree algorithms for adaptive refinement fluid dynamics simulations, *J. Comput. Phys.*, *143*, 519–543.
- Knebe, A., A. Green, and J. Binney (2001), Multi-level adaptive particle mesh (MLAPM): A c code for cosmological simulations, *Mon. Not. R. Astron. Soc.*, *325*, 845–864.
- Kojima, H., H. Matsumoto, T. Miyatake, I. Nagano, A. Fujita, L. A. Frank, T. Mukai, W. R. Paterson, Y. Saito, S. Machida, and R. R. Anderson (1994), Relation between electrostatic solitary waves and hot plasma flow in the plasma sheet boundary layer: GEOTAIL observations, *Geophys. Res. Lett.*, *21*, 2921–2924.
- Kravtsov, A. V., A. A. Klypin, and A. M. Khokhlov (1997), Adaptive refinement tree: A new high-resolution N-body code for cosmological simulations, *Astrophys. J. Suppl. Ser.*, *111*, 73–94.
- Kuznetsova, M. M., M. Hesse, and D. Winske (1998), Kinetic quasi-viscous and bulk flow inertia effects in collisionless magnetotail reconnection, *J. Geophys. Res.*, *103*, 199–213.
- Kuznetsova, M. M., M. Hesse, D. Winske (2001), Collisionless reconnection supported by nongyrotropic pressure effects in hybrid and particle simulations, *J. Geophys. Res.*, *106*, 3799–3810.
- Langdon, A. B., and B. F. Lasinski (1976), Electromagnetic and relativistic plasma simulation models, *Methods Comput. Phys.*, *16*, 327–366.
- Lapenta, G. (2002), Particle rezoning for multidimensional kinetic particle-in-cell simulations, *J. Comput. Phys.*, *181*, 317–337.
- Lapenta, G. and J. U. Brackbill (2002), Nonlinear evolution of the lower hybrid drift instability: Current sheet thinning and kinking, *Phys. Plasmas*, *9*, 1544–1554.

- Lapenta, G., J. U. Brackbill, and W. S. Daughton (2003), The unexpected role of the lower hybrid drift instability in magnetic reconnection in the three dimensions, *Phys. Plasmas*, *10*, 1577–1587, doi:10.1063/1.1560615.
- Lin, R. P., and H. S. Hudson (1976), Nonthermal processes in large solar-flares, *Sol. Phys.*, *50*, 153–178.
- Lin, R. P., S. Krucker, G. J. Hurford, D. M. Smith, H. S. Hudson, G. D. Holman, R. A. Schwartz, B. R. Dennis, G. H. Share, R. J. Murphy, A. G. Emslie, C. Johns-Krull, and N. Vilmer (2003), RHESSI observations of particle acceleration and energy release in an intense solar gamma-ray line flare, *Astrophys. J.*, *595*, L69–L76.
- Lin, Y. and D. W. Swift (1996), A two-dimensional hybrid simulation of the magnetotail reconnection layer, *J. Geophys. Res.*, *101*, 19,859–19,870.
- Mandt, M. E., R. E. Denton, and J. F. Drake (1994), Transition to whistler mediated magnetic reconnection, *Geophys. Res. Lett.*, *21*, 73–76.
- Matsumoto, H., H. Kojima, T. Miyatake, Y. Omura, M. Okada, I. Nagano, and M. Tsutsui (1994), Electrostatic Solitary Waves (ESW) in the magnetotail: BEN wave forms observed by GEOTAIL, *Geophys. Res. Lett.*, *21*, 2915–2918.
- Matsumoto, H., X. H. Deng, H. Kojima, and R. R. Anderson (2003), Observation of electrostatic solitary waves associated with reconnection on the dayside magnetopause boundary, *Geophys. Res. Lett.*, *30*, 1326, doi:10.1029/2002GL016319.
- McPherron, R. L. (1970), Growth phase of magnetospheric substorms, *J. Geophys. Res.*, *75*, 5592–5599.
- Miyashita, Y., S. Machida, A. Nishida, T. Mukai, Y. Saito, and S. Kokubun (1999), GEOTAIL observations of total pressure and electric field variations in the near and mid-distant tail associated with substorm onsets, *Geophys. Res. Lett.*, *26*, 639–642.
- Nagai, T., M. Fujimoto, Y. Sato, S. Machida, T. Terasawa, R. Nakamura, T. Yamamoto, T. Mukai, A. Nishida, and S. Kokubun (1998), Structure and dynamics of magnetic reconnection for substorm onsets with Geotail observations, *J. Geophys. Res.*, *103*, 4419–4440.
- Nagai, T., I. Shinohara, M. Fujimoto, M. Hoshino, Y. Saito, S. Machida, and T. Mukai (2001), Geotail observations of the Hall current system: Evidence of magnetic reconnection in the magnetotail, *J. Geophys. Res.*, *106*, 25,929–25,949.

- Nakabayashi, J. and S. Machida (1997), Electromagnetic hybrid-code simulation of magnetic reconnection: Velocity distribution functions of accelerated ions, *Geophys. Res. Lett.*, *24*, 1339–1342.
- Nakamura, M. S., M. Fujimoto, and K. Maezawa (1998), Ion dynamics and resultant velocity space distribution functions in the course of magnetic reconnection, *J. Geophys. Res.*, *103*, 4531–4546.
- Omura, Y., H. Matsumoto, T. Miyake, and H. Kojima (1996), Electron beam instabilities as generation mechanism of electrostatic solitary waves in the magnetotail, *J. Geophys. Res.*, *101*, 2685–2697.
- Parker, E. N. (1958), Dynamics of the interplanetary gas and magnetic fields, *Astrophys. J.*, *128*, 664–676.
- Parker, E. N. (1963), The solar-flare phenomenon and the theory of reconnection and annihilation of magnetic fields, *Astrophys. J., Suppl. Ser.*, *8*, 177–212.
- Petschek, H. E. (1964), Magnetic field annihilation, in *AAS-NASA Symposium on the Physics of Solar Flares*, *NASA Spec. Publ. SP-50*, 425–439.
- Petschek, H. E. (1966), The mechanism for reconnection of geomagnetic and interplanetary field lines, in *The Solar Wind*, edited by R. J. Mackin, and M. Neugebauer, pp. 257–273, Pergamon, Oxford.
- Pei, W., R. Horiuchi, and T. Sato (2001), Ion dynamics in steady collisionless driven reconnection, *Phys. Rev. Lett.*, *87*, 235003.
- Press, W. H., S. A. Teukolsky, W. T. Vetterling, and B. P. Flannery (1992), *Numerical Recipes in FORTRAN*, 2nd ed., Cambridge Univ. Press, New York.
- Pritchett, P. L. (1994), Effects of electron dynamics on collisionless reconnection in two-dimensional magnetotail equilibria, *J. Geophys. Res.*, *99*, 5935–5941.
- Pritchett, P. L. (2001), Geospace Environment Modeling magnetic reconnection challenge: Simulations with a full particle electromagnetic code, *J. Geophys. Res.*, *106*, 3783–3798.
- Ricci, P., J. U. Brackbill, W. Daughton, and G. Lapenta (2004), Influence of the lower hybrid drift instability on the onset of magnetic reconnection, *Phys. Plasmas*, *11*, 4489–4500, doi:10.1063/1.1778744.

- Rostoker, G. (1972), Polar magnetic substorms, *Rev. Geophys. Space Phys.*, *10*, 157–211.
- Saito, Y., T. Mukai, T. Terasawa, A. Nishida, S. Machida, M. Hirahara, K. Maezawa, S. Kokubun, and T. Yamamoto (1995), Slow-mode shocks in the magnetotail, *J. Geophys. Res.*, *100*, 23,567 – 23,581.
- Sato, T. (1979), Strong plasma acceleration by slow shocks resulting from magnetic reconnection, *J. Geophys. Res.*, *84*, 7177–7190.
- Sato, T., and T. Hayashi (1979), Externally driven magnetic reconnection and a powerful magnetic energy converter, *Phys. Fluids*, *22*, 1189–1202.
- Sergeev, V. A., D. G. Mitchell, C. T. Russell, and D. J. Williams (1993), Structure of the tail plasma/current sheet at $\sim 11 R_E$ and its changes in the course of a substorm, *J. Geophys. Res.*, *98*, 17,345–17,365.
- Scholer, M., and D. Roth (1987), A simulation study on reconnection and small-scale plasmoid formation, *J. Geophys. Res.*, *92*, 3223–3233.
- Scholer, M., I. Sidorenko, C. H. Jaroschek, R. A. Treumann, and A. Zeiler (2003), Onset of collisionless magnetic reconnection in thin current sheets: Tree-dimensional particle simulations, *Phys. Plasmas*, *10*, 3521–3527, doi:10.1063/1.1597494.
- Schwartz, S. J., M. F. Thomsen, W. C. Feldman, and F. T. Douglas (1987), Electron dynamics and potential jump across slow mode shocks, *J. Geophys. Res.*, *92*, 3165–3174.
- Shay, M. A., and J. F. Drake (1998), The role of electron dissipation on the rate of collisionless magnetic reconnection, *Geophys. Res. Lett.*, *25*, 3759–3762.
- Shay, M. A., J. F. Drake, R. E. Denton, and D. Biskamp (1998), Structure of the dissipation region during collisionless magnetic reconnection, *J. Geophys. Res.*, *103*, 9165–9176.
- Shay, M. A., J. F. Drake, B. N. Rogers, and R. E. Denton (1999), The scaling of collisionless, magnetic reconnection for large systems, *Geophys. Res. Lett.*, *26*, 2163–2166.
- Shay, M. A., J. F. Drake, and B. N. Rogers (2001), Alfvénic collisionless magnetic reconnection and the Hall term, *J. Geophys. Res.*, *106*, 3759–3772.
- Shay, M. A., J. F. Drake, M. Swisdak, and B. N. Rogers (2004), The scaling of embedded collisionless reconnection, *Phys. Plasmas*, *11*, 2199–2213.

- Shinohara, I., T. Nagai, M. Fujimoto, T. Terasawa, T. Mukai, K. Tsuruda, and T. Yamamoto (1998), Low-frequency electromagnetic turbulence observed near the sub-storm onset site, *J. Geophys. Res.*, *103*, 20,365–20,388.
- Shinohara, I., H. Suzuki, M. Fujimoto, and M. Hoshino (2001), Rapid large-scale magnetic-field dissipation in a collisionless current sheet via coupling between Kelvin-Helmholtz and lower-hybrid drift instabilities, *Phys. Rev. Lett.*, *87*, 095001.
- Sonnerup, B. U. Ö. (1979), Magnetic field reconnection, in *Solar System Plasma Physics*, vol. III, edited by L. J. Lanzerotti, C. F. Kennel, and E. N. Parker, pp. 45–108, North-Holland, Amsterdam.
- Speiser, T. W. (1965), Particle trajectories in model current sheets 1: Analytical solutions, *J. Geophys. Res.*, *70*, 4219–4226.
- Spitzer, L., Jr. (1962), *Physics of Fully Ionized Gases*, 2nd ed., p. 139, Interscience, New York.
- Suisalu, I., and E. Saar (1995), An adaptive multigrid solver for high-resolution cosmological simulations, *Mon. Not. R. Astron. Soc.*, *274*, 287–299.
- Sweet, P. A. (1958), The neutral point theory of solar flares, in *Electromagnetic Phenomena in Cosmical Physics*, edited by B. Lehnert, pp. 123–134, Cambridge University Press, London.
- Sweet, P. A. (1961), Mechanisms of solar flares, *Ann. Rev. Astron. Astrophys.*, *7*, 149–176.
- Swisdak, M., J. F. Drake, M. A. Shay, and J. G. McIlhargey (2005), Transition from antiparallel to component magnetic reconnection, *J. Geophys. Res.*, *110*, A05210, doi:10.1029/2004JA010748.
- Tanaka, M. (1995), Macro-particle simulations of collisionless magnetic reconnection, *Phys. Plasmas*, *2*, 2920–2930.
- Terasawa, T., and A. Nishida (1976), Simultaneous observations of relativistic electron bursts and neutral-line signatures in the magnetotail, *Planet. Space Sci.*, *24*, 855–866.
- Terasawa, T. (1983), Hall current effect on tearing mode instability, *Geophys. Res. Lett.*, *10*, 475–478.

- Teyssier, R. (2002), Cosmological hydrodynamics with adaptive mesh refinement A new high resolution code called RAMSES, *Astronomy and Astrophysics*, *385*, 337–364.
- Ugai, M. (1993), Computer studies on the fast reconnection mechanism in a sheared field geometry, *Phys Fluids B*, *5*, 3021–3031.
- Vasyliunas, V. M. (1975), Theoretical models of magnetic field line merging, 1, *Rev. Geophys.*, *13*, 303–336.
- Vay, J. L., P. Colella, A. Friedman, D. P. Grote, P. McCorquodale, and D. B. Serafini (2004), Implementations of mesh refinement schemes for particle-in-cell plasma simulations, *Comput. Phys. Comm.*, *164*, 297–305.
- Villasenor, J., and O. Buneman (1992), Rigorous charge conservation for local electromagnetic field solvers, *Comput. Phys. Comm.*, *69*, 306–316.
- Villumsen, J. V. (1989), A new hierarchical particle-mesh code for very large scale cosmological N-body simulations, *Astrophys. J. Suppl. Ser.*, *71*, 407–431.
- Yahagi, H., and Y. Yoshii (2001), N-body code with adaptive mesh refinement, *Astrophys. J.*, *558*, 463–475.